

# Tool eccentricity in thick-plate aluminum alloy friction stir welds

by

Luqman Hakim Ahmad Shah

A thesis

presented to the University of Waterloo

in fulfilment of the

thesis requirement for the degree of

Doctor of Philosophy

in

Mechanical and Mechatronics Engineering

Waterloo, Ontario, Canada, 2020

©Luqman Hakim Ahmad Shah 2020

## **Examining committee membership**

The following served on the Examining Committee for this thesis.

The decision of the Examining Committee is by majority vote.

External Examiner	MOHAMMAD JHAZI Professor
Supervisor 1	ADRIAN GERLICH Associate Professor
Supervisor 2	SCOTT WALBRIDGE Associate Professor
Internal Member	NORMAN ZHOU Professor
Internal Member	HAMIDREZA JAHED MOTLAGH Professor
Internal-external Member	ADIL AL-MAYAH Associate Professor

## **Author's declaration**

This thesis consists of material all of which I authored or co-authored: see Statement of Contributions included in the thesis. This is a true copy of the thesis, including any required final revisions, as accepted by my examiners.

I understand that my thesis may be made electronically available to the public.

## Statement of contributions

Luqman Hakim Ahmad Shah was the sole author for Chapters 1, 3 and 7. This thesis consists in part of four manuscripts written for publication. Exceptions to sole authorship of material and its respective publication details are as follows:

Literature review presented in Chapter 2:

Luqman Shah wrote the article while Walbridge and Gerlich provided valuable discussions on the subject.

‘Tool eccentricity in friction stir welding: a comprehensive review’, **L.H. Shah**, S. Walbridge and A. Gerlich, *Science and Technology of Welding and Joining* 2019, 24 (6), 566-578.

Research presented in Chapter 4:

Luqman Shah wrote the article, conducted the friction stir welding process and most of the mechanical and microstructural characterizations. Midawi conducted digital image correlation experiments and analysis. Walbridge and Gerlich provided funding and expertise on the subject.

‘Influence of tool eccentricity on the material flow and microstructural properties of AA6061 aluminum alloy friction stir welds’, **L.H. Shah**, A.R.H. Midawi, S. Walbridge, A. Gerlich, *Journal of Alloys and Compounds* 2020, 826.

Research presented in Chapter 5:

Luqman Shah wrote the article, conducted the friction stir welding as well as most of mechanical and microstructural characterizations. Sonbolestan conducted temperature measurements and hardness characterization. Midawi conducted digital image correlation experiments and analysis. Walbridge and Gerlich provided funding and expertise on the subject.

‘Dissimilar friction stir welding of thick plate AA5052-AA6061 aluminum alloys: effects of material positioning and tool eccentricity’, **Luqman Hakim Ahmad Shah**, Seyedhossein

Sonbolestan, Abdelbaset R. H. Midawi, Scott Walbridge, Adrian Gerlich, *International Journal of Advance Manufacturing Processes* 2019, 105(1-4), 889-904.

Research presented in Chapter 6:

Luqman Shah wrote the article, conducted the peak temperature and high speed camera (HSC) studies. Fleury conducted the force and torque measurements along with camera studies. St-George, Walbridge and Gerlich provided funding and expertise on the subject.

‘Evolution of process parameters in friction stir welding of AA6061 aluminum alloy by varying tool eccentricity’, **L.H. Shah**, A. Fleury, L. St-George, S. Walbridge, A.P. Gerlich, *International Journal of Advanced Manufacturing Technology* 2020, submitted.

## **Abstract**

Tool eccentricity, i.e. the wobbling motion of a milling tool during rapid rotation caused by its slight offset from the spindle rotational axis, has been given very limited attention in the 20 years of friction stir welding (FSW) research, despite the existence of this phenomenon (to varying severity) in every FSW process. While in most cases this irregularity is inherently impossible to prevent and intuitively undesirable, several works in recent years have revisited this issue and suggested that by amplifying the tool eccentricity, beneficial improvements in the outcome of the weld joint could actually be realized.

However, such claims do not provide a detailed explanation as to why this is the case and fail to explain how it seems to contradict previous findings. Such discrepancies in the literature therefore warrant an in-depth analysis of the matter in order to understand the phenomenon better and finally suggest a definitive verdict as to whether the advantages of tool eccentricity reported in recent works outweigh the disadvantages readily associated with the phenomenon. This is particularly vital since FSW has recently attracted much attention in heavy structural applications of thick-plate aluminum alloys with the introduction of three FSW standards, namely ISO 25239 AWS D12-2014 and CSA W59.2 2018, which are expected to act as catalysts for further expansion of FSW applications. Since such applications would require welding of long beams, extrusions, or plates, any advantages and/or disadvantages of tool eccentricity would be inherently embedded in the system and would therefore require serious consideration.

To come to a sound verdict, this study attempts to view the issue in a holistic manner. Following the ‘structure, property, process, and performance’ tetrahedral components of materials engineering, this study firstly looks into the microstructural and mechanical evolution of welded joints by employing tools with specified eccentricity. The mechanism behind the observed metallurgical and mechanical transformation are then investigated. Next, the changes in the process parameters are analyzed and subsequently discussed. The study then expands these findings through characterization in dissimilar alloy FSW joints. Finally, the impact of tool eccentricity on the welding process response variables is assessed.

From the metallurgical standpoint, the formation of rougher weld bead surface and expansion of periodic bands in the stir zone when eccentric tools were employed suggested improved material flow and mixing. Through observations of grain refinement and higher strain

rates compared to typical aligned specimens, it is also suggested that enhanced shearing activity occurs with increased eccentricity. In addition, a shift in preferred texture orientation through energy backscattered diffraction (EBSD) analysis suggests deviation from the typical material flow order due to increased tool eccentricity. Further transmission electron microscopy (TEM) observations suggest that evolution of second phase particles in the periodic bands occur with a more eccentric tool setup, as compared to an aligned setup.

Interestingly, the microstructural evolution caused by increased tool eccentricity results in only negligible effects on the global mechanical properties of the joint, since failure primarily occurs in the heat-affected zone (HAZ) of the heat-treatable AA6061 alloy. However, it was found that, when a 0.2 mm kissing bond defect is present, the ‘soft zone’ of the periodic band could deviate the fracture path to force it to propagate through the stir zone, which can be potentially detrimental to the joint integrity.

Finally, concerning the FSW process, it was found that tool eccentricity negatively affects the load imposed onto the tool. Tri-axial force measurements and high-speed camera observations suggest that larger force oscillations occur with larger tool eccentricity, which may shorten tool life. However, the range of welding parameters employed in this study show negligible effect of tool eccentricity on the torque values. Peak temperature measurements of the stir zone showed close proximity values to the solidus temperature of the alloy, which suggests the occurrence of a ‘stick-slip’ mechanism that stabilizes the torque values.

In conclusion, while the results do suggest significant differences in the metallurgical morphology in the local stir zone regions caused by eccentric tool setup, the impact on the global mechanical properties of the joint is found to be negligible in thick-plate aluminum alloys. More importantly, tool eccentricity negatively affects the load imposed onto the tool, which might adversely reduce tool life and, by extension, the integrity of the FSW machine itself. It is thus suggested that tool eccentricity should be gauged and minimized prior to employing the FSW process in order to prolong tool and machine life while avoiding unintentional metallurgical property variations in the weld joint.

## **Acknowledgements**

Praise and gratitude be to Allah, for it is with His Grace and Mercy, I am able to complete this journey and add another milestone in my life.

I wish to render my utmost gratitude to my thesis supervisor Professor Adrian P. Gerlich and Professor Scott Walbridge for giving me the opportunity to pursue PhD under their supervisions. I am extremely lucky to have supervisors whose support and guidance help me achieve a very fruitful and wonderful PhD life. In addition, I would like to appreciate University of Waterloo technical staff Dr Yuquan Ding and Mark Griffett for helping with the metallurgical aspects throughout my PhD study. I would like to also express my heartfelt thanks to Michael Booth, Dr Abdelbaset Midawi, Dr Nazmul Huda, Hossein Sonbolestan, Emanuel Santos, Rafael De Araujo, Wentao Hou, Shihui Guo, Dr Rakesh Ranjan, Anthony Fleury and all Centre for Advanced Materials Joining (CAMJ) professors and members who have collaborated and supported me throughout my study period.

Finally, my heartfelt gratitude to Ministry of Education Malaysia and Universiti Malaysia Pahang for funding my entire PhD journey.



## **Dedication**

To Ayah, Dr Ahmad Shah Mohd Noor, the hero of my life, who sow the seed of this PhD more than 20 years ago even though I was too young to realize it back then. To the two strong women in my life, my Umi, Rahimi Arshad and my wife, Wan Normayani Wan Endut, the backbones of my life. It is through both of your support that I have made it thus far!

To my kids, Sarah Nafisah, Hannah Batrisyia, Uzair Ansari and Yusya' Syarif, who perplexingly be the source of motivation, laughter, stress and de-stress all at the same time. May this thesis also be a motivation for you to pursue long life learning! To Mak and Abah, whose continuous doas made this journey a very memorable and fruitful one. To my siblings (Boma, Salamah, Maryam, Hanip and Siyah), as well as in-laws (Abg Adi, Meri, Ira, Awa, Aitu, Farah and Badrul) who have been with me through thick and thin despite the distance separating us.

Finally, to the Ummah at large. May we seek knowledge for the betterment of ourselves and the people around us!

# Table of Contents

<b>Examining committee membership</b> .....	<b>ii</b>
<b>Author’s declaration</b> .....	<b>iii</b>
<b>Statement of contributions</b> .....	<b>iv</b>
<b>Abstract</b> .....	<b>vi</b>
<b>Acknowledgements</b> .....	<b>viii</b>
<b>Dedication</b> .....	<b>ix</b>
<b>List of figures</b> .....	<b>xiii</b>
<b>Chapter 1: Introduction</b> .....	<b>1</b>
1.1 Background.....	1
1.2 Problem statement and research gap.....	2
1.3 Objective.....	3
1.4 Scope and limitations.....	4
1.4.1 Base material.....	4
1.4.2 FSW process .....	4
1.5 Thesis layout .....	5
<b>Chapter 2: Literature review</b> .....	<b>7</b>
2.1 Tool eccentricity in FSW .....	7
2.2 Pin profile eccentricity.....	7
2.3 Tool eccentricity .....	15
2.3.1 Inherent tool eccentricity .....	19
2.3.2 Artificial tool eccentricity .....	24
2.4 Summary and research gap.....	27
<b>Chapter 3: Methodology</b> .....	<b>28</b>
3.1 Welding parameters and friction stir welding (FSW) tool.....	28
3.2 Sample preparation and metallurgical analysis.....	29
3.3 Electron backscatter diffraction (EBSD) analysis .....	30
3.4 Transmission electron microscopy (TEM) analysis .....	30
3.5 Tensile testing and digital image correlation (DIC) analysis.....	31
3.6 Hardness and surface roughness measurements .....	32
3.7 High speed camera (HSC) observations .....	32
3.8 Thermal cycle measurements.....	32
3.8.1 Stir zone (SZ) region.....	32
3.8.2 Heat affected zone (HAZ) region .....	33
<b>Chapter 4: Effects of tool eccentricity on similar AA6061 friction stir welding</b> .....	<b>35</b>

4.1 Introduction.....	35
4.2 Methodology.....	35
4.3 Results.....	36
4.3.1 Surface roughness analysis .....	36
4.3.2 Microstructural observations .....	38
4.3.3 Mechanical characterization .....	45
4.4 Discussion.....	48
4.4.1 Effects of pin profile on stir zone microstructure .....	48
4.4.2 Effects of tool eccentricity on stir zone microstructural morphology .....	49
4.4.3 Kinematics of tool eccentricity and material deposition mechanism .....	51
4.4.4 Tool eccentricity and kissing bond defect .....	55
4.5 Conclusion .....	56
<b>Chapter 5: Effects of tool eccentricity on dissimilar AA5052-AA6061 friction</b>	
<b>stir welds .....</b>	<b>58</b>
5.1 Introduction.....	58
5.2 Methodology.....	59
5.3 Results.....	60
5.3.1 Microstructural characterization .....	60
5.3.2 Thermal cycle analysis.....	63
5.3.3 Mechanical properties analysis .....	64
5.3.4 Texture analysis .....	69
5.4 Discussion.....	77
5.4.1 Effect of base material positioning on material mixing.....	77
5.4.2 Effect of eccentricity on material deposition.....	80
5.4.3 Effect of microstructural evolution on mechanical properties.....	82
5.5 Conclusion .....	84
<b>Chapter 6: Effects of tool eccentricity on process response variables of friction</b>	
<b>stir welds .....</b>	<b>86</b>
6.1 Introduction.....	86
6.2 Methodology.....	88
6.2.1 Force and torque analysis.....	88
6.2.2 Strain rate analysis .....	89
6.3 Results.....	91
6.3.1 Force and torque measurements.....	91
6.3.2 High-speed camera observations .....	96

6.3.3 Temperature measurements .....	98
6.3.4 Strain rate and texture analysis .....	100
6.4 Discussion .....	104
6.4.1 Force evolution in eccentricity setup .....	104
6.4.2 Correlation between force, torque and temperature .....	106
6.4.3 Correlation between strain rate and rotational speed .....	108
6.5 Conclusion .....	109
<b>Chapter 7: Conclusion .....</b>	<b>111</b>
7.1 Comprehensive summary .....	111
7.1.1 Properties .....	111
7.1.2 Performance .....	112
7.1.3 Structure .....	112
7.1.4 Process .....	113
7.2 Overall summary .....	114
7.3 Future outlook and suggestions .....	115
<b>References .....</b>	<b>116</b>
<b>Appendix A .....</b>	<b>134</b>
General properties of base metal AA6061-T6511 Al alloy .....	134
General properties of base metal AA5052-H32 Al alloy .....	135
<b>Appendix B .....</b>	<b>136</b>
Conference presentations .....	136
Journal papers .....	137

## List of figures

Figure 1-1. Schematic image of a typical FSW process. ....	2
Figure 1-2. Components of materials engineering.....	3
Figure 2-1. Schematic of material transport around the pin during FSW [97]. ....	19
Figure 2-2. Top and side plane schematic of vertical oscillation per rotation of tool due to eccentricity, which creates crests and troughs in the banded structure.....	21
Figure 2-3. Schematics ((a) to (e)) of layer stacking representing successive sequences with eccentric tool. In (e), the rotation is complete with an additional layer compared to (a). (f) Optical view of zigzag interface resulting from eccentric motion of the tool [75].....	22
Figure 2-4. Schematic of the extrusion process caused by the rotation and forward progress of an off-centred (eccentric) tool [59]. ....	23
Figure 2-5. Schematic of the shear expected (a) for the conventional view of continuous material flow during FSW and (b) within material being extruded around the tool faster than the tangential tool speed due to an off-centred (eccentric) tool for the indicated region in Figure 2-4(d) [59]. ....	23
Figure 2-6. Schematic of force distribution in the stir zone (a) without and (b) with pin eccentricity [64]. ....	26
Figure 3-1. (a) Isometric view, (b) side view, (c) top view and (d) schematic view of the typical aligned FSW tool. ....	29
Figure 3-2. Tool design for (a) aligned and (b) eccentric setup, where collet centreline is at an offset from tool centreline.....	29
Figure 3-3. Cross-sectional macrograph of the stir zone for (a) aligned sample and (b) eccentric sample. ....	31
Figure 3-4. (a) Design of tool with holes for temperature measurements. (b) Fabricated fixture with data logger casing and thermocouple ports.....	33
Figure 3-5. Thermocouple positions at mid-thickness of work pieces with their respective distances from the faying surface. ....	34
Figure 4-1. Weld surface macroscopic images of (a) aligned, (b) 0.2 mm eccentric and (c) 0.4 mm eccentric setup as well as close up weld surface SEM images of (d) aligned, (e) 0.2 mm eccentric, and (f) 0.4 mm eccentric setup, respectively. The welding speed is 63 mm/min. ....	36
Figure 4-2. 3D surface roughness profile of (a) aligned, (b) 0.2 mm eccentric, and (c) 0.4 mm eccentric setup. The welding speed is 63 mm/min. ....	37
Figure 4-3. Roughness average (Ra) and average roughness depth (Rz) of welded specimens... ..	38
Figure 4-4. Transverse plane cross-sectional macrographs of aligned (0 mm), 0.2 mm eccentric, and 0.4 mm eccentric setup with various travel speeds. Red arrows show tracer Al foils. Advancing side is at the left side of the images, while retreating side is at the right side.....	39

Figure 4-5. (a) Close up of the stir zone with the respective points for EBSD analysis. Grain size and orientation of aligned sample at the (b) inner band region, (c) outer band region, and (d) middle region. Grain size and orientation of 0.2 mm eccentric sample at the (e) inner band region, (f) outer band region, and (g) middle region. ....	40
Figure 4-6. (a) Grain size measurement regions of interest (b) Grain size of various SZ regions for aligned and eccentric setups. ....	41
Figure 4-7. TEM microstructures of the middle region for (a) aligned sample and (b) 0.2 mm eccentric sample and the bottom inner band region for (c) aligned sample and (d) 0.2 mm eccentric sample. ....	42
Figure 4-8. TEM micrographs of (a) inner band region and (b) outer band region of aligned sample, as well as (c) inner band region and (d) outer band region of 0.2 mm eccentric sample. ....	43
Figure 4-9. TEM micrographs of inner band region for aligned sample ((a) to (c)) and 0.2 mm eccentric sample ((d) to (f)) with increasing magnification. ....	44
Figure 4-10. Stir zone hardness mapping of (a) aligned setup, (b) 0.2 mm eccentric setup, and (c) 0.4 mm eccentricity setup. The welding speed is 63 mm/min. ....	46
Figure 4-11. Cross-sectional DIC images of initial local strain of (a) aligned sample and (b) 0.2 mm eccentric sample as well as final local strain right before fracture for (c) aligned sample and (d) 0.2 mm eccentric sample. Both samples contain kissing bond defect at the weld root. ....	47
Figure 4-12. Comparison of strain distribution versus location index across the mid-region traverse plane for (a) samples fractured in the HAZ and (b) samples fractured in SZ. ....	47
Figure 4-13. Overlaid image of tool pin on the stir zone of a sample. ....	49
Figure 4-14. Linear velocity of tool in (a) aligned and (b) eccentric setup during rotation. (c) Schematic relationship between the angular velocity, eccentricity and tool velocity components in welding direction [58]. Welding direction is upwards. ....	51
Figure 4-15. (a) Time dependent linear velocity of aligned and eccentric setup tool and (b) Linear velocity amplitude change due to tool eccentricity. ....	52
Figure 4-16. (a) Comparison of point travel path per rotation of tool for aligned and eccentric setup with no translational motion. (b) Schematic of APR point displacement comparison for aligned, 0.2 mm, and 0.4 mm eccentric setup. ....	53
Figure 4-17. Fracture initiating at the kissing bond in both (a) aligned sample and (b) 0.2 mm eccentric sample. ....	56
Figure 5-1. Cross-sectional macrographs of (a) A5R6, (b) A5R6-0.2, (c) A5R6-0.4, (d) A6R5, (e) A6R5-0.2, and (f) A6R5-0.4. Colour contrasts are visible between work pieces due to difference in lighting setup and slight variation in the etching period. ....	60
Figure 5-2. (a) 3-dimensional macrograph of A6R5 and longitudinal stir zone images of (b) A5R6 and (c) A6R5 along with microhardness maps. All images demonstrate the horizontal uniformity of the observed pattern throughout the longitudinal plane. ....	61

Figure 5-3. Higher magnification images of Figure 5-1(c) and Figure 5-1(f) and corresponding EDX mapping of Mg elements for regions A ((a) and (e)), B ((b) and (f)), C ((c) and (g)) and D ((d) and (h)).	62
Figure 5-4. A6R6 thermal cycle at various mid-thickness points perpendicular to the faying surface.	63
Figure 5-5. Temperature profile of various points from the weld centre.	64
Figure 5-6. Mid-thickness hardness profiles for (a) A5R6 oriented samples and (b) A6R5 oriented samples.	65
Figure 5-7. Stir zone hardness mapping of (a) A5R6 and (b) A6R5.	65
Figure 5-8. Ultimate tensile strength and elongation of samples. The bars represent the tensile strength (MPa) while the straight line and markers represent the elongation (%). Dashed lines represent tensile strength values of A5R5 and A6R6 for comparison.	67
Figure 5-9. Global stress-strain curves for similar and dissimilar welded joints.	67
Figure 5-10. Fracture surface images obtained from tensile specimens for joints (a) A6R6, (b) A5R5, (c) A6R5, and (d) A5R6. Both dissimilar welding samples show a similar mixed fracture mode to A6R6.	68
Figure 5-11. DIC images of (a) A6R5-0.4 and (b) A5R6-0.4 right before fracture. Fracture occurred in HAZ of AA6061 side.	69
Figure 5-12. Transverse macrograph of (a) A5R6, (b) A5R6-0.4, (c) A6R5 and (d) A6R5-0.4.	69
Figure 5-13. IPF maps of ND-TD plane and {111} PFs for A5R5, A5R6, and A6R5 specimens of the top region.	70
Figure 5-14. Stir zone EBSD mapping of (a) top-left, (b) top-right, (c) mid-left, (d) mid-right, and (e) bottom for A6R5.	71
Figure 5-15. Stir zone EBSD mapping of (a) top-left, (b) top-right, (c) mid-left, (d) mid-right, and (e) bottom for A6R5-0.4.	72
Figure 5-16. Recrystallization fraction of A6R5 stir zone regions: (a) top left, (b) mid left, (c) bottom. Recrystallization fraction of A6R5-0.4 stir zone regions: (d) top left, (e) mid left, (f) bottom.	73
Figure 5-17. Recrystallized fraction of stir zone regions of (a) A6R5 and (b) A6R5-0.4.	73
Figure 5-18. Schematic variation of temperature and strain in the stir zone of a friction stir weld with the different physical processes in each zones [97].	74
Figure 5-19. PFs, IPFs, and ODFs of A6R5 stir zone regions.	75
Figure 5-20. PFs, IPFs, and ODFs of A6R5-0.4 stir zone regions.	76
Figure 5-21. Ultimate tensile strength vs. temperature for various Al alloys [200].	78
Figure 5-22. Top view schematic of material deposition mechanism [97].	81
Figure 5-23. Temperature and hardness profile of A6R6 with respect to distance from weld centre.	83
Figure 6-1. Design of the (a) tool sleeve and (b) pin insert. Dimensions are in millimeters.	88
Figure 6-2. Extracted area for EBSD analysis.	90

Figure 6-3. The forces ( $F_x$ , $F_y$ , $F_z$ ) and torque ( $M_z$ ) history throughout the whole welding process for (a) A-63 (b) 0.2-63 and (c) 0.4-63 samples.....	92
Figure 6-4. 3D plots showing relationships between the longitudinal ( $F_x$ ), traverse ( $F_y$ ) and forge ( $F_z$ ) forces for (a) A-63, (b) 0.2-63 and (c) 0.4-63 under steady state welding. The red dashed lines separate the positive and negative values recorded for $F_x$ .....	93
Figure 6-5. Normalized values of the torque and tri-axial forces during steady state for 0.4-63 sample. ....	94
Figure 6-6. Force, torque and power average absolute values in steady state as a function of weld speed under different tool setup conditions: (a) Longitudinal force, $F_x$ , (b) Transverse force, $F_y$ , (c) Forge force, $F_z$ , (d) Torque, $M_z$ and (e) Power, $P$ . ....	95
Figure 6-7. Tri-axial forces maximum oscillation amplitude during steady state. ....	96
Figure 6-8. Eccentricity comparison during jog and welding process with various eccentricity setup under 63 mm/min weld speed for (a) MTI gantry FSW machine and (b) Jafo universal milling machine. ....	97
Figure 6-9. Thermal history during FSW with A-63 setup.....	98
Figure 6-10. Tool shoulder average peak temperature measured during steady state of aligned setup with (a) varying weld speed and (b) varying rotational speed. ....	99
Figure 6-11. IPF maps of (a) A-710, (b) A-1120 and (c) E-1120. The HAGBs are represented by the black lines. Welding direction is upwards. ....	101
Figure 6-12. PFs, IPFs and ODF of all samples. ....	102
Figure 6-13. Schematic of the preferred $\{111\}$ and $\{011\}$ plane orientations at the shoulder interface for (a) A-1120 and (b) E-1120 samples. ....	103
Figure 6-14. Eccentricity change in A-63 setup caused by the difference in tool pin profile. ...	105
Figure 6-15. Comparison of maximum strain rate available in literature with various welding conditions taken from [22]......	109



# Chapter 1: Introduction

## 1.1 Background

Friction stir welding (FSW) is a solid-state joining process that consolidates materials together by means of frictional heat and severe plastic deformation imposed by a rotating tool. One of the main parameters controlling this process is the tool geometry, typically consisting of a shoulder and a protruding pin. It is fixed to a spindle, which provides the rotating motion. During the process, the pin is slowly plunged into the material to plastically deform the workpiece through the stirring action, while the shoulder doubles as the main heat generator through friction and minimizes upward material expulsion [1]. Once sufficient plunge depth is achieved, the tool traverses along the faying surfaces of the workpieces. The main characteristics of the FSW process are shown in Figure 1-1. The advancing side (AS) is the side of the weld where the direction of tool rotation is the same as the welding direction, while the retreating side (RS) is the side of the weld where the tool rotation opposes the weld direction. These designations will be of importance in the subsequent chapters of this thesis.

Since its invention in the early 1990s by Wayne Thomas of The Welding Institute (TWI), UK, most of the research regarding friction stir welding has centred on processing variables related to the tool design (shape, etc.) and movement, considering their significant influence on joint microstructures, properties, and defect formation. The main parameters include rotational speed (rpm) [2]–[4], welding speed (mm/min) [5]–[7], revolutionary pitch (welding speed to rotational speed ratio) [8], tool design [9], [10] and shoulder-to-pin diameter ratio [11]–[13]. Numerous in-depth reviews and parameter optimization techniques have been reported regarding these variables [14], [15], [24]–[26], [16]–[23]. Other FSW-related reviews include numerical modelling [27]–[31], automation and process control [32]–[34], FSW of aluminum alloys [35]–[38], FSW of polymers and metals other than aluminum [39]–[42], FSW of dissimilar alloys/metals [43]–[50], and metal matrix composites [51]–[54]. However, to the best of the authors' knowledge, there has been no previous comprehensive review regarding the effects of tool eccentricity on the FSW process, despite its existence with varying degree of severity in all FSW processes.

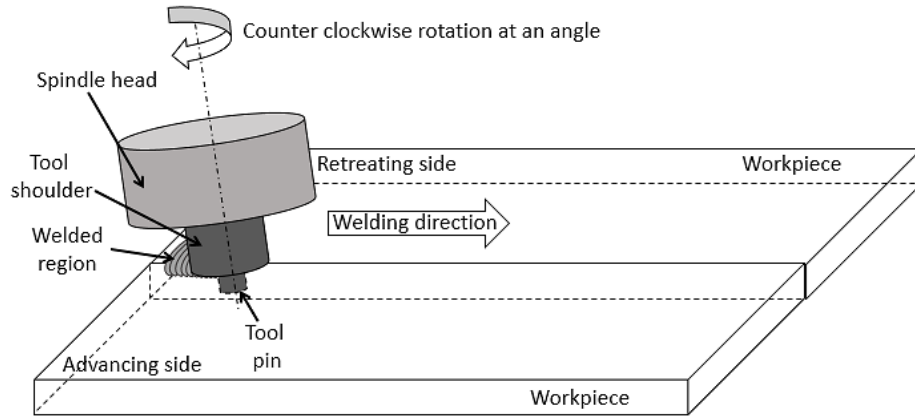


Figure 1-1. Schematic image of a typical FSW process.

## 1.2 Problem statement and research gap

Tool eccentricity during rotation, i.e. rotation of a tool, which is slightly off from the spindle rotational axis due to thread wear of the tool holder or improper fit-up of the tool in its holder, is a common phenomenon in milling operations. The improper setup creates a minute ‘wobbling’ at a certain amplitude with each full rotation. The effect of this on the milling tool’s cutting behaviour have been discussed extensively in previous works [55], [56]. However, data pertaining to the effect of tool eccentricity in FSW, which mostly operates in a similar manner, is scarce.

A comprehensive review regarding tool eccentricity will be presented in Chapter 3 [57]. Among the available literature on the issue, Guo et al. proposed that the amplitude of the banded structure visible at the weld crown of the FSW joints is increased due to tool eccentricity, which causes an upward and downward motion since FSW parameters usually involve tilting the tool forward at a slight angle of 1 to 3° [58]. Through microstructural observations, Fonda et al. suggested that the materials undergo reverse shearing, owing to the tool eccentricity inherent in any FSW operation [59]. In addition, works by Yan et al. as well as by Zaeh and Gebhard highlighted that eccentricity corresponds to variations in the process forces [60], [61].

As will be discussed in more detail in Chapter 2, most of the fundamental discussions stated in the preceding paragraph have been focused on the inherent tool eccentricity conditions (i.e.: random variance within the equipment tolerances), which is typically defined as tool eccentricity less than 0.1 mm [57]. On the other hand, several works on artificial tool eccentricity ( $\geq 0.1$  mm eccentricity) have suggested improved tensile strength [62]–[64] and enhanced material mixing

with increased tool eccentricity [62], [65], but with a limited understanding of the fundamental mechanism. Considering this, the thesis attempts to elucidate several unanswered questions pertaining to this issue, including:

- How does the tool eccentricity influence the material flow and microstructural properties of thick-plate aluminum alloys? Subsequently, how do these microstructural changes impact the mechanical performance of the FSW joint?
- To what extent does tool eccentricity affect the processing parameters in FSW, and should such change be of any concern with regards to the tool life?
- Could observations of the metallurgical and physical aspects of the weld region provide a further understanding of the fundamental mechanism(s) at play when tool eccentricity is imposed?

### 1.3 Objective

The objectives of this thesis are therefore set based on the questions mentioned in Section 1.2, but with reference to the elements of materials engineering as shown in Figure 1-2. In essence, material engineering is composed of four critical aspects, which are integrated together, namely the structure (metallurgical morphology, crystal texture, etc.), properties (microstructural, mechanical and physical), performance (tensile strength, hardness, roughness, etc.), and processing parameters. It is therefore convenient to characterize the influence of FSW tool eccentricity by employing these components and grouping the objectives accordingly.

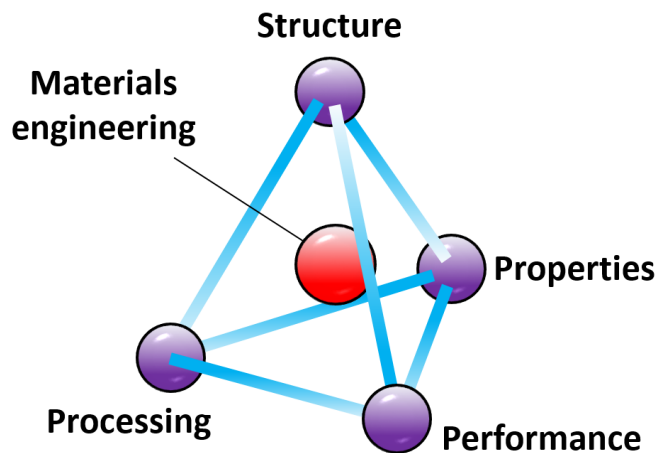


Figure 1-2. Components of materials engineering.

The three main objectives in this thesis are as follows:

- Elucidation of tool eccentricity effects on the kinematics of friction stir welding and stir zone material flow of thick-plate AA6061 aluminum alloy.
- Elucidation on the effects of tool eccentricity and base material positioning on dissimilar friction stir welding of thick plate AA5052-AA6061 aluminum alloys.
- Analysis of the change in process response variables of AA6061 Al alloy plates joined by FSW due to tool eccentricity.

The first objective attempts to explain the fundamental mechanism(s) of tool eccentricity through observing the ‘properties’ and ‘structure’ aspects. The second objective further investigates its influence on the ‘properties’ and ‘structure’ aspects with a focus on dissimilar alloy joints, with the addition of analyzing the ‘performance’ aspect as well. Finally, the third objective focuses on changes observed in the ‘processing’ aspect.

## **1.4 Scope and limitations**

### **1.4.1 Base material**

9.5-mm-thick plates of heat treatable AA6061-T651 and non-heat treatable AA5052-H32 aluminium alloys were used in this study. The general properties of both alloys are given in Appendix A.

### **1.4.2 FSW process**

Throughout the study, the butt joint configuration or bead-on-plate welding was employed. In the butt-joint configuration, two elements (e.g. plates) are laid side-by-side parallel to the rolling direction, and the FSW tool traverses linearly along the joint to achieve complete through-thickness consolidation. On the other hand, bead-on-plate welding implies that the tool is used on a single plate only. While it is rather similar to the friction stir processing (FSP) operation, a slight discrepancy lies in the fact that friction stir processes are usually concerned with modifying the surface of a given material, where the tool pin length is relatively short compared to the overall thickness of the base material. However, bead-on-plate welding usually implies that the tool undergoes full penetration of the material.

In addition, the main difference between butt joint welding and bead-on-plate welding is regarding the presence (or absence) of the remnant oxide layer from the abutting faying surfaces, usually visible in the form of a tortuous line in the stir zone known as the joint line remnant (JLR) or lazy-S [66]. In cases where full penetration is not achieved, a kissing bond defect can also form at the bottom stir zone region, which can be detrimental to the joint's strength and fatigue life [67]–[69].

Therefore, wherever the joint's integrity or material flow of the faying surface is of concern, the butt joint configuration was utilized, which is mainly the case. However, when only metallurgical/structural observations of local, specific regions in the stir zone are desired without mechanical characterization, then the bead-on-plate welding approach is used, for reasons of simplicity, while keeping all other variables constant.

Moreover, as will be explained in more detail in Chapter 3, a Jafo universal milling machine was utilized to fabricate the friction stir welds throughout the whole research. While sound welds were obtained using this machine, the machine is not equipped with real-time force and torque measurement capabilities. As such, for evaluating the 'processing' aspect of tool eccentricity, the data was collected using a separate MTI gantry FSW machine available elsewhere in the Centre de Soudage par Friction Malaxage (CSFM), at Université du Québec à Chicoutimi (UQAC) in Chicoutimi, Quebec, Canada. The role of the FSW tool and its profile is explained in detail in Chapter 3, while slight discrepancies between the setup of the Jafo milling machine and MTI gantry FSW machine are discussed in Chapter 6.

## **1.5 Thesis layout**

The thesis consists of seven chapters including this one. The subsequent chapters and their contents are outlined as follows:

In the Chapter 2, a comprehensive literature review regarding tool eccentricity is presented. Previously reported works are dissected to reveal the research gap that this thesis aims to address. Points of agreement or contradiction are also highlighted.

Next, the overall methodology of the thesis is presented in Chapter 3. This chapter summarizes the general experimental methods taken in order to obtain reliable information from the empirical observations. However, several unique methodologies are presented in the respective subsequent chapters where necessary.

Chapter 4 covers the first objective mentioned in Section 1.3. The effect of tool eccentricity on microstructural and material flow evolution of AA6061 is addressed. In addition, the kinematics of tool eccentricity are investigated to correlate the eccentric motion and the outcome in the stir zone.

In Chapter 5, the effect of tool eccentricity is further analyzed on dissimilar AA6061 to AA5052 welds through mechanical and microstructural characterization.

Next, the final objective is addressed in Chapter 6. This chapter deals with analyzing the kinetics influenced by tool eccentricity in AA6061 alloy welds, as well as looking at their effect on other process response variables such as peak temperature and strain rate.

Finally, Chapter 7 closes the loop by summarizing the important findings and relating them back to the objectives set in Section 1.3. Future work is also suggested.

## **Chapter 2: Literature review**

This chapter critically reviews the recent progress in FSW tool eccentricity research. The bulk of this chapter is based on the published manuscript: ‘Tool eccentricity in friction stir welding: a comprehensive review’, L.H. Shah, S. Walbridge, and A. Gerlich, *Science and Technology of Welding and Joining* 2019, 24 (6), 566-578.

### **2.1 Tool eccentricity in FSW**

An overview of work on FSW reveals nuances in defining the term “eccentricity” in the context of the tool geometry and movement, and so this should be addressed before hand. In general, two types of eccentricity can be defined, namely pin profile eccentricity and tool eccentricity derived from concentric oscillation. Tool eccentricity can be further divided into two categories: inherent eccentricity and artificially imposed (i.e.: intentional) eccentricity. As can be seen in the following subsections that works on inherent eccentricity focus on the inherent eccentric motion of the tool, which is mostly less than 0.1 mm. On the other hand, studies on artificial eccentricity look into eccentricity more than 0.1 mm and are mainly concerned with how artificially increasing the amplitude of eccentric motion can potentially improve the weld output. Since the effects of pin profile and tool eccentricity are caused by different stirring mechanisms, both concepts will be reviewed separately in this chapter.

### **2.2 Pin profile eccentricity**

It is commonly known that the FSW tool geometry influences the flow of plasticized material, and this has a significant effect on weld microstructures and properties. An extensive review of tool design including tool material, shoulder-to-pin ratio, and pin geometry has been discussed by Rai et al.[17], and an overview of the scale of features and diameter ratios for tools used for different material thickness is given by Zhang et al.[18]. While the tool shoulder generates most of the heat and facilitates bulk material flow, Kumar and Kailas proposed that the pin and the profile on the surface will enhance layer by layer material flow, and therefore plays an equally important role [70].

Pin profile eccentricity is a condition whereby a polygonal profile on the pin outer surface enhances material flow and local material deformation. The presence of sharp vertexes on the outer

circumference have been shown to promote local regions of high strain rate, which can serve to increase local heating and strain rates [71]. In this context, the term “eccentricity” is being used to describe the extent to which the pin shape deviates from that of a perfectly round cylinder or cone. Numerous comparative studies have compared these pin profiles to the typical straight cylindrical design as listed in Table 2-1. Straight square, threaded cylindrical and triangles, among others, have been utilized, which enhance the deformation and consolidation, allowing in lower rotation speeds to be applied and higher joint efficiency of up to 99% [72].

The improvements in joint properties have been associated with the pulsating action of the pin while stirring, which is related to the polygonal corners and the eccentricity ratio, i.e. the ratio of the dynamic volume swept by the tool to the static volume of the tool [37], [73]. Table 2-2 presents the pulse rate at 1000 rpm (pulse/s) and eccentricity ratio for various pin profiles. Note that the dynamic volume for all conditions is equal to  $\pi r^2$  where  $r$  is the radius of the cylindrical pin, while the static volume is calculated based on the volume of each pin profile.

It is clear in Table 2-2 that pulse rate increases with the number of flat faces on the pin profile. Since a hexagonal pin profile will produce 6 pulses per rotation, which is double the pulse rate produced by a triangle pin profile, its pulse rate also doubles. Additional frictional heat is generated owing to the pulsating stirring action, which offers resistance to the regular flow of plasticized material [74]. In addition, works by Gratecap et al. have shown that triangle and square tool pin profiles produce material flow patterns which feature three or four segmented layers corresponding to the three or four vertices on the tool pin [75]. Thus, more plasticized material and enhanced material flow can be predicted.



Table 2-1. Research progress on pin profile eccentricity in friction stir welding [10], [72], [82]–[91], [73], [92], [93], [74], [76]–[81].

No	Authors and year	Material and thickness	Joint type	Pin profile (mm)	Experimental observations
1	Boz and Kurt, 2004	AA1080, 5 mm	Butt joint	Straight square, threaded cylindrical	Best joint using 0.85 and 1.1 mm pitched threaded cylindrical pins
2	Fujii et al., 2006	AA1050-H24, AA5083-O & AA6061-T6, 5 mm	Butt joint	Straight cylindrical, threaded cylindrical, triangle	Straight cylindrical is best for 1050, no significant effect on 6061, varying results for 5083
3	Elangovan and Balasubramanian, 2007	AA2219, 6 mm	Butt joint	Straight cylindrical, threaded cylindrical, tapered cylindrical, square, triangle	Straight square yielded highest tensile strength (240 MPa, 60% joint efficiency*)
4	Elangovan et al., 2008	AA6061, 6 mm	Butt joint	Straight cylindrical, threaded cylindrical, tapered cylindrical, square, triangle	Straight square yielded highest tensile strength (185 MPa, 65% joint efficiency*)
5	Elangovan and Balasubramanian, 2008	AA2219, 6 mm	Butt joint	Straight cylindrical, threaded cylindrical, tapered cylindrical, square, triangle	Straight square yielded highest tensile strength (240 MPa, 60% joint efficiency*)
6	Elangovan et al., 2008	AA6061, 6 mm	Butt joint	Straight cylindrical, threaded cylindrical, tapered cylindrical, square, triangle	Straight square yielded highest tensile strength (195 MPa*)

Table 2-1. (continued)

7	Padmanaban and Balasubramanian, 2009	AZ31B magnesium alloy, 6 mm	Butt joint	Straight cylindrical, threaded cylindrical, tapered cylindrical, square, triangle	Threaded cylindrical yielded highest tensile strength (208 MPa)
8	Babu et al., 2009	AA2219, 6 mm	Butt joint	Straight cylindrical, threaded cylindrical, tapered cylindrical, square, triangle	Utilization of response surface method (RSM) to maximize tensile strength.
9	Vijay and Murugan, 2010	Al-10wt.% TiB <sub>2</sub> metal matrix composite, 6 mm	Butt joint	Straight square, taper square, straight hexagon, taper hexagon, straight octagon, taper octagon	Straight square yielded highest tensile strength (282 MPa, 99.47% joint efficiency)
10	Suresha et al., 2011	AA7075-T6	Butt joint	Square tool, conical tool	Conical tool results in better joint efficiency (66%)
11	Gopalakrishnan et al., 2011	AA6061-T6, 6 mm	Butt joint	Hexagon, taper square, taper hexagon, square, taper octagon	Taper square yielded highest tensile strength in almost all welding speed
12	Palanivel et al., 2012	AA5083-H111 and AA6351-T6, 6 mm	Butt joint	Straight square, straight hexagon, straight octagon, tapered square, tapered octagon	Straight square yielded highest tensile strength (273 MPa)
13	Mohanty et al., 2012	Si-rich Al alloy, 6 mm	Butt joint	Straight cylindrical, tapered cylindrical, trapezoidal	Straight cylindrical yielded highest tensile strength (109 MPa)

Table 2-1. (continued)

14	Kumar and Raju, 2012	Copper, 3 mm	Butt joint	Taper cylindrical, taper threaded, triangular, square, pentagonal, hexagonal	85% of joint efficiency using square tool pin
15	Ramanjaneyulu et al., 2013	AA2014-T6, 5 mm	Butt joint	Conical, triangular, square, pentagon, hexagon	Improved symmetry in hardness profile and higher peak temperature with increasing flats
16	Khodaverdizadeh et al., 2013	Pure copper, 5 mm	Butt joint	Threaded cylindrical, square	Finer grains and higher tensile strength with square pin profile
17	Xu et al., 2013	AA2219-T62, 12 mm	Butt joint	Threaded tapered with three spiral flutes, threaded tapered with triangle	Finer grains and particles with three spiral flutes profile.
18	Bahrami et al., 2014	AA7075-O, 6 mm	Butt joint	Threaded tapered, triangular, square, four-flute square, four-flute cylindrical	Triangular pin tool yields highest tensile strength. Most uniform SiC particles distribution from threaded tapered
19	Motalleb-nejad et al., 2014	AZ31B magnesium alloy, 3 mm	Butt joint	Simple cylindrical, screw threaded cylindrical, taper	Highest mechanical properties from taper pin
20	Marzbanrad et al., 2014	AA5083, 3 mm	Butt joint	Cylindrical, square	Square pin profile produced finer grains and higher strength
21	Mehta and Badheka, 2016	AA6061-T651 to electrolytic tough pitch Cu, 6.3 mm	Butt joint	Cylindrical, triangular, square and hexagonal	Cylindrical pin profile yields defect free joints

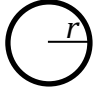




Table 2-1. (continued)

22	Goel et al., 2018	AA6063, 4.75 mm	Butt & scarf joint	Straight cylindrical, tapered cylindrical, triangle, square, hexagonal	Maximum tensile strength (162 MPa) from tapered cylindrical
----	-------------------	-----------------	--------------------------	--	--

---

\*approximation from presented graphs.

Table 2-2. Pin profiles with respective pulses and eccentricity/swept volume ratio of the tool.

Pin profile	Top view of pin profile	Pulse rate at 1000 rpm (pulse/s)	Eccentricity ratio
Straight cylindrical		-	$\pi r^2 / \pi r^2 = 1$
Straight triangle		50	$4\pi / (3\sqrt{3}) = 2.42$
Straight square		67	$\pi/2 = 1.57$
Straight hexagon		100	$2\pi / (3\sqrt{3}) = 1.21$
Straight octagon		133	$\pi / (1.17(1 + \sqrt{2})) = 1.11$

On the other hand, the eccentricity ratio for these polygonal pin profiles decreases and approaches the straight cylindrical ratio of 1 as more corners are fabricated on to the pin [72]. Elangovan and Balasubramanian highlighted that higher pin profile eccentricity such as a square tool pin profile allows incompressible material to pass around the pin profile and will result in a lower quantity of weld defects [73]. The utilization of a square pin profile in FSW was also observed to cause a higher degree of plastic deformation and a higher peak temperature. As a result, larger stir zone (SZ), finer recrystallized grain structure, and higher mechanical properties can be achieved [87], [90].

Palanivel et al. conducted a study of dissimilar FSW joints between AA5083-H111 and AA6351-T6 plates with five different pin profiles, namely: straight square, straight hexagon, straight octagon, tapered squared, and tapered octagon [74]. The results show that the highest tensile strength of 273 MPa was achieved using the square pin profile and 950 rpm rotational speed. Comparing this square pin profile with the hexagonal and octagonal, each pin profile produces 63, 95, and 127 pulses/s, respectively, at a similar tool rotational speed. Since the

intensity and duration of the pulse are inversely proportional to the number of flat faces in a straight tool, the relatively high intensity and long pulse duration of the square tool pin profile results in a severe and random layer by layer transfer of material.

Up to now, the discussion has focused on the pin polygonal profile and how it affects the weld outcome. Despite several exceptions, the majority of such comparative studies have shown that minimal polygonal edges such as what would be present in a straight triangular or straight square profile can provide optimum joint efficiency [72]–[74], [77]–[79], [85], [87], [89], [91].

The reason for this can be postulated as follows. Minimal edges provide minimal direct contact between material and tool, since the flats act as paddles in accumulating material [1]. Sheared material is periodically accumulated in these flats and subsequently deposited at the wake of the tool [94]. Despite lower pulse rates, with a larger eccentricity ratio, a larger volume of material can be temporarily ‘stored’ in the flats before periodic deposition, enhancing material mixing. More aggressive mixing can therefore be achieved with a relatively higher advance per revolution (APR, i.e. welding speed/rotational speed) as compared to cylindrical tools. Higher APR in turn reduces heat input to retard grain growth after dynamic recrystallization occurs in the stir zone, accompanied by less heat dissipation to the surrounding base metal, thus minimizing grain size and detrimental softening in the heat-affected zone (HAZ) region. The rigorous mixing also facilitates in avoiding formation of sub-surface defects such as wormhole and voids even at lower rpm and faster travel speeds.

Other than the flats, certain additional modifications to the pin profiles have reportedly also led to better results. Such modifications and subsequent improvements have included adding threads [76], [80], tapering [83], [90], [93], or adding spiral flutes [88].

However, the work by Palanivel et al. discussed earlier also reported negative effects when tapered pin profiles were used. The mixed flow region of the AA5083-AA6351 dissimilar joint observed with the square pin profile was not present in the joints made using the tapered square tool. They attributed this to the tapered pin profile being ineffective in producing the pulsating stirring action and imposing the layer by layer transfer of plasticized material. Owing to the tapered square pin tool sweeping less material when compared to the straight square pin profile, larger grains were produced in the stir zone, which resulted in poor tensile joint strength [72]. One possible reason for this observation would be the difference in flow stress of both samples, which may alter the material flow dynamics of the process.

Although minimal pin edges such as those present in triangular and square profiles are ideal to obtain optimal material mixing, and subsequently enhance mechanical properties, such tool designs also experience severe local stresses around the polygonal pin profiles. In addition, works by Colligan et al. demonstrated increase in force and torque as the number of flats are reduced [95]. The tool wear and durability could be severely compromised with a constant high shear stress imposed during the FSW process. Modelling by Mehta et al. has demonstrated that, based on FSW of 5 mm-thick AA2014 with a 1000 rpm rotational speed and 7.73 mm/s travel speed, the maximum shear stress experienced by square and triangular pin profiles is approximately 2 and 4 times the amount compared to circular pins, respectively [96]. They attribute this to the corresponding decrease in the pin's structural stiffness. Imposing high shear stresses on the tool during FSW could severely compromise the tool durability and premature fracture is a concern. One solution to this problem is the use of tapered profile to reduce the load imposed on the tool. The highest moment load in such profiles will be at the pin base, which is the strongest area. This would therefore result in prolonged tool life [1].

In summary, there is a strong consensus in literature suggesting that minimal polygonal edges in pin profiles yield optimal results, but special attention should also be taken regarding tool durability, particularly when welding high temperature hard alloys. For example, only a stepped spiral or partially formed triangular tools made from ceramic have been demonstrated for steel. It should be noted that there are other complex tool designs available in the literature, which are beyond the scope of this review but show equal if not better results. An extensive tool pin review such as the one by Zhang et al.[18] can be referenced for further information on such tool pins.

## **2.3 Tool eccentricity**

Tool eccentricity or tool runout occurs due to tool offset with respect to the spindle centre. The minor offset causes an eccentric motion, which sweeps the tool in a circular orbit during FSW. It is generally due to slight misalignment during fit-up of the tool in the spindle [97] or a minor defect in the bearings of the spindle head due to repetitive high load operations. As in common turning or milling operations, it is an inherent feature and impossible to completely eliminate. Early works by Kline and Devor have suggested that tool eccentricity influences machined surface accuracy and tool wear [56]. Since FSW closely resembles a milling/metal cutting operation in

terms of the tooling layout and motion [96], [98], it should come as no surprise that the issue of tool eccentricity has been highlighted very early during its progress by Thomas and Nicholas[99]. They pointed out that it must be part of the FSW welding process characteristics, since eccentricity allows hydromechanically incompressible plasticized material to flow more easily around the pin.

The subsequent discussions on tool eccentricity will consider research on two eccentric conditions, namely: inherent and artificial tool eccentricity. Inherent tool eccentricity results in eccentric motions, which are relatively very small and unavoidable. As mentioned, it is inherent in all milling operations. Related works on FSW report eccentricities in the range of 0.001 to 0.06 mm [59]–[61], [75]. Research on eccentric motion in this range mainly focuses on the fundamental understanding of FSW, how this motion effects the process control and response variables (welding speed, force, etc.) and its effect on the workpiece microstructure (banding, material flow, etc.). On the other hand, available literature on tool eccentricity also includes research on artificial eccentric motion. This condition is the result of deliberate tool design or clamping setup to purposely impose relatively large eccentric motion. Such conditions typically amplify the eccentric motion ranging from 0.1 to 0.8 mm. Research on eccentric motion in this range mainly focuses on analysing its effect on the joint quality. Several reported results include better material mixing, higher tensile strength, and inhibition of hooking in lap joints under eccentric conditions. Table 2-3 summarizes the research progress on both of these subtopics.



Table 2-3. Research progress on tool eccentricity in friction stir welding [58], [60], [102], [61]–[65], [75], [100], [101].

No.	Authors and year	Material and thickness	Joint type	Tool details	Eccentricity (mm)	Experimental observations
Inherent tool eccentricity						
1	Yan et al., 2007	AA2524-T351 & AA2024-T351, 6.4 mm	Butt joint	Threaded cylindrical pin (Ø7.1 mm, 6.2 mm length) and dished shoulder (Ø20.3 mm)	0.03, 0.06	Corresponds to variation in actual welding speed of $\pm 1 \text{ mms}^{-1}$ at 300 rpm
2	Fonda et al., 2007	AA2195, 25 mm	Bead-on-plate	Truncated cone-shaped pin with three flats, flat scrolled shoulder	Not mentioned	Periodical intensity variation of material deformation, reverse shearing formation
3	Zaeh and Gephard, 2010	AW-5182-H111, 3 mm	Butt joint	Threaded pin	0.001 - 0.03	Eccentricity has an influence on the process force
4	Gratecap et al., 2012	AA2017-T4 and plasticine, 4 mm	Bead-on-plate	Conical pin (3.9 mm length), pinless cylindrical tool, three and four milled faces tools	0.03	Eccentricity causes discontinuity during welding process
5	Guo et al., 2015	Pure lead, 7 mm	Butt joint	H13 pinless tool, double ring concave, Ø11.5 mm shoulder	0.06, 0.4	Banded structures are formed due to eccentricity
Artificial tool eccentricity						

Table 2-3. (continued)

1	Mao et al., 2014	AA7075, 10 mm	Butt joint	GH4169 steel, tapered threaded pin (Ø10 mm root, 9.7 mm length), flat shoulder (Ø28 mm)	0.1*, 0.2*, 0.3*, 0.4*	Highest tensile strength (249 MPa) and elongation (14%) with 0.2 mm pin eccentricity
2	Amini et al., 2015	AA5083-O, 4 mm	Butt joint	H13, flat shoulder (Ø18 mm) Ø5.5 mm and 3.85 mm length pin with conical, offset conical, half-cone-shaped and cone-shaped arched profiles	0, 1.5*	Highest tensile strength (200 MPa**) and elongation (22%**) with pin eccentricity
3	Essa et al., 2016	AA1050-H12 & AA5754-H24, 5 mm	Butt joint	H13, cylindrical pin (Ø6 mm, 4.6 mm length), 2° concaved shoulder (Ø19 mm)	0, 0.2*, 0.8*	Less temperature and lower peak temperature is generated due to eccentric pins
4	Burek et al., 2017	AA7075-T6, and 1.6 mm	0.8 Lap joint	Threaded cylindrical pin (Ø4 mm)	0, 0.1, 0.2, 0.3	Limits lap joint hooking formation on AS and RS of welds.
5	Shah et al., 2018	AA6061-T651, 9.5 mm	Butt joint	H13, tapered threaded with three flats pin (Ø5 mm root, 9.1 mm length), flat shoulder (Ø15 mm)	0, 0.2	Enhances material mixing and stir zone softening. Negligible difference in tensile strength
6	Chen et al., 2019	AA5052, 2 mm	Bead-on-plate	H13, tapered pin (Ø5 mm root, 1.75 mm length) flat shoulder (Ø12.5 mm)	0, 0.4*, 0.8*	Highest tensile strength (220 MPa) and average SZ hardness (69 HV) with 0.4 mm pin eccentricity

\*Pin eccentricity, \*\*approximated from graphs.

### 2.3.1 Inherent tool eccentricity

Using plasticine as the workpiece, Gratecap et al. reported that the origin of the eccentric movement stems from the FSW tool attachment in the tool holder of the milling machine [75]. However, minor geometrical variations in the material flow in an AA2017-T4 sample, compared to the plasticine, suggest that eccentricity may also be caused by the different transverse forces on the advancing and retreating sides of the weld. This can be understood through the simple model of material transportation around the pin during FSW shown in Figure 2-1 [61], [103]. The tool region is divided into quadrants, namely advancing/leading, retreating/leading, advancing/trailing and retreating/trailing [97]. Material shearing is initiated in the advancing/leading quadrant, transferred and accumulated throughout the retreating/leading quadrant. Finally, the collected materials are deposited in the trailing side and the cycle repeats while the tool pin simultaneously travels through the workpiece. Due to this dynamic mechanism, a normal force gradient acting on the advancing/leading and retreating/leading quadrants of the tool can be expected, which may lead to eccentric motion.

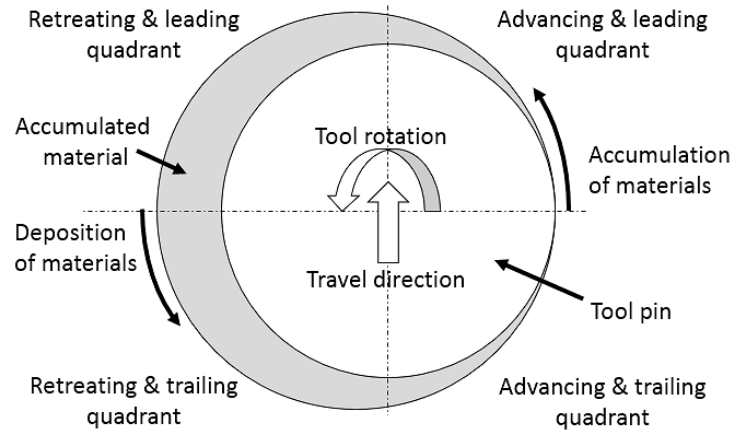


Figure 2-1. Schematic of material transport around the pin during FSW modified from [97].

The eccentric motion and its effect on the material flow were analysed using plasticine and AA2017-T4 alloy as the work piece and high-speed camera images by Gratecap et al.[75]. A small 0.03 mm eccentric movement was reported, which generated both surface and bulk striations in the model plasticine. The high-speed video (125 images/s) during the process illustrated the

formation of successive stacked layers on the trailing side of the plasticine when a cylindrical tool without a shoulder was used. The oscillatory movement was also seen to form a discontinuous welding process. Each deposited layer for each revolution is followed by an ephemeral period in which the tool loses contact with the deposited layer before a successive layer is deposited. Despite performing bead-on-plate welding, i.e. no faying surface is involved, they observed the formation of an intermittent zigzag oxide layer in the AA2017-T4 subsurface, commonly known as joint line remnant (JLR) or lazy-S shaped oxide trail [104]. While common butt joint FSW will form JLRs due to remnant oxides from the faying surface, under the bead-on-plate condition, they postulated that the oxides would principally form during this brief discontinuous period [75].

On the other hand, Zaeh and Gephard examined the effect of tool eccentricity on the process force [61]. Force measurements showed that tool runout has a major influence on the process force ( $F_x$  and  $F_y$ ) oscillating amplitude when a 0.03 mm tool runout was applied using 1400 rpm without any welding speed (0 mm/min), but this effect became negligible for extremely low runout (0.001 mm). From the given graph, it is estimated that the amplitude of the process forces for a 0.03 mm tool runout is approximately  $\pm 600$  N, while for a 0.001 mm tool runout, it is  $\leq 100$  N, respectively. Consequently, the generated oscillating process forces are seen to induce vibrations into the machine structure, which increase with increasing tool eccentricity.

Yan et al. employed a high resolution linear variable displacement transducer (LVDT) to monitor variations in the process variables of FSW applied to AA2524-T351 plates, namely the displacement of the tool,  $X$ , to monitor tool oscillations, as well as z-axis downward force,  $F_z$ , and the force acting on the tool along the translational direction,  $F_x$  [60]. The inherent tool runout in their setup was measured to be 0.03 mm (designated as low tool runout) and 0.06 mm (designated as high tool runout). Periodic variations of  $F_x$  and  $F_z$  during all FSW processes were observed, which demonstrates interaction between the workpiece and the tool motion.

Table 2-4 summarizes the results they reported for FSW on AA2524 alloy with 0.03 mm runout compared to the baseline data, i.e. no welding is involved. As can be seen, it was observed that the translational motion alone produced a lower  $X$  displacement and slightly increased oscillation of the  $F_x$  force compared to tool rotation alone. The data also suggests that the effect of tool runout is somewhat suppressed during FSW process, as suggested by the decrease in  $X$  displacement. Additionally, they have also reported variations in actual welding speed of

$\pm 1 \text{ mms}^{-1}$  at 300 rpm due to tool eccentricity. Such observations provide further fundamental understanding of how the eccentric motion of the tool affects the welding process control and response variables.

Table 2-4. Observed amplitude of periodic variations for process variables at constant tool runout (0.03 mm) for baseline experiments (no welding) and FSW of AA2524 alloy [60].

Experiment type	Tool rotation (rpm)	Welding speed (mm/min)	Displacement, $X$ (mm)	$F_x$ force (N)	$F_z$ force (N)
Baseline	300	0	0.030	13	33
Baseline	0	126.6	0.015	28	30
Baseline	300	126.6	0.030	80	33
FSW	300	126.6	0.015	700	180

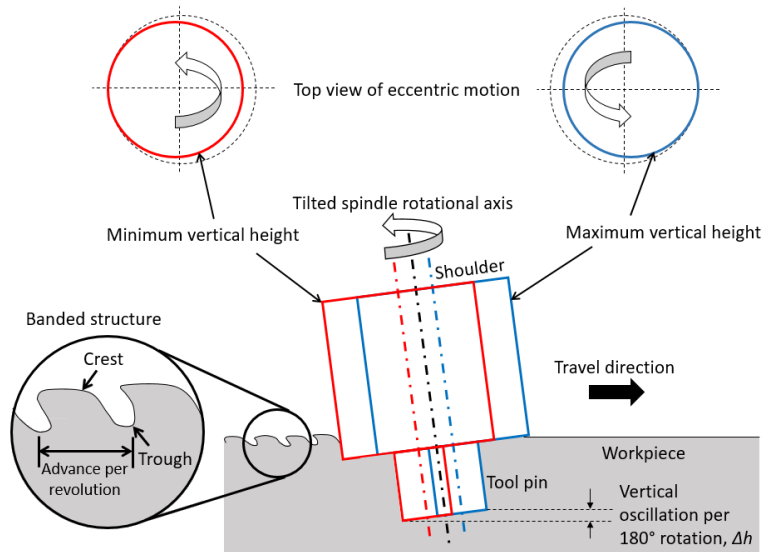


Figure 2-2. Top and side plane schematic of vertical oscillation per rotation of tool due to eccentricity, which creates crests and troughs in the banded structure.

Among other FSW features that are theorized to originate from the tool's eccentric motion is the banded structures at the weld's top surface, as shown in Figure 2-2 [58], [105]. Banded structures are periodic repetitions of crests and troughs formed at each advance-per-revolution (APR, i.e. ratio of weld speed over rotational speed) of the tool during the FSW process. Although

they are formed in all FSW samples including setups where no tilt angle is imposed, Guo et al. have suggested that the average height between the crests and troughs are larger with increased tool eccentricity, owing to the increase in vertical oscillation per rotation of the tilted tool (Figure 2-2) [58]. In addition, in their work on the influence of tool shoulder contact conditions on the material flow, Doude et al. have also considered the effect of the vertical oscillation to be the reason behind elongated Pb tracers observed embedded into the workpiece after FSW [105].

Gratecap et al. further explain that regardless of the tool's eccentricity, the forward displacement of tool after each rotation will remain constant [75]. However, the volume of material processed will increase with increasing eccentricity, generating thicker layers of weld bands. Figure 2-3 illustrates the layer stacking representing successive sequences with eccentric tool.

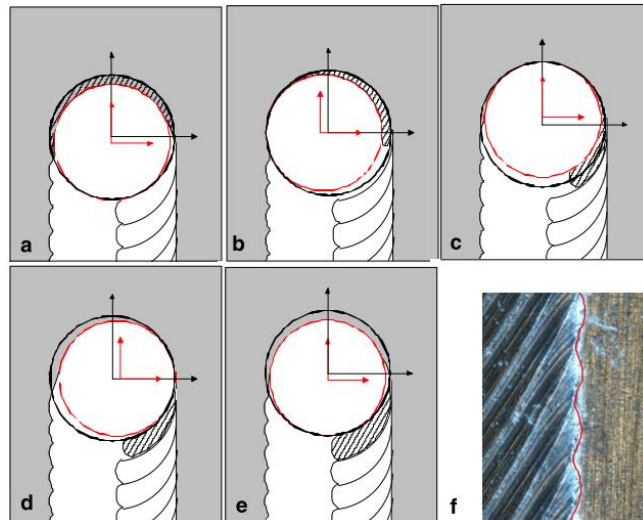


Figure 2-3. Schematics ((a) to (e)) of layer stacking representing successive sequences with eccentric tool. In (e), the rotation is complete with an additional layer compared to (a). (f) Optical view of zigzag interface resulting from eccentric motion of the tool [75].

Where material flow is concerned, initial works by Fonda et al. have suggested that eccentric oscillation magnitude influences material flow in AA2195 [100]. Large oscillations will cause the instantaneous speed of the tool to exceed the welding speed. Thus, tool motion will be dominated by the eccentricity. Measured tool forces along the longitudinal and transverse direction will vary periodically between positive and negative values, causing the welding speed to vary similarly, as claimed independently by Yan et al.[60]. This will result in continuous material

extrusion through several tool rotations before being deposited in the wake of the tool.

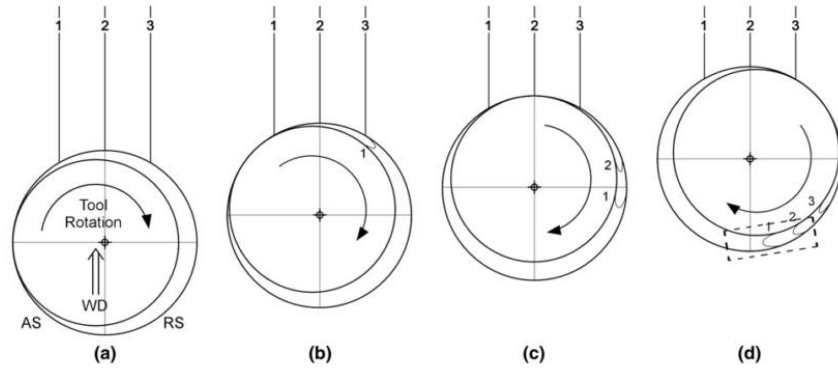


Figure 2-4. Schematic of the extrusion process caused by the rotation and forward progress of an off-centred (eccentric) tool [59].

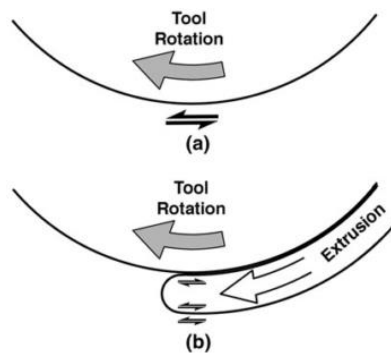


Figure 2-5. Schematic of the shear expected (a) for the conventional view of continuous material flow during FSW and (b) within material being extruded around the tool faster than the tangential tool speed due to an off-centred (eccentric) tool for the indicated region in Figure 2-4(d) [59].

In another work, Fonda et al. further proposed reverse shearing formation of material. As the eccentric tool oscillates forward in the welding travel direction, material will be removed from in front of the tool and extruded around the tool to be deposited in the tool wake (see Figure 2-4) [59]. As shown in Figure 2-5, extrusion of the material will be faster than the tangential speed of the tool, causing the inner and outer edges of the extruded material to experience different shear strain orientations. While the typical sense of shear is retained at the outer edge of the extruded material, a reverse sense of shear develops at the inner edge, closest to the tool. They claim that this feature depends to a certain degree on the magnitude of the eccentric motion. However, since

eccentricity is inherent in typical friction stir welds, the proposed extrusion can be considered a general property of the FSW process.

### **2.3.2 Artificial tool eccentricity**

There is very limited data regarding artificial tool eccentricity. As mentioned earlier, most papers on this issue focused on its effects on the joint's mechanical and microstructural properties, while works on the fundamental understanding of its mechanism is scarce. Several notable works are highlighted here, and future potential research directions are discussed.

Burek et al. conducted FSW experiments on thin sheets of AA7075-T6 in a lap joint configuration with up to 0.3 mm tool eccentricity [102]. They concluded that the eccentric motion affects the weld mixing depth, the weld width, and the shape of the contact line (hooking effect, i.e. deformed kissing bond at the faying surface). Rougher weld bead surfaces were produced as a larger tool eccentricity was used. They attributed this trend to higher weld temperature, which plasticizes more material than required. Another viable explanation would be that it is due to more material being processed with each APR as suggested by the authors of references [58], [75]. In addition, while eccentric oscillations of up to 0.3 mm are considered to limit the formation of lap joint hooking, it was also observed that eccentric setups produced voids at the joint interface when the APR is too high. Highest tensile strength values were recorded for non-eccentric tool and minimal eccentricity (0.1 mm) setups.

The effects of limiting the eccentricity to the pin (and centring the shoulder) were conducted by Mao et al. through a specially designed tool where the pin is fabricated with an offset from the rotating axis of the tool shoulder [62]. A pin offset of up to 0.4 mm was utilized on 10 mm-thick AA7075 alloy. A 0.2 mm pin offset resulted in highest tensile strength (249 MPa) and elongation (14%). These observations are attributed to better interfaces, finer grains, and more dispersive secondary phase particles, which resulted from the enhanced strain rates applied during stirring. The 0.2 mm offset sample showed the largest stir zone width and area, and fractured at the base metal region, in contrast with the other samples, where fracture propagated in the HAZ of the retreating side. The pin offset was further increased up to 0.4 mm. However, this further increase was seen to deteriorate the mechanical properties. The authors attributed this to more



severe deformation and higher peak temperature, which may temporarily change the sticking condition of the tool-material interaction, towards a slip condition instead. Slipping of the tool causes a narrower extrusion area of the material that is not directly in contact with the tool, hence the stir zone area decreases compared to the 0.2 mm offset.

On the other hand, similar pin offset studies on AA1050-H12 and AA5754-H24 were performed by Essa et al. to investigate the heat generation of the tool [101]. Peak temperatures were measured using an infrared measuring device on the top surfaces of the advancing side of the weld joints. Experimental results and numerical simulations for both alloys implied that, while more heat is being generated, less temperature and a decrease in peak temperature is observed when larger pin offsets up to 0.8 mm were used. Even so, details such as the exact distance between the measured temperature location to the faying surface and possible error from emissivity of aluminium is not disclosed. Therefore, the reason for the decrease is not clearly understood.

Works by Shah et al. on 9.5 mm-thick AA6061-T6 alloy using Al foil tracers at the faying surface of the workpieces have reported better material mixing in the stir zone when a 0.2 mm eccentric motion is imposed (by offsetting a tool fabricated with the pin centred with respect to the shoulder) [65]. In addition, enhanced stir zone softening was also observed due to the tool eccentricity. However, the effect of the tool eccentricity on the global stress-strain curve of the material under uniaxial tensile testing was found to be negligible.

Recent work by Chen et al. has shed some light regarding the mechanism in which the tool eccentricity enhances the material flow [64]. In their work, 2 mm-thick AA5052 alloy was friction stir processed (FSPed) using tool a with different pin eccentricities of 0, 0.4, and 0.8 mm. Enhanced material mixing manifested in the form of ‘onion-ring’ shaped lamellar structures and decreased average grain sizes in the SZs were observed for both 0.4 and 0.8 mm pin eccentricity compared to a normal tool. The mechanism behind the improvement can be explained through the schematic diagram in Figure 2-6.

As shown in Figure 2-6, the process consists of several force components from the shoulder (plunge force), the pin (contact force,  $F_c$ ) and the backing plate (extrusion force). The contact force from the pin can be broken down into shear force ( $F_N$ ) and push force ( $F_T$ ). However, with the pin eccentricity, an additional eccentric force ( $F_E$ ) is introduced during tool rotation, increasing the

shear force,  $F_{N'} = F_N + F_E$ , which enhances tool-material interaction, expanding the lower region of the SZ and forming the onion-ring structure [64].

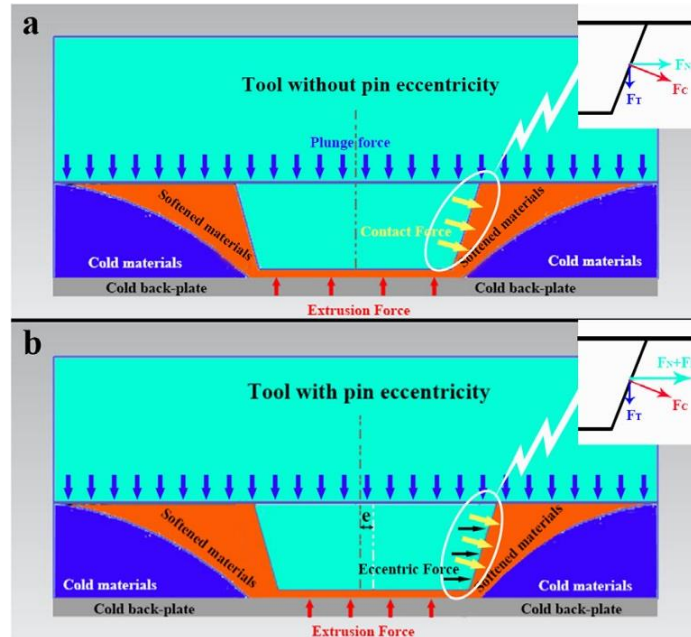


Figure 2-6. Schematic of force distribution in the stir zone (a) without and (b) with pin eccentricity [64].

The microstructural mechanical characterization revealed that a 0.4 mm eccentricity demonstrated the lowest average grain size, giving it a slightly higher hardness and ultimate tensile strength, while roughly maintaining similar elongation. Similar to the Mao et al.[62], they postulated that this is due to higher heat generation with a 0.8 mm pin eccentricity, which may have caused local melting at the tool interface, causing the tool-material interaction to temporarily transitioned from a stick condition to a slip condition [106], [107]. However, no temperature measurements were reported in either of these works to support this claim.

It is interesting to note that both works report different optimum pin eccentricity. This can be attributed to the difference in workpiece (material and thickness) as well as tool design. Given the stark difference in the results, further iterations of this study on different setups would be worthwhile to investigate.

## 2.4 Summary and research gap

With regards to pin eccentricity, it can be seen that having minimal polygonal edges such as triangular and square profiles is beneficial for producing improved joint quality. It is due to this fact that a triangular shaped pin profile (tri-flats) was utilized throughout this study. However, a significant increase in the resultant maximum shear stress is imposed, which can severely reduce tool life. Enhanced tool design features such as taper and threading, which were also integrated in this study needed to be considered in efforts to establish optimal tool designs.

From the standpoint of the typical FSW process, tool eccentricity in a typical setup is inherent and impossible to prevent. Given that such eccentricity does affect the process forces, weld speed, overall weld features, material flow, and microstructural texture, care should be taken when installing the tool into the spindle head and minimal eccentricity should be measured prior to the welding process to ensure consistent welds and prolonged tool durability.

Even so, amplifying the eccentricity above 0.1 mm has shown interesting results such as inhibiting the hooking effect, improving material mixing, and increasing the joint tensile strength. However, as mentioned earlier, consideration should also be taken regarding the additional forces imposed on the tool, which may deteriorate tool life.

While numerous fundamental research studies have been done regarding inherent eccentricity to understand its effects on the properties of the resulting weld, the same cannot be said regarding artificial eccentricity. Indeed, works on artificial eccentricity in most cases focus on how the control variables affect the metallurgical and mechanical output, but lack discussions elucidating the fundamental mechanism behind the tool eccentricity effects and how tool eccentricity also affects the process variables. In addition to the metallurgical and mechanical aspects, it is therefore equally important that possible changes in variables such as peak temperature, force, and torque, as well as the strain rate associated with tool oscillation be characterized in future studies. A holistic picture can then be drawn to link tool eccentricity with the mechanical and microstructural changes observed.

## Chapter 3: Methodology

To avoid repetition, this chapter presents the general metallurgical and mechanical characterization methodologies employed throughout the thesis. Wherever relevant, additional specific methodologies are presented in the subsequent chapters.

### 3.1 Welding parameters and friction stir welding (FSW) tool

The welding process were conducted using a 7.5 HP Jafo FWR40J universal milling machine. The overall welding parameters used in this study are tabulated in Table 3-1. The weld speed and rotational speed were set based on preliminary experiments and prior literature, taking into consideration the capability of the machine, the thickness of the materials and the maximum 0.4 mm eccentricity employed which may impose additional loading on the tool.

Table 3-1. Welding parameters.

Welding parameters	Value
Tool tilt angle	2.5°
Plunge rate	16, 22 mm/min
Dwell time	5, 10 s
Weld speed	45, 63, 90, 125 mm/min
Rotational speed	710, 900, 1120, 1400 rpm
Tool eccentric setup	Aligned, 0.2 mm, 0.4 mm eccentricity

Welds were made using a H13 steel tool with M6-threaded tool with tri-flats and an 8° taper, as shown in Figure 3-1. The shoulder and pin root diameter were 15 mm and 6 mm, respectively, while the pin length was 9.3 mm.

As depicted in Figure 3-2(a), the aligned tool setup with negligible eccentricity ( $< 0.05$  mm) can be achieved by firmly clamping the tool to the spindle head using a typical collet. To obtain the unique and consistent eccentric feature, the diameter of the tool shoulder's top region was thinned down with the desired offset and fixed into the spindle head accordingly, as shown in Figure 3-2(b). A dial gauge was utilized to measure and ensure consistency of eccentric motion before and after the welding process. The tolerance of the eccentricity was  $\leq 0.05$  mm.

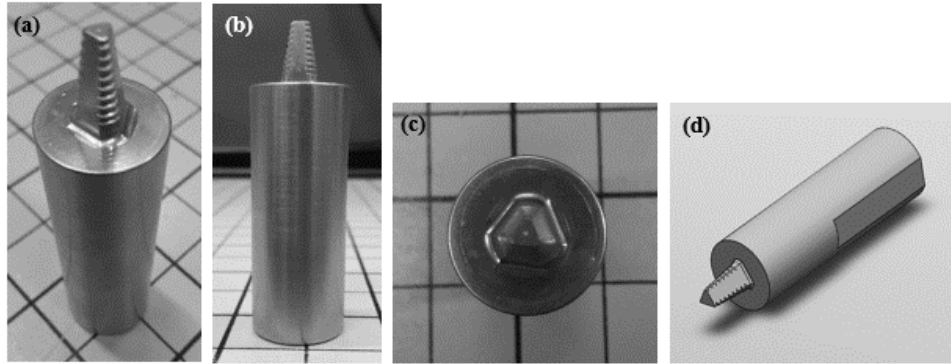


Figure 3-1. (a) Isometric view, (b) side view, (c) top view and (d) schematic view of the typical aligned FSW tool.

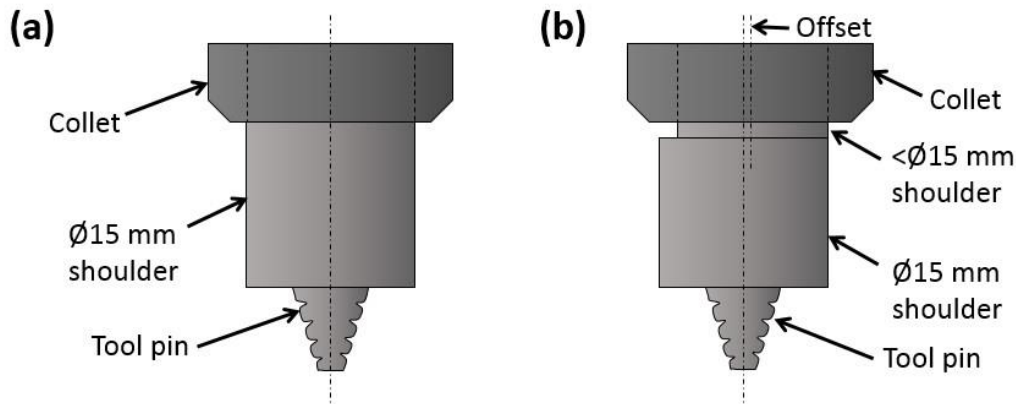


Figure 3-2. Tool design for (a) aligned and (b) eccentric setup, where collet centreline is at an offset from tool centreline.

### 3.2 Sample preparation and metallurgical analysis

To avoid any further heat treatment after the welding process, the welded specimens were cold mounted after being cut accordingly. The specimens then undergo standard aluminum alloy grinding and polishing techniques with final polishing of 1  $\mu\text{m}$  colloidal silica.

In most cases, Keller's reagent (a mixture of 190 ml  $\text{H}_2\text{O}$  + 5 ml  $\text{HNO}_3$  + 3 ml  $\text{HCl}$  + 2 ml  $\text{HF}$ ) was used as etchant. Etching time was approximately 60 s. In some cases, to observe grain boundaries, other etching processes were utilized, such as using Weck's reagent (100 ml  $\text{H}_2\text{O}$  + 4 g  $\text{KMnO}_4$  + 1 g  $\text{NaOH}$ ) for approximately 15 s, modified Poulton's etchant (mixture of two chemical solutions of 1 ml  $\text{H}_2\text{O}$  + 6 ml  $\text{HNO}_3$  + 1 ml  $\text{HF}$  + 12 ml  $\text{HCl}$  and 25 ml  $\text{HNO}_3$  + 1 g  $\text{H}_2\text{CrO}_4$  + 10 ml  $\text{H}_2\text{O}$ ) for approximately 5 s, or through electro-etching using Barker's reagent

(200 ml H<sub>2</sub>O + 6 ml HBF<sub>4</sub>) as the electrolytic medium, with Al foil as the cathode and the sample as the anode using a voltage of 20 V.

For microscopic observations, an Olympus NTB 3558 optical microscope was utilized. Scanning electron microscopy (SEM) and energy dispersive X-ray spectroscopy (EDX) analysis were conducted using an UltraPlus field emission scanning electron microscope (FESEM) to reveal elemental mapping of specimens.

### **3.3 Electron backscatter diffraction (EBSD) analysis**

To observe in detail the microstructural and texture evolution, 10 mm × 10 mm × 1 mm specimens were prepared by standard sample preparations and evaluated using electron backscatter diffraction (EBSD) analysis. This involved Ar<sup>+</sup> ion milling the surface, and imaging with a Zeiss Sigma field emission scanning electron microscopy (FESEM) equipped with an Oxford AZtecSynergy system with EBSD acquisition, available in nanoFAB Fabrication and Characterization Centre, University of Alberta, Canada.

Alternatively, EBSD analysis was also performed using a JEOL JSM-7000F equipped with a Schottky field emission gun and a Nordlys II EBSD Camera with HKL Channel analysis software to process inverse pole figure maps, available in Canadian Centre for Electron Microscopy at McMaster University, Hamilton, Canada. Both EBSD characterization was performed with a 1 μm step size on a 150 × 150 grid. In both cases, the final stages of sample preparation were done by the respective operators to ensure reliable results.

### **3.4 Transmission electron microscopy (TEM) analysis**

To evaluate dislocation density and particle evolution in specimens, transmission electron microscopy (TEM) analysis was conducted in Canadian Centre for Electron Microscopy (CCEM) at McMaster University, Hamilton, Canada, using a JEOL 2010F system operating at 200 kV. TEM samples were initially cut at middle and bottom region parallel to the top plane of the stir zone using a precision cutter machine into 15 mm × 10 mm × 1 mm coupons. Next, the specimens were carefully ground down to a thickness of ~0.15 mm to ensure the desired region (shown as thick red lines in Figure 3-3) of the samples can be extracted. The samples were sent to CCEM and the final stages of the sample preparation involving disc cutting and thinning was done using

precision die set to ensure deformation was not imposed on the specimen. The samples were then punched into 3 mm-diameter disks and underwent jet electropolishing in nitric acid/methanol solution at  $-50\text{ }^{\circ}\text{C}$  before undergoing TEM analysis. Note that the terminologies presented in Figure 3-3 will be explained in detail in Chapter 4.

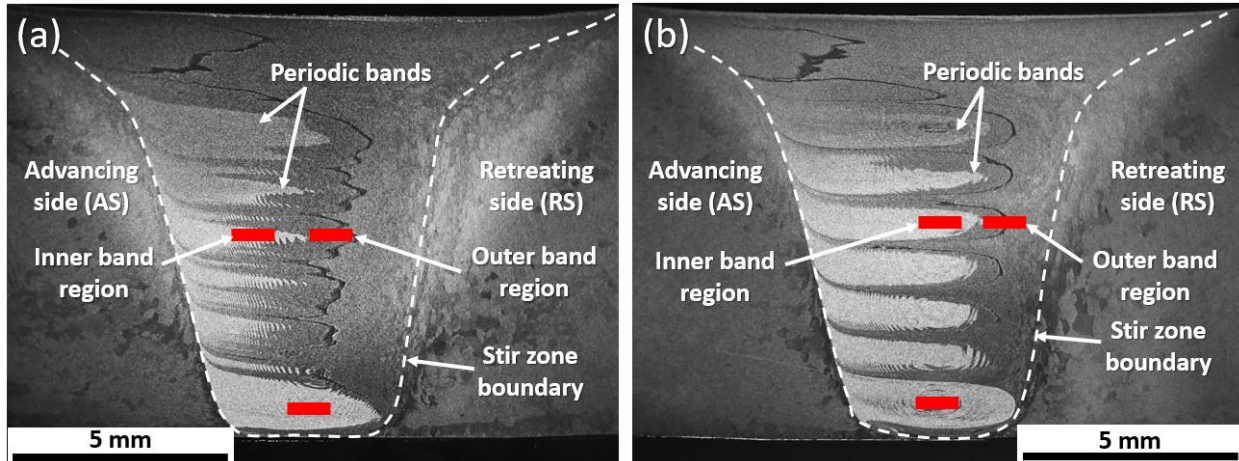


Figure 3-3. Cross-sectional macrograph of the stir zone for (a) aligned sample and (b) eccentric sample.

### 3.5 Tensile testing and digital image correlation (DIC) analysis

For mechanical characterization, samples were fabricated into ASTM-E8 standard dog-bone-shaped coupons (50 mm gauge length and 12.5 mm width) and subjected to uniaxial quasi-static tensile testing with a crosshead speed of 2 mm/min and initial calculated strain rate of  $0.00067\text{ s}^{-1}$ . To determine yield strength values more accurately, an extensometer was also integrated in the test. Subsequently, an SEM was used to observe the fracture surface of the tensile samples.

In addition, a digital image correlation (DIC) technique was also conducted using a Correlated Solutions system with VIC3D software. 2 mm-thick welded samples were prepared to further examine the local strain in the transverse plane during uniaxial tensile loading on a Tinius Olsen HK10T servo-mechanical tensile frame (10 kN maximum load capacity). Isotropic behaviour is assumed throughout the thickness of the samples. The samples were spray painted with fine black speckles on top of a white background prior to testing. The DIC was performed using 29 subsets and a step size of 7. The crosshead speed of the uniaxial tensile testing was 1 mm/min. While in some cases Al foil was inserted between the abutting base materials for

material flow observations (Chapter 4), no Al foil was inserted in the fabricated samples for tensile testing to maintain validity of the results.

### **3.6 Hardness and surface roughness measurements**

Vickers hardness maps and cross-weld profiles were obtained using a Clemex automated Vickers microhardness tester using a 0.2 kgf load and 10 s dwell time with 0.5 mm indent intervals. To analyze the surface roughness of the samples, a JEOL JSN 6460 SEM device and a Keyence 3D laser scanning confocal microscope with its respective software were utilized. All mechanical characterizations were taken at least 10 days after the welding process to allow natural aging and stabilization of the specimens.

### **3.7 High speed camera (HSC) observations**

To observe the change in the tool eccentricity before welding (jog) and during the welding process, a Photron FASTCAM high-speed camera (HSC) with a 500 frames-per-second (fps) setup was used to capture close up images of the tool. The HSC system was fixed on the stage behind the tool and opposite the welding direction, while a bright light source was fixed in front of the tool to give a sharp contrast between the tool and the surrounding for accurate measurements. Image data was recorded using Photron FASTCAM Viewer software and subsequently analyzed using Fiji image analysis software. Three separate measurements were taken for each set of conditions to ensure consistency.

### **3.8 Thermal cycle measurements**

#### **3.8.1 Stir zone (SZ) region**

Thermal history of the tool during the FSW process was conducted using an Omega K-type thermocouple, which was embedded at the middle of the shoulder surface as shown in Figure 3-4(a). The thermocouple was fixed using Omegabond “600” high temperature chemical set cement. Careful steps were taken to expose the probe of the thermocouple to insure direct contact with the workpiece during welding in order to obtain real time workpiece measurements. The



thermocouple was connected to an MSR145 data logger that was secured in a specially designed fixture, which rotates with the spindle, as shown in Figure 3-4(b).

The sampling rate was 1 Hz and at least three welds were performed for each parameter conditions to ensure repeatability of temperature measurements. Successive welds were done after the tool, workpiece and backing plate is cooled down to ambient temperature. After the temperature measurements, the thermocouple was recalibrated against a reference thermocouple in water between the ambient temperature and boiling point to take into account the slight alterations of the thermocouple position arising from the rigorous forces during the welding process to ensure accurate temperature reading. It is also worth to note that, while ideal, it was not possible to calculate the heat input due to the absence of torque measurement capability on the machine.

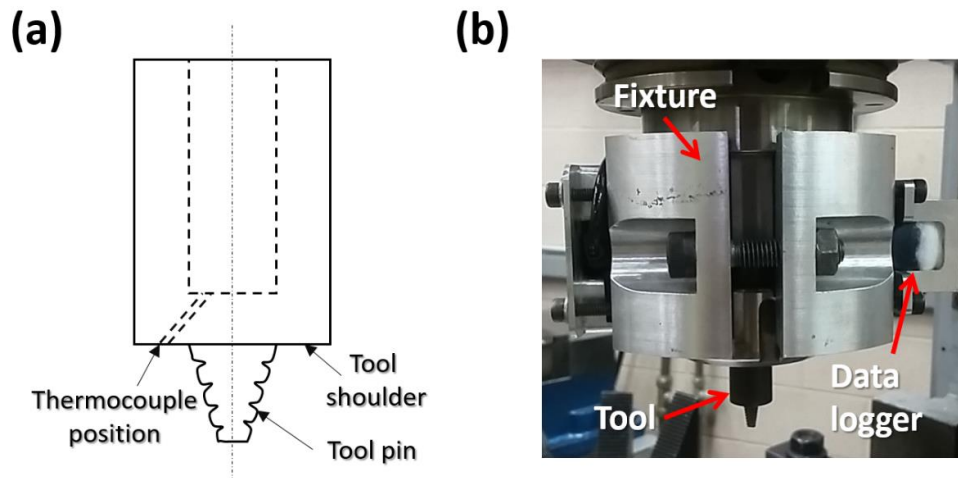


Figure 3-4. (a) Design of tool with holes for temperature measurements. (b) Fabricated fixture with data logger casing and thermocouple ports.

### 3.8.2 Heat affected zone (HAZ) region

To measure the thermal cycle of heat affected zone (HAZ) region of the work piece, 6 thermocouples were fixed inside 1 mm-diameter drilled holes mid-thickness of the work pieces in welding traverse direction (Figure 3-5). Similar Omega K-type thermocouples were positioned 10 mm, 15 mm, and 20 mm from the original faying surface, both on the advancing side (AS) and the retreating side (RS), respectively. The thermal history was recorded by a National Instruments data acquisition system using a 1 Hz sample rate.

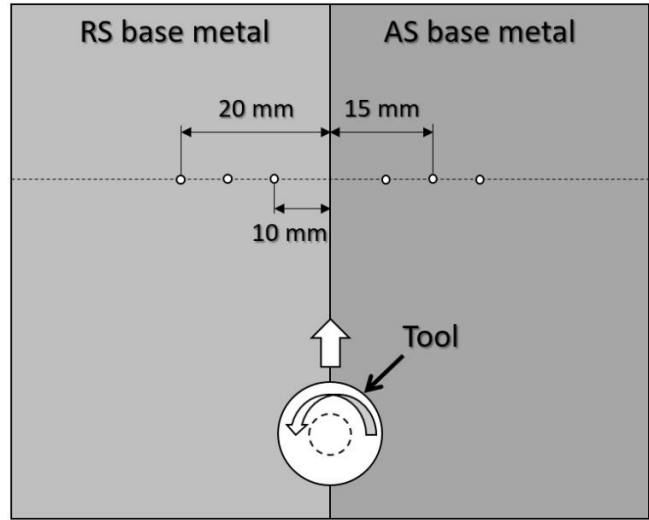


Figure 3-5. Thermocouple positions at mid-thickness of work pieces with their respective distances from the faying surface.

## **Chapter 4: Effects of tool eccentricity on similar AA6061 friction stir welding**

This chapter covers the first thesis objective by presenting metallurgical and mechanical characterizations to elucidate the kinematics behind tool eccentricity. The bulk of this chapter is based on the published manuscript: 'Influence of tool eccentricity on the material flow and microstructural properties of AA6061 aluminum alloy friction stir welds', Luqman Hakim Ahmad Shah, Abdelbaset R.H. Midawi, Scott Walbridge and Adrian Gerlich, *Journal of Alloys and Compounds* 2020, 826, 154219.

### **4.1 Introduction**

As mentioned in Section 2.2.2, information is limited concerning the effects of artificial tool eccentricity on the mechanical and microstructural properties of the joint workpiece. Burek et al. tested tool eccentricity up to 0.3 mm on FSW lap joining of 0.8 mm and 1.6 mm thick AA7075-T6 sheets and showed that eccentricity limits the hooking phenomenon in lap joints at the expense of forming voids, but at the same time affects the mixing zone depth, as well as the weld width [102]. Mao et al. and Chen et al. have also reported that a maximum tensile strength in FSW of AA7075 and AA5052 Al alloy, respectively, could be achieved when specially designed tools with pin eccentricity are utilized [62], [64]. Furthermore, initial findings by the authors have suggested better material mixing but enhanced softening in the stir zone of a thick AA6061-T651 alloy plate when 0.2 mm tool eccentricity is imposed, but the tensile strength remains similar [65].

Despite the reported improvements, the understanding of the mechanisms related to tool eccentricity and how they influence the properties of the joint remains scarce. Therefore, this study aims to expand the fundamental understanding of the effects tool eccentricity has on the mechanical and metallurgical properties of AA6061 aluminum alloy FSW joints.

### **4.2 Methodology**

In addition to the experimental methods listed in Chapter 3, to further elucidate the detrimental effect of tool eccentricity, another batch of welds were conducted using a shorter tool pin length of 8.9 mm (compared to the 9.3 mm pin length generally used) to artificially form

kissing bond defects at the weld root. Kissing bond defects form due to incomplete consolidation of the weld root, commonly due to insufficient tool plunge depth [66], [108]. Tensile mechanical property measurements were subsequently conducted (refer to Section 3.5) to understand the interaction between tool eccentricity and the presence of this defect.

## 4.3 Results

### 4.3.1 Surface roughness analysis

Figure 4-1 presents the top view of the weld surface for all tool setups under 63 mm/min welding speed. A stereoscope was utilized to obtain the macroscopic images (Figure 4-1(a) to (c)) and close-up microscopic images were taken using scanning electron microscopy (SEM) (Figure 4-1(d) to (e)). In general, a relatively smooth surface can be seen for the aligned setup, but rough surfaces were obtained when tool eccentricity is used, depicted by sporadic black dots visible in Figure 4-1(b) and (c). These rough surface observations have also been reported by others [62], [102].

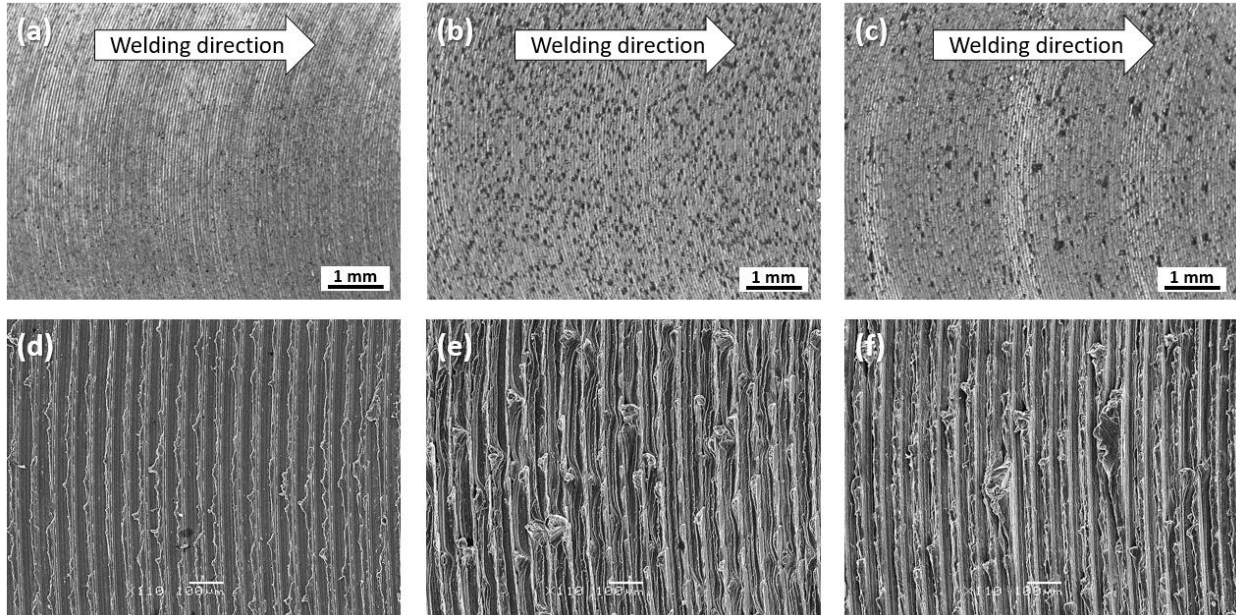


Figure 4-1. Weld surface macroscopic images of (a) aligned, (b) 0.2 mm eccentric and (c) 0.4 mm eccentric setup as well as close up weld surface SEM images of (d) aligned, (e) 0.2 mm eccentric, and (f) 0.4 mm eccentric setup, respectively. The welding speed is 63 mm/min.

The close-up SEM images show that, while the aligned sample exhibits a relatively smooth surface, the observed black dots in the eccentric setups originates from excess material being deposited intermittently while the tool is traversing, suggesting a change in material deposition mechanism. Although the frequency of these clusters of excess material is maximized while using 0.2 mm of eccentricity, the clusters are much larger and more dispersed when 0.4 mm eccentricity is used, as depicted in Figure 4-1(c) and (f).

Figure 4-2 depicts the 3D surface roughness profile of the specimens produced with aligned and eccentric tooling, with a 2D representation of the peaks and valleys of the weld bands. The topology is formed by averaging 10 line values running longitudinally through the middle of the weld beads for each specimens. The 2D topology of the weld bead show fairly consistent periodical shape for the aligned setup, but become more irregular as the eccentricity setup increases. The roughness average ( $R_a$ ) and average roughness depth ( $R_z$ ) of welded specimens are shown in Figure 4-3. A general trend of higher  $R_a$  and  $R_z$  can be seen with increasing eccentricity for all welding speed conditions. In addition, error bars are seen to be large for 0.4 mm eccentric setups. This can be attributed to the sporadic excessive material deposition on the weld surface, contributing to significant surface irregularities and inconsistencies.

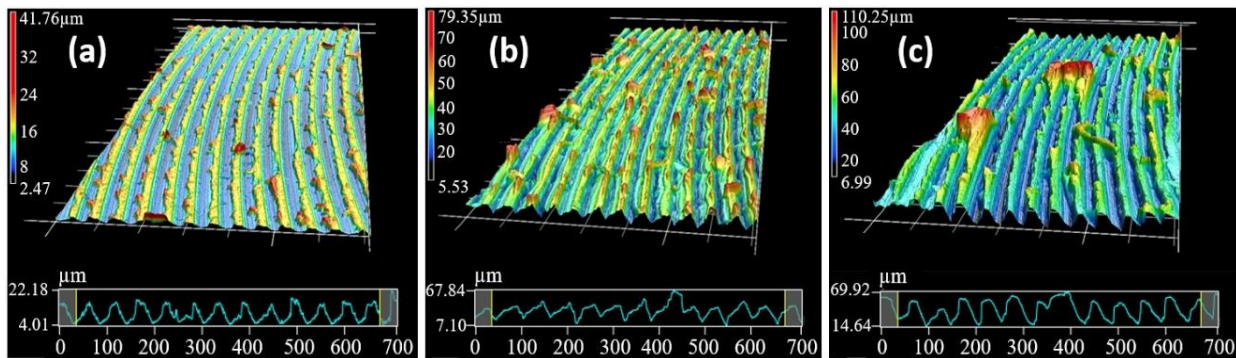


Figure 4-2. 3D surface roughness profile of (a) aligned, (b) 0.2 mm eccentric, and (c) 0.4 mm eccentric setup. The welding speed is 63 mm/min.

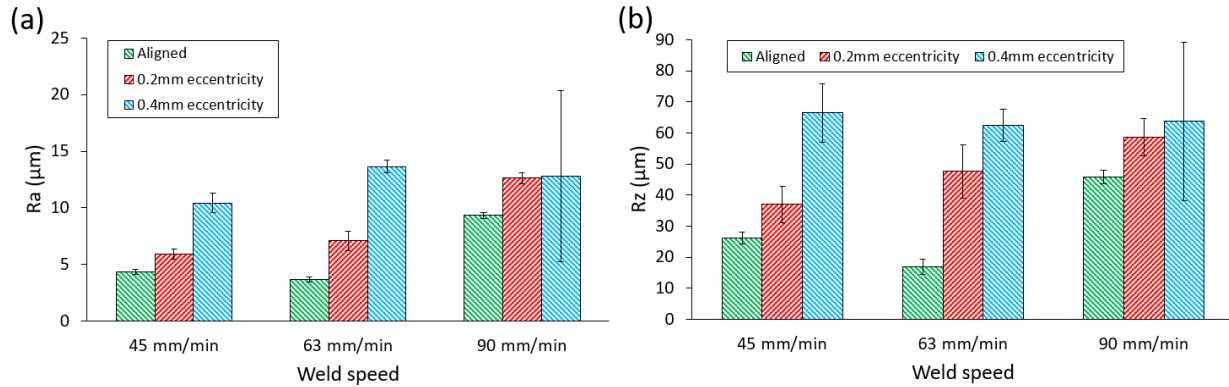


Figure 4-3. Roughness average (Ra) and average roughness depth (Rz) of welded specimens.

Through the weld surface striations in the macroscopic images, the advance per revolution (APR) or revolutionary pitch of samples at the various travel speeds and eccentricity setups were also measured. The measured APR for all samples with different eccentricity setups were found to be constant at  $0.040 \pm 0.001$  mm,  $0.055 \pm 0.001$  mm and  $0.079 \pm 0.001$  mm for 45 mm/min, 63 mm/min and 90 mm/min travel speeds, respectively, which are in good agreement with the calculated APR of 0.040 mm/rev, 0.056 mm/rev and 0.080 mm/rev. This confirms that the APR is maintained with the eccentric setup of up to 0.4 mm.

### 4.3.2 Microstructural observations

Figure 4-4 depicts the traverse plane macrograph of aligned and eccentric setups. The boundaries of the BM, HAZ, TMAZ, and SZ microstructural regions were approximated using yellow dashed lines. The Al foil, which was used as a tracer between the sheets, can be observed as a thin zigzag line depicted by the red arrows. Due to slight over-etching, several macrographs present the Al foil as a dark tortuous line, while the others exhibit bright lines, due to the difference in etching between the pure Al foil content and surrounding alloy material. The images show enhanced deformation of the Al foil away from its initial vertical position as eccentricity increases and as welding speed decreases. In addition, the periodic bands protruding from the advancing side (AS) can also be found to expand horizontally with increasing eccentricity.

Figure 4-5 presents inverse pole figure (IPF) maps of the inner band, outer band, and middle SZ regions in the welds produced with aligned and eccentric tools, in which the areas of interest are shown in Figure 4-5(a). The high angle grain boundaries (misorientation angle  $> 15^\circ$ ) are presented as black lines, while low angle grain boundaries (misorientation angles between  $2^\circ$

and 15°) are shown by faint grey lines in the boundary misorientation maps (Figure 4-5(b) to (g)). In all inspected regions, increased grain refinement can be noted when the eccentric tooling was utilized.

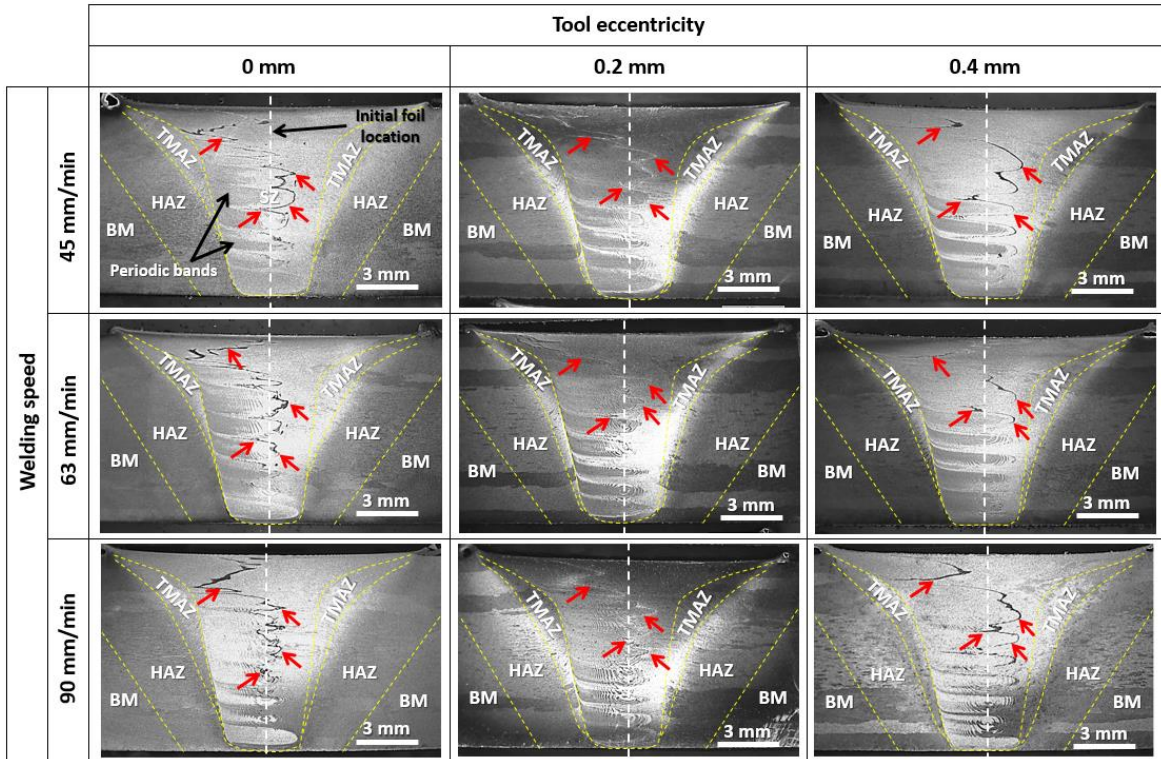


Figure 4-4. Transverse plane cross-sectional macrographs of aligned (0 mm), 0.2 mm eccentric, and 0.4 mm eccentric setup with various travel speeds. Red arrows show tracer Al foils. Advancing side is at the left side of the images, while retreating side is at the right side.

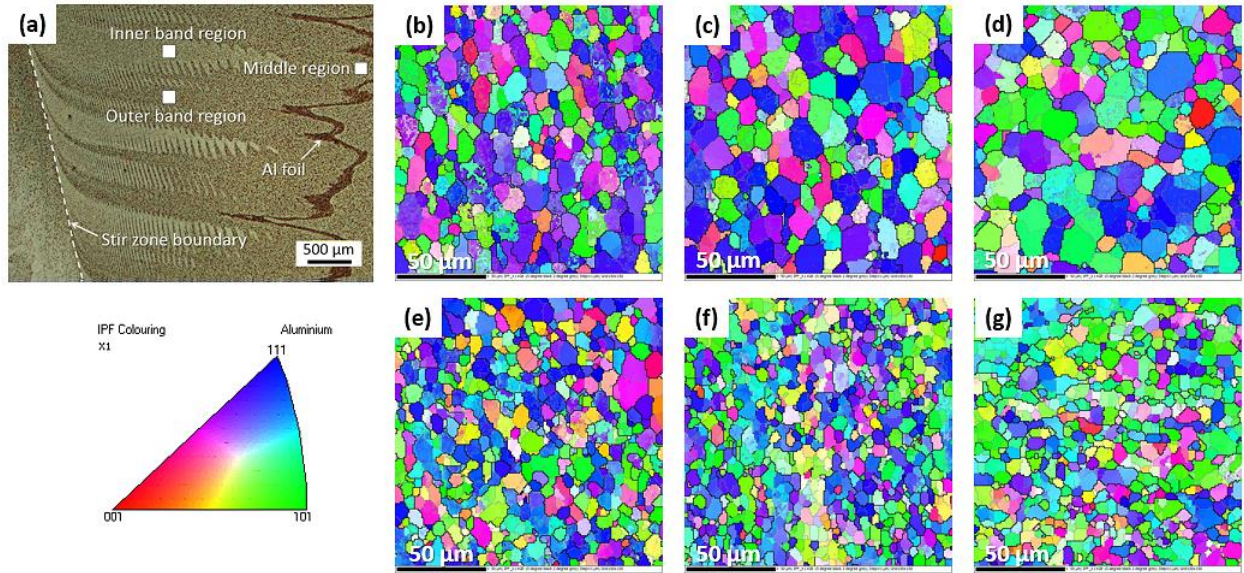


Figure 4-5. (a) Close up of the stir zone with the respective points for EBSD analysis. Grain size and orientation of aligned sample at the (b) inner band region, (c) outer band region, and (d) middle region. Grain size and orientation of 0.2 mm eccentric sample at the (e) inner band region, (f) outer band region, and (g) middle region.

Grain sizes were measured using the ASTM E112-13 linear intercept method and the average grain sizes are presented in Figure 4-6. Despite the large margin of error due to the preferred orientation of the grains, a general trend of a slight decrease in grain size can be seen for both the samples made using aligned or eccentric tools, when comparing the areas in the middle and outer band region, versus the inner band region. A slight decrease in the grain size can also be observed in all three stir zone (SZ) regions for the eccentric setup, but no apparent trend could be noted with increased eccentricity.



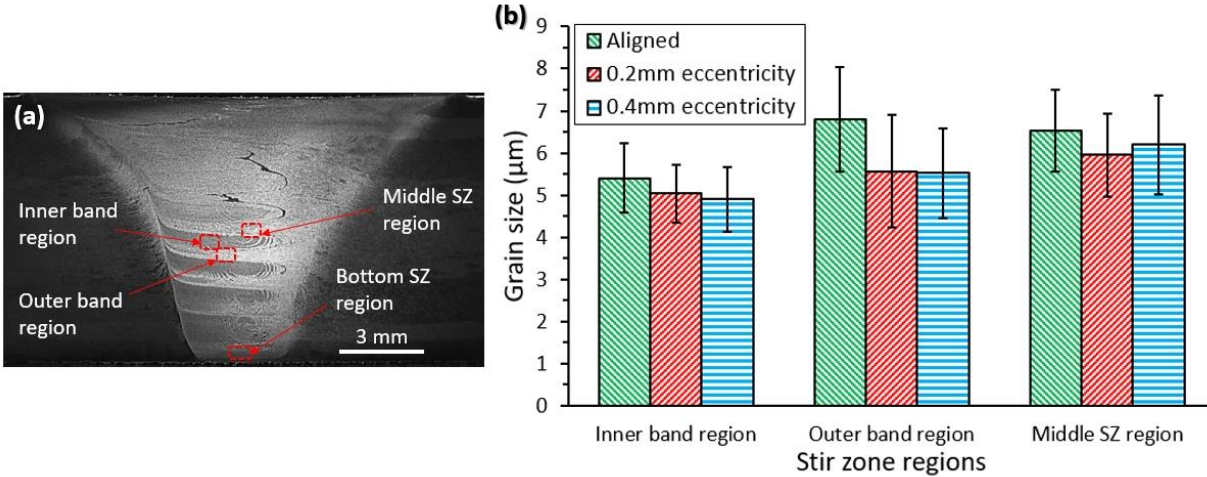


Figure 4-6. (a) Grain size measurement regions of interest (b) Grain size of various SZ regions for aligned and eccentric setups.

TEM analysis was conducted as outlined in Section 3.4. Figure 4-7 presents TEM microstructures of the middle inner band region and the bottom region of the stir zone (refer to Figure 4-6(a)) for the aligned and 0.2 mm eccentric setup. The inner band region was examined in both the mid-thickness and bottom SZ region. Needle-shaped (depicted with yellow arrow), rod-shaped (blue arrow) and platelet-shaped (red arrow) precipitates can be observed. While the mid-thickness region is mainly dominated by rod-shaped and needle-shaped precipitates for the aligned sample (Figure 4-7(a)) and 0.2 mm eccentric setup (Figure 4-7(b)), both setup conditions exhibit predominantly platelet-shaped precipitates at the bottom region (Figure 4-7(c) and (d)). This suggests that the local mid-thickness and bottom areas underwent a different thermal history, which may affect the stir zone properties.

To further examine the difference between the inner and outer band regions of the middle section, Figure 4-8 presents the TEM micrographs of the inner band region and the outer band region of both aligned and 0.2 mm eccentric samples. In both regions of the aligned sample (Figure 4-8(a) and (b)), coarse rod-shaped dispersoids (shown in green arrows) averaging  $1.31 \pm 0.62 \mu\text{m}$  were present on the grain boundaries as well as within the grains. Such large particles were also observed by Svensson et al. and Gerlich et al. in the stir zone region of AA6082 and AA6061, respectively [109], [110]. In addition, a higher density of much finer rod-shaped particles (blue arrows) are seen dispersed throughout the aligned sample's inner band region (Figure 4-8(a)) while the plate-shaped particles (red arrows) are more predominant in the outer region (Figure 4-8(b)).

The dislocation densities for both regions are also relatively low owing to the thermal cycle imposed during FSW [111].

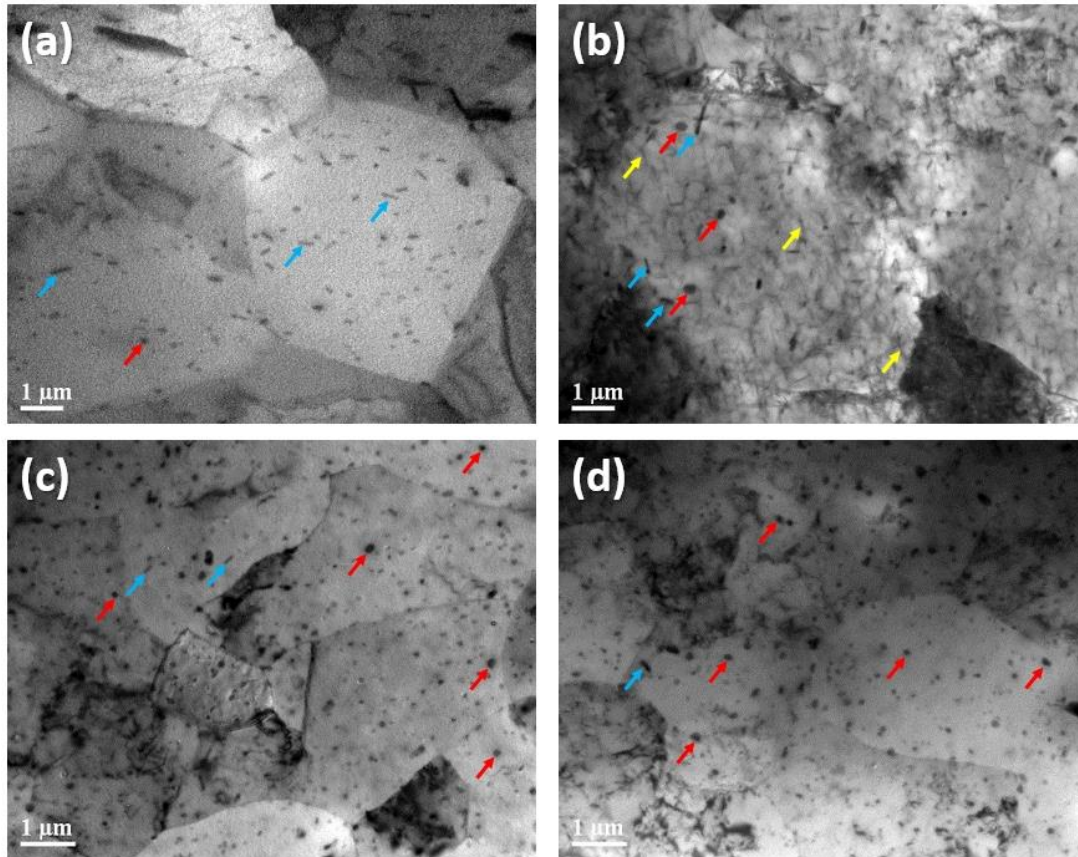


Figure 4-7. TEM microstructures of the middle region for (a) aligned sample and (b) 0.2 mm eccentric sample and the bottom inner band region for (c) aligned sample and (d) 0.2 mm eccentric sample.

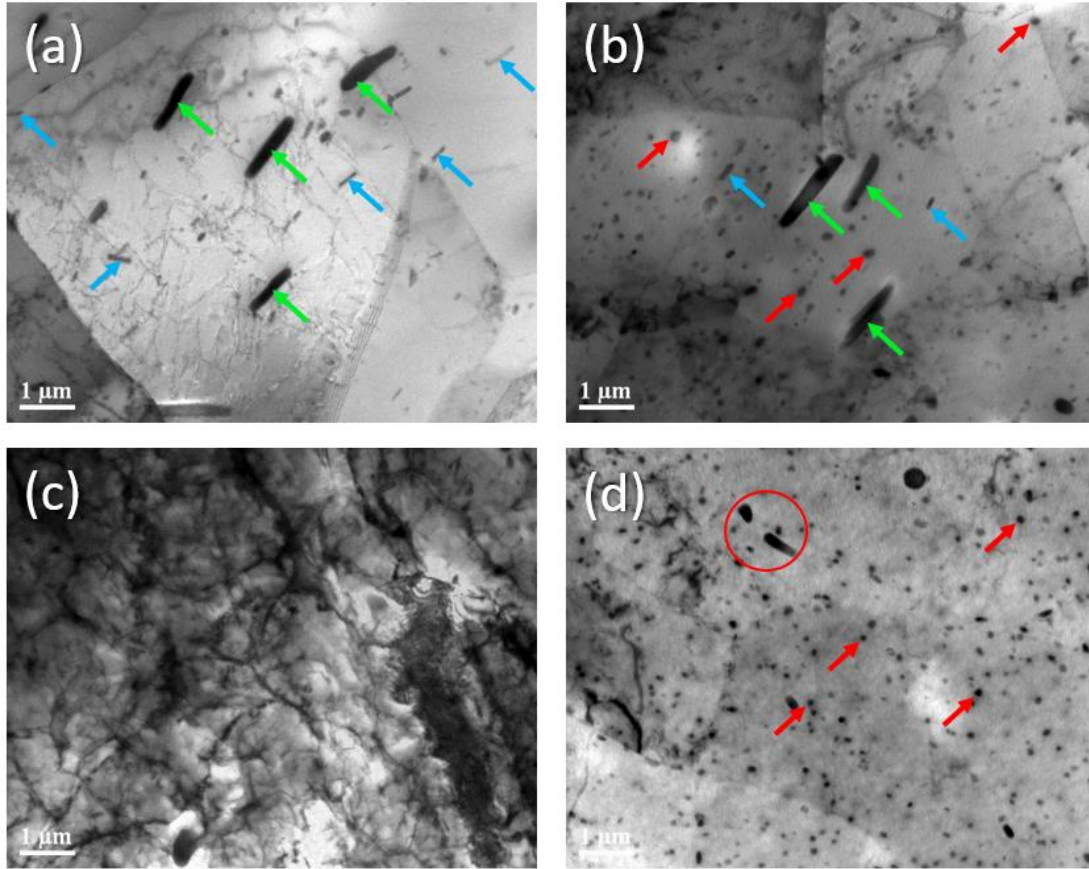


Figure 4-8. TEM micrographs of (a) inner band region and (b) outer band region of aligned sample, as well as (c) inner band region and (d) outer band region of 0.2 mm eccentric sample.

However, a stark contrast of higher dislocation density can be seen in the inner band region of the 0.2 mm eccentric sample (Figure 4-8(c)). Since previous work [112] has established that the material in the periodic bands originated from the advancing side base material and more material accumulation occurs in this region when eccentric tool setup was employed, it is postulated that the region undergoes enhanced deformation and shearing activity, amplifying the formation of dislocations.

On the other hand, the outer band region (material originating from the retreating side) shows an abundance of the plate-shaped particles, likely to be Si-rich stable  $\beta$  precipitates [113]. This is similar to the outer band region of the aligned sample, but with the absence of the coarse dispersoids. Even so, based on the different morphology from the surrounding fine particles, it is proposed that the particle highlighted in the red circle in Figure 4-8(d) is a remnant of a dispersoid, presumably being sheared due to the rigorous eccentric motion, as commonly reported following

FSW [114]. This may also account for why the dispersoids are largely absent in the 0.2 mm eccentric sample.

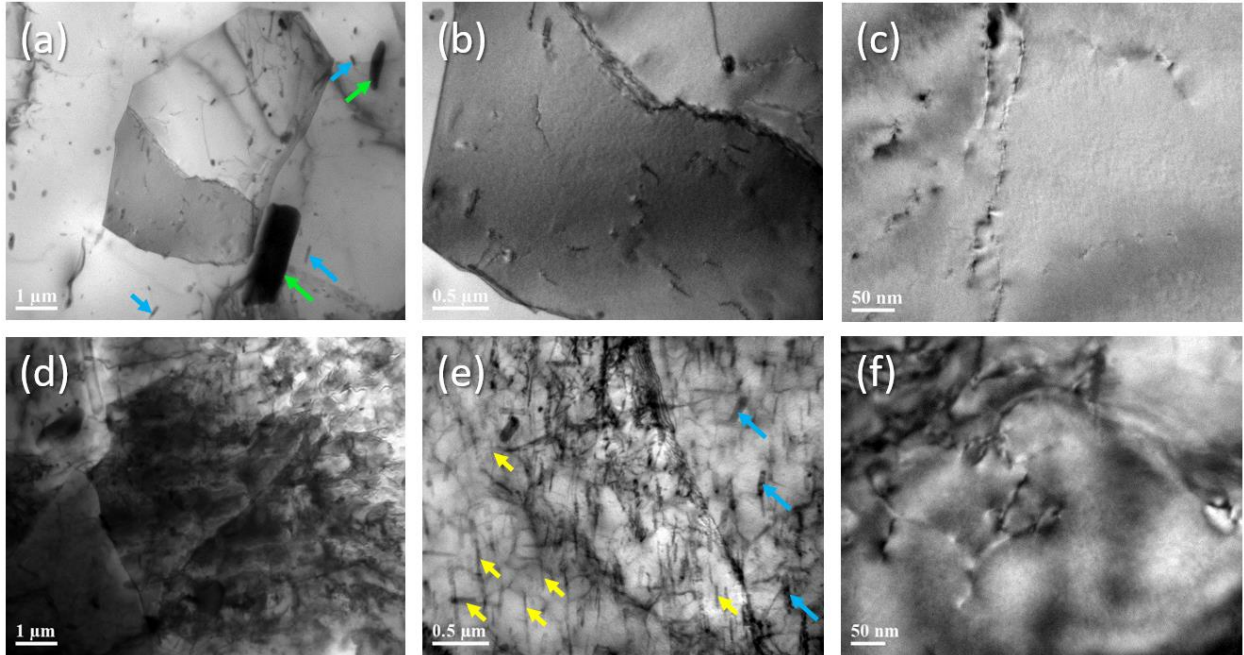


Figure 4-9. TEM micrographs of inner band region for aligned sample ((a) to (c)) and 0.2 mm eccentric sample ((d) to (f)) with increasing magnification.

Figure 4-9 presents TEM micrographs of the inner band region for aligned and 0.2 mm eccentric samples for further comparison, taken from the  $[0\ 0\ 1]_{Al}$  zone axis. The difference in dislocation density can be clearly seen, where the 0.2 mm eccentric sample demonstrates significantly higher dislocation density. While only coarse dispersoids (green arrows) and rod-shaped particles (blue arrows) are present in the aligned sample, higher magnification of the 0.2 mm eccentric samples reveals that, in addition to the rod-shaped particles, finer needle-shaped  $\beta''$  precipitates (yellow arrows) are also present, as observed earlier in Figure 4-7(b).

Table 4-1 summarizes the observed dominant precipitates, dispersoids, and dislocation density of the inner and outer band region for both samples. The possible particle compounds were suggested based on the energy dispersive X-ray spectroscopy (EDS) peaks observed in the TEM analysis data (not shown). The diameter or length of precipitates and dispersoids listed in the table are an average of 30 measured particles from several observed locations.

Table 4-1. Dominant precipitate and dislocation density of inner and outer band region of samples.

	Dominant precipitate (average diameter/length in nm)	Dispersoids (average length in nm)	Dislocation density
Aligned sample			
Inner band region	-	Large, rod-shaped $\text{Al}_{12}(\text{Fe}, \text{Cr}, \text{Mn})_3\text{Si}$ $1308 \pm 619$	Low
		Small, rod-shaped $\text{Al}_{12}(\text{Fe}, \text{Cr}, \text{Mn})_3\text{Si}$ $292 \pm 53$	
Outer band region	Plate-shaped $\beta$ (Si) $137 \pm 44$	Large, rod-shaped $\text{Al}_{12}(\text{Fe}, \text{Cr}, \text{Mn})_3\text{Si}$ $1643 \pm 755$	Low
Eccentric sample			
Inner band region	Needle-shaped $\beta''$ and $\beta'$ ( $\text{Mg}_2\text{Si}$ ) $233 \pm 28$	Small, rod-shaped $\text{Al}_{12}(\text{Fe}, \text{Cr}, \text{Mn})_3\text{Si}$ $289 \pm 75$	High
Outer band region	Plate-shaped $\beta$ (Si) $115 \pm 45$	-	Medium

### 4.3.3 Mechanical characterization

Vickers hardness measurements were taken at least 10 days after the welding process in order to ensure that the precipitates have reached a stable condition considering room temperature aging may occur. It has been shown by Aval et al.[115] that the stir zone hardness profile of AA6061-T6 alloy stabilizes after 168 hours (7 days), and does not undergo any significant change even after 1680 hours (70 days). The hardness mapping of the SZ is presented in Figure 4-10 for all tool alignment conditions with welding speed of 63 mm/min. Each hardness indent is 0.5 mm apart from each other.

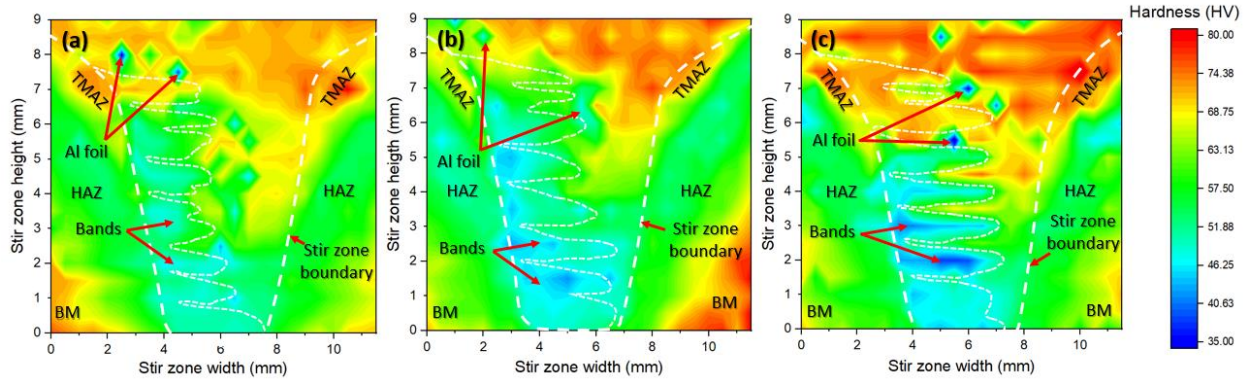


Figure 4-10. Stir zone hardness mapping of (a) aligned setup, (b) 0.2 mm eccentric setup, and (c) 0.4 mm eccentricity setup. The welding speed is 63 mm/min.

Several soft spots can be seen throughout the SZ, where the hardness indents occur at locations where Al foil is present, and therefore exhibit values well below the workpiece hardness. Overall, the SZ and HAZ of the heat-treatable AA6061 alloy undergoes softening compared to the nominal base metal hardness value of 108 HV due to the heat introduced during the FSW process. The HAZ and the lower region of the SZ show more severe softening in both setups. In addition, the soft SZ region is expanded horizontally with higher tool eccentricity. This is observed concurrently with a horizontal expansion of the periodic bands shown in Figure 4-4 as eccentricity is imposed.

In a preliminary study, tensile testing was performed to identify the effects of tool eccentricity on mechanical behaviour as per the standard ASTM E8M-04 using dog bone-shaped coupons, which indicated that the enhanced softening due to eccentric motion does not compromise the tensile strength [65]. However, DIC analysis as discussed in Section 3.5 was additionally conducted to further understand the fracture evolution of the joints through observations of its local strains. Figure 4-11 shows the strain maps during transverse tensile testing of a joint produced with aligned tooling (Figure 4-11(a) and (c)) compared to a joint produced with 0.2 mm eccentricity (Figure 4-11(b) and (d)), both with intentionally induced kissing bond defects. The map is showing strains in the weld transverse direction where loading was applied ( $\epsilon_{yy}$ ). In both cases, the DIC images indicate that initial local strain initiated at the weld root where the intentional kissing bond defects exist (Figure 4-11(a) and (b)). However, two modes of fracture were observed, namely fracture through the HAZ (Figure 4-11(c)) and fracture through the SZ

(Figure 4-11(d)). It should be noted that all aligned samples tested failed at the HAZ, while two out of the six 0.2 mm eccentric samples tested failed in the SZ.

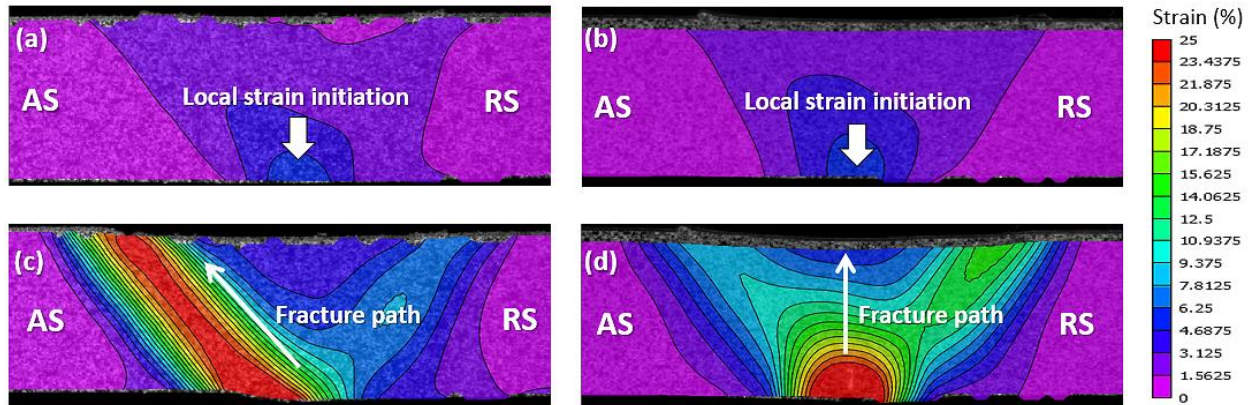


Figure 4-11. Cross-sectional DIC images of initial local strain of (a) aligned sample and (b) 0.2 mm eccentric sample as well as final local strain right before fracture for (c) aligned sample and (d) 0.2 mm eccentric sample. Both samples contain kissing bond defect at the weld root.

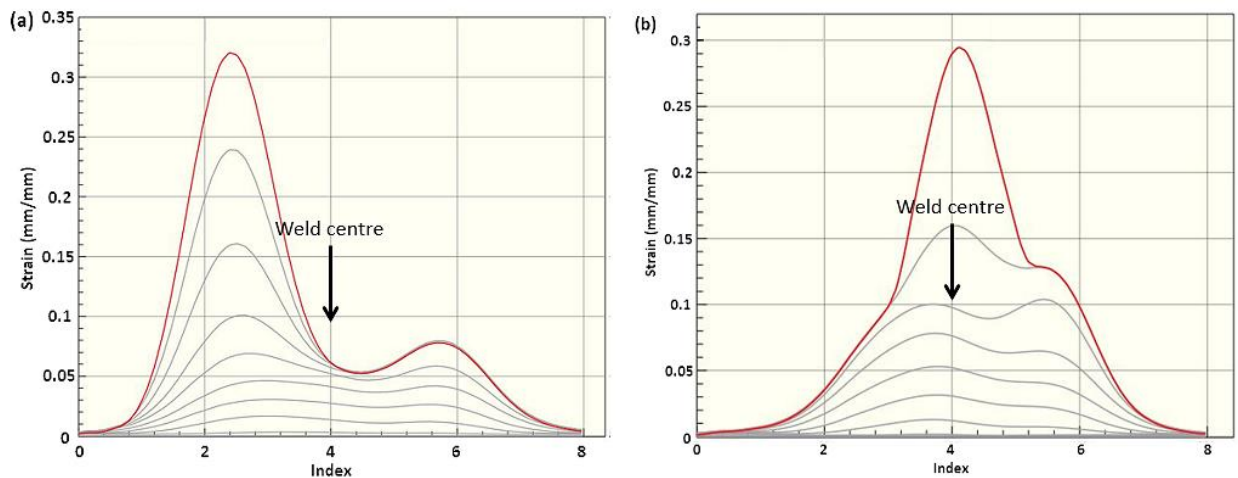


Figure 4-12. Comparison of strain distribution versus location index across the mid-region traverse plane for (a) samples fractured in the HAZ and (b) samples fractured in SZ.

A representation of the change in the local strains at the mid-thickness of aligned and 0.2 mm eccentric sample is presented in Figure 4-12. The data suggests that elongation initially occurs throughout the SZ and HAZ in both cases to a certain extent, but eventually the strains concentrated in the HAZ and fracture occurs here at 32% strain in the case of aligned setup. On the other hand, the strains in some of the 0.2 mm eccentric setup continues to concentrate in the proximity of the weld centre, eventually failing at 29% strain in this region.

## 4.4 Discussion

### 4.4.1 Effects of pin profile on stir zone microstructure

As can be seen in Figure 4-4, a clear SZ boundary delineation in the AS for all tool setup can be explained through the different strain experienced on each side. Reynolds demonstrated through mathematical modelling that the AS undergoes higher strains compared to the RS [116]. Other previous works have also observed severe shearing in the AS when the SZ is viewed from the horizontal plane compared to the RS [98]. This is an inherent feature in FSW, since the workpiece material from the front of the tool is initially accumulated from the AS, eventually being deposited at the wake of the tool [61], [103].

On the other hand, the periodic bands protruding from the AS of the SZ can be explained through the Nunes kinematic model [98], [117]. The model suggests that a combination of three incompressible flow fields, namely rigid body rotation, uniform translation, and ring vortex forms two distinct currents, specifically a straight-through current on the RS and a whirlpool current on the AS. In the straight-through current flow, the material is simply deposited from the front to the wake of the tool. Meanwhile, the material in the whirlpool current undergoes downward displacement by the thread profile on the rotating tool, experiencing several rotations before being deposited at a relatively lower position. The interaction between the two currents results in the interleaving feature, where the periodic bands are formed through the whirlpool current (AS material), while the dominant region in the SZ is the result of the straight-through current (RS material). Hamilton et al., among others, have also reported this feature in their work [118].

Nunes has also suggested that the multiple bands observed in the present work can be associated to the tool pin threads that generates multiple ring vortex throughout the through-thickness of the workpiece [98]. This can be demonstrated from an overlaid image of the tool pin on the SZ of a sample, depicted in Figure 4-13. The periodic bands (highlighted in red) are seen to conform well to the troughs of the pin threads, while the locations of the flats on the tool pin profile facilitates an orderly through-thickness deposition of whirlpool current materials at the wake of the tool. This is in contrast with the stir zone of thin samples, where a singular onion-ring shaped stir zone is commonly formed.



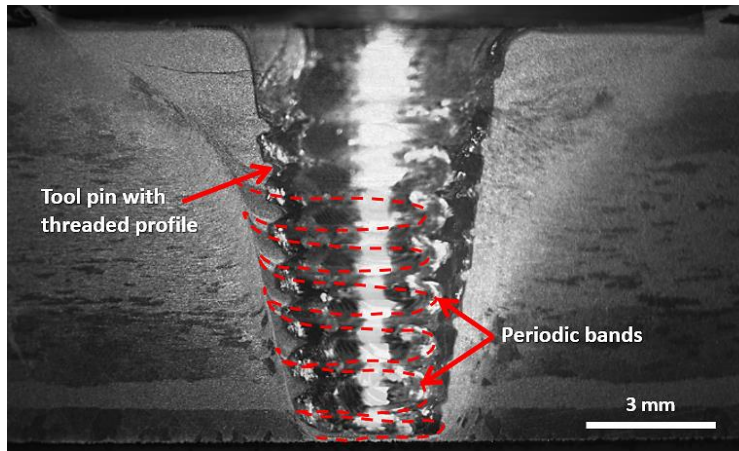


Figure 4-13. Overlaid image of tool pin on the stir zone of a sample.

#### 4.4.2 Effects of tool eccentricity on stir zone microstructural morphology

As mentioned earlier, the larger periodic bands generally seen at the lower SZ region of cross-sectional images in Figure 4-4 are believed to be due to the downward deposition mechanism. However, observations of horizontal expansion of these bands in the eccentric setups may also suggest that more AS material is accumulated in the whirlpool current and deposited evenly at each pin thread. Formation of onion-ring shaped features near the centre and lower region of the stir zones in Figure 4-4 further emphasizes that mixing between materials within the whirlpool current and straight-through current is enhanced. This observation will be analyzed further based on kinematics in the subsequent subsection.

In addition, Figure 4-10 demonstrates that the inner band region (formed by the whirlpool current), which is expanded due to eccentricity, shows lower hardness compared to its outer band region (formed by straight-through current) counterpart. The softening effect in the SZ of the age hardened aluminum alloys such as AA6061 are governed by strengthening precipitates [119], [120]. The primary hardening constituent in AA6061 is magnesium silicide,  $Mg_2Si$ . The precipitation sequence of AA6061 is as follows [121], [122]:

Supersaturated solid solution  $\rightarrow \beta''$  (needle-shaped precipitate, metastable)  $\rightarrow \beta'$  (rod-shaped precipitate, metastable)  $\rightarrow \beta$ - $Mg_2Si$  (platelet-shaped, stable).

The needle-shaped precipitates have been known to be the main strengthening factor in 6xxx series Al alloys [123]. Previous studies by Sato et al. and Woo et al. have also demonstrated

that such alloys exhibit lower hardness values in the stir zone due to dissolution of these coherent  $\beta''$  phases [124], [125]. A clear contrast between the dominant precipitates at the middle inner band region and bottom region shown in Figure 4-7 suggests that overaging occurred in the bottom region, which forms a high density of large and incoherent  $\beta$ -Mg<sub>2</sub>Si precipitates, subsequently decreasing the hardness in this region.

However, the periodic bands protruding from the advancing side stir zone boundary also exhibits low hardness values in the stir zone, while eccentric setup further expands this 'soft zone'. This is despite the high dislocation densities observed in the 0.2 mm eccentric setup inner band region images (Figure 4-8(c) and Figure 4-9(d) to (f)), which seem to show minimal effect in increasing the local hardness of the stir zone, contrary to conventional wisdom.

While it is postulated that more heat is generated in the periodic bands of 0.2 mm eccentricity setup and possibly higher static/dynamic recovery is expected, as will be seen in Section 6.3.4, evidence of higher strains and strain rates may account for a high dislocation density retained in the eccentric sample. Results in Section 6.3.4 seem to suggest that the high dislocation density in the 0.2 mm eccentric setup is maintained, since it is less influenced by static/dynamic recovery mechanism and is more dominated by the high strain and strain rate.

In addition, owing to the enhanced shearing in the eccentric setup, it is postulated that the fine grains and high dislocation density present mainly in the inner band region of this sample may have acted as a catalyst for precipitation growth. Works by Andersen showed that the dimension of the semi-coherent strengthening  $\beta''$  precipitates is typically about 50 nm in length [126]. These precipitates acts as shearable obstacles against dislocation movement [127]. However, if coarsening occurs, the precipitates become non-shearable and the dislocations by-pass the particles instead, decreasing the retarding effect against dislocation movements [128], [129]. Based on the average value in Table 4-1 ( $233 \pm 28$  nm), it seems to suggest that the needle-shaped  $\beta''$  precipitates underwent coarsening, making them less useful in strengthening the material. It is also likely that a portion of these precipitates has already transformed into  $\beta'$  precipitates, since the size and structure of both are comparable and can be easily mistaken [113], [130]. Thus, formation of these overaged, large needle-shaped precipitates from the dislocation-precipitate interactions may have effectively negate the strengthening effect of the high dislocation densities, resulting in a comparable 'soft zone' with the aligned sample [128].

### 4.4.3 Kinematics of tool eccentricity and material deposition mechanism

As discussed earlier, it is suggested that the eccentric movement accumulates and deposits more AS material through the whirlpool current. This can be explained through the kinematics of tool eccentricity.

The kinematic analysis can be divided into tool tangential velocity,  $v_t$ , and tool linear velocity,  $v_l$ . For tangential velocity of an aligned tool,  $v_{ta}$ :

$$v_{ta} = r_p \cdot \omega = 352 \text{ mms}^{-1} \quad (\text{Eq. 4-1})$$

where  $r_p$  is the root pin radius (3 mm) and  $\omega$  is the rotational speed in  $\text{rads}^{-1}$  (117.3  $\text{rads}^{-1}$ ). When the 0.1 mm and 0.2 mm tool offset is considered for the 0.2 mm and 0.4 mm eccentric setup, the tangential velocity for both setups become  $364 \text{ mms}^{-1}$  and  $375 \text{ mms}^{-1}$ , respectively. It can be seen that  $v_t$  of samples show an incremental linear increase as larger tool offset is employed.

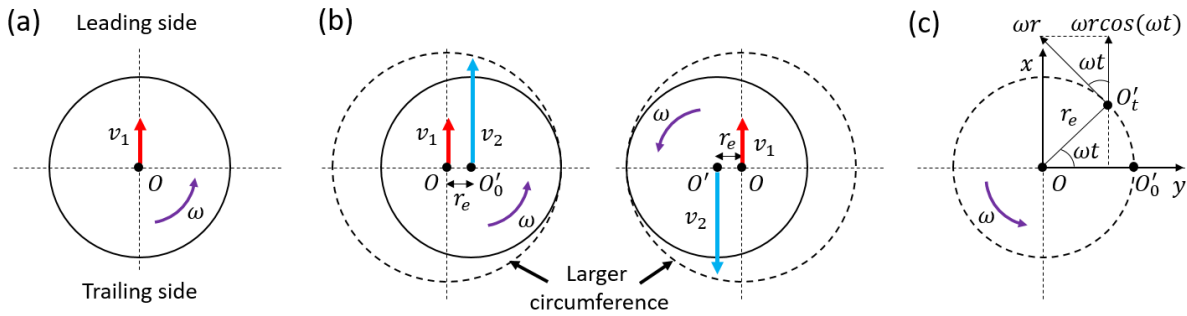


Figure 4-14. Linear velocity of tool in (a) aligned and (b) eccentric setup during rotation. (c) Schematic relationship between the angular velocity, eccentricity and tool velocity components in welding direction [58]. Welding direction is upwards.

However, the linear/translational velocity at the tool centre,  $O$ , with respect to the welding direction changes drastically when the tool eccentric setup is compared. This can be illustrated using Figure 4-14 [58]. In the case of an aligned setup (Figure 4-14(a)),

$$v_{la} = v_1 = 63 \text{ mm} \cdot \text{min}^{-1} = 1.05 \text{ mm} \cdot \text{s}^{-1} \quad (\text{Eq.4-2})$$

where  $v_1$  is the weld speed. On the other hand, with the tool offsetting radius,  $r_e$ , as shown in Figure 4-14(b), the eccentric tool linear velocity  $v_{le}$  is the sum of  $v_1$  and  $v_2$ , where  $v_2$  is the velocity component at tool centre  $O'$  along the welding direction due to the eccentric rotation. For

each revolution,  $v_2$  undergoes a positive (forward) motion in the advancing side and a negative (backward) motion in the retreating side.

As shown in Figure 4-14(c),  $v_2$  can be expressed as

$$v_2 = \omega \cdot r_e \cdot \cos(\alpha) \cdot \cos(\omega t) \quad (\text{Eq.4-3})$$

where  $\alpha$  is the tool tilt angle ( $2.5^\circ$ ). Since  $\cos(\alpha) \approx 1$ ,

$$v_{le} = v_1 + v_2 = v_1 + \omega \cdot r_e \cdot \cos(\omega t) \quad (\text{Eq.4-4})$$

Based on Equation 4-2 and Equation 4-4,  $v_{la}$  and  $v_{le}$  can be plotted as a function of time (Figure 4-15(a)). While the linear velocity of aligned tool setup remains constant at 1.05 mm/s, drastic fluctuations of  $v_{le}$  can be observed as tool eccentricity increases. At 0.4 mm eccentricity, the maximum and minimum linear velocity is calculated to be 24.5 mm/s and -22.4 mm/s, respectively. The significant change in amplitude is presented in Figure 4-15(b). Thus it can be inferred that, despite the consistent APR forward motion, tools with eccentricity exhibit variations in the linear velocity where the tool is seen to translate forward in the AS while moving backwards in the RS.

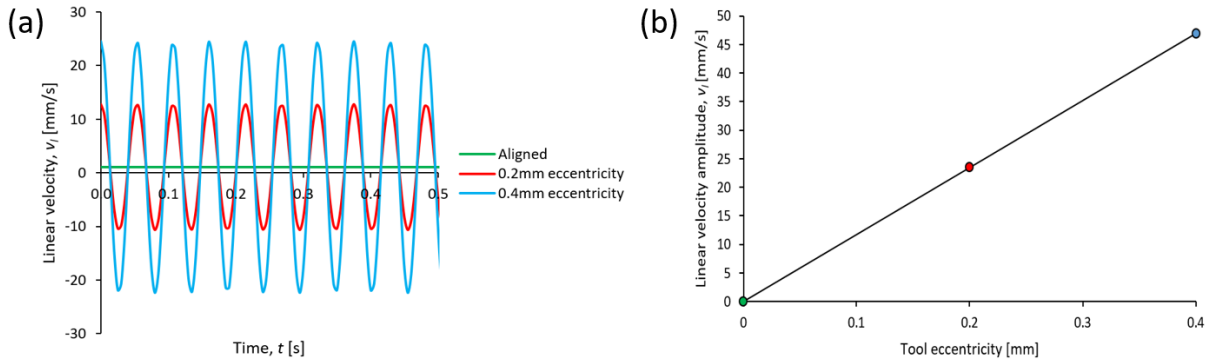


Figure 4-15. (a) Time dependent linear velocity of aligned and eccentric setup tool and (b) Linear velocity amplitude change due to tool eccentricity.

This welding speed variation due to eccentricity has also been reported by Yan et al. using a high resolution linear variable displacement transducer (LVDT) [60]. With a measured eccentricity of 0.03 mm, the authors showed that it corresponds to a variation in actual welding speed of  $\pm 1$  mm/s at 300 rpm rotational speed. Even at higher welding speeds, it seems that this trend would be present. This is because the APR and  $v_1$  will remain low since a relatively high rotational speed is needed to maintain sufficient heat to soften the material.

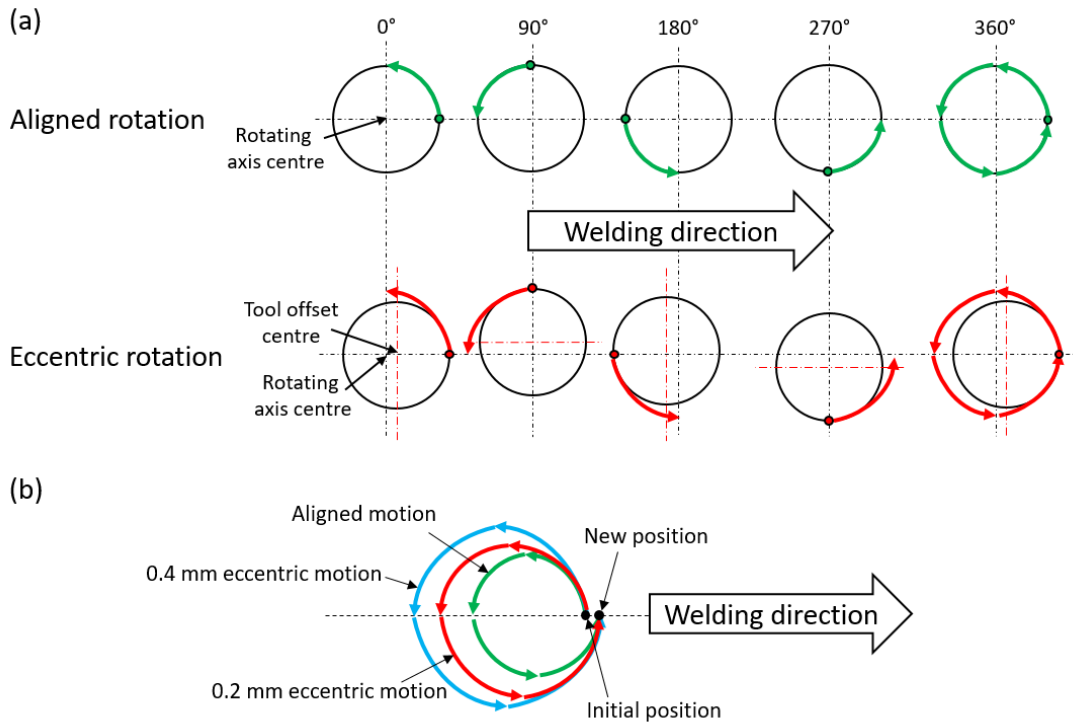


Figure 4-16. (a) Comparison of point travel path per rotation of tool for aligned and eccentric setup with no translational motion. (b) Schematic of APR point displacement comparison for aligned, 0.2 mm, and 0.4 mm eccentric setup.

Another kinematic consideration is with regards to pin surface point travel path per revolution, as suggested by Essa et al.[101] and illustrated in Figure 4-16. Consider both cases of aligned and eccentric setup where a point on the tool surface initiates rotational movement from the tip of the leading (forward) side, but with no translational motion (Figure 4-16(a)). For simplicity, the tool pin is considered to be round. Note that, since the eccentricity setup has a tool offset centre, the point is displaced forward slightly due to the offset. With each 90° rotation, the travel path for both conditions can be traced, until a full rotation is made. Combining the travel paths of the point at the full rotation (360°), it can be seen that, while the aligned setup makes a travel path equivalent to the circumference of the tool (green arrows), the eccentric setup forms a larger travel path because of the tool offset (red arrows). The travel path also linearly increases as the tool eccentricity increases. With the addition of translational motion, the point travel path can be schematically presented as shown in Figure 4-16(b), where a backward sense of tool travel can also be seen with each rotation.

From this kinematic analysis, several deductions regarding the effect of eccentricity can be inferred;

- (i) Eccentric setup enhances AS material accumulation since a larger travel path as well as higher linear and tangential velocity is formed, despite the consistent APR measured. This explains horizontal expansion of the periodic bands due to increased eccentricity observed in Figure 4-4.
- (ii) From the discontinuous welding process due to eccentric motion proposed by Gratecap et al.[75] and the backward sense of eccentric tool motion mentioned earlier, it can be postulated that a periodic material compression takes place during material deposition after a gap opens during half of the eccentric cycle (at  $0^\circ$  in Figure 4-16(a)) and closes again in the other half cycle (at  $180^\circ$  in Figure 4-16(a)). It can also be seen that more material is deposited with each revolution, manifested by the excess material on the weld surface in Figure 4-2. Another reason for the obvious roughness in eccentric samples is due to the slight vertical oscillation caused by the tool tilt, which enhances the amplitude between the crest and troughs of the weld bands [57], [58].
- (iii) With enhanced material shearing due to the periodic material compression, a longer travel path and accumulation of AS material occurs in the whirlpool current in each rotation, and so finer grains are formed at the wake of the tool as seen in Figure 4-5. Corresponding to the enhanced shearing activity, the local peak temperature of the whirlpool current material is expected to rise, promoting dissolutions of strengthening precipitates and re-precipitation of soft  $\beta$  phases, consequently degrading the material hardness. While finer grains are observed in eccentric setups, which suggests increased shearing activity, further study is needed to confirm this issue by comparing the strain rates of each setup. In addition, the force and torque implied on the pin is expected to increase with increasing eccentricity, potentially decreasing the tool life and durability.

It is to be expected that the actual amplitude of 0.2 mm and 0.4 mm eccentricity setup may be dampened to less than its initial values during welding because of the constraint imposed by the material surrounding the tool, and finite machine rigidity. Observation of the changes in eccentricity is discussed in detail in Chapter 6.

#### **4.4.4 Tool eccentricity and kissing bond defect**

Defects such as kissing bond defects are undesirable and may pose detrimental effects on the joint's integrity. However, such defects and their severity are difficult to detect through common non-destructive tests (NDTs) [131], [132]. In addition, prior work by the authors on the fatigue life of thick section FSW joints in AA6061 has suggested that specimens with kissing bond defects have the lowest fatigue performance compared to any other defect groups [133]. Due to these challenges, it is therefore of interest to explore whether the tool eccentricity setup would have a positive or negative influence on the effort to limit the detrimental impact of samples where unintentional kissing bonds may be present.

As stated earlier, previous works by the authors have suggested that the enhanced softening in the SZ owing to eccentric setup does not have any effect on the tensile strength behaviour of AA6061 [65]. This can be attributed to the observed fracture propagating in the HAZ, which is away from the softened SZ region in all tested samples. However, evidence from the results presented herein (Figure 4-11 and Figure 4-12) seems to suggest that tool eccentricity may facilitate a different failure path in friction stir welds with existing kissing bond defects.

Owing to the constant vertical oscillation of the tool and slight difference in plunge depth for each workpiece, the vertical kissing bond length was measured to vary between 192 to 252  $\mu\text{m}$ . Figure 4-17 shows an aligned sample, which fractured at the HAZ, and a 0.2 mm eccentric setup sample, which fractured in the SZ. Interestingly, an initial fracture originating from the kissing bond defect can be observed even in the aligned setup, despite the final fracture happening in the HAZ. This was observed in all samples that fractured in the HAZ, including the samples with 0.2 mm tool eccentricity. Since local strain initiated at this region (Figure 4-11(a) and (b)), the slightly higher hardness of the aligned setup at lower region of the SZ (Figure 4-10(a)) may have prevented further crack propagation in the SZ until the HAZ began to yield instead.

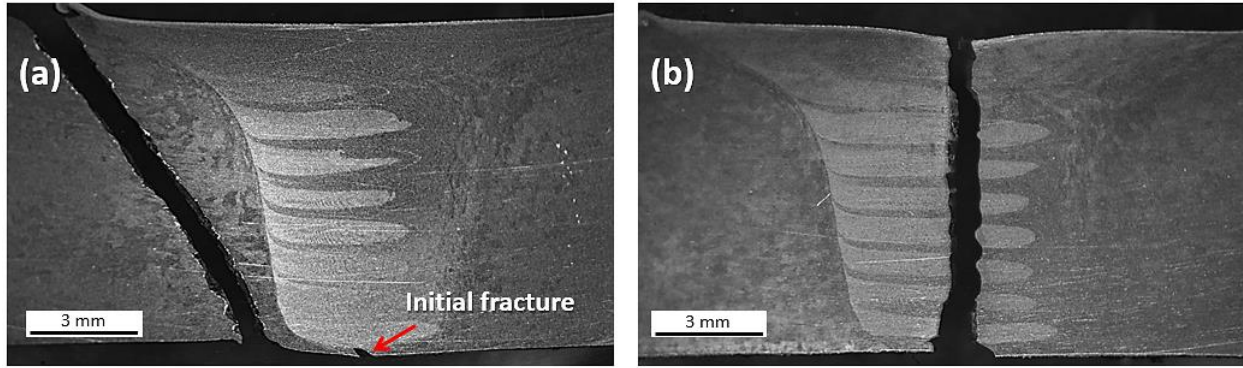


Figure 4-17. Fracture initiating at the kissing bond in both (a) aligned sample and (b) 0.2 mm eccentric sample.

On the other hand, the softening of the SZ lower region in the 0.2 mm eccentric setup (Figure 4-10(b)) could have potentially weakened this region and facilitated the crack propagation in the SZ after the initiation at the weld root. However, as mentioned earlier, only two out of the six tested eccentric samples show this trend, which is insufficient to confirm the extent to which the kissing bond length and shape, which are inconsistent even within a single FSW, play a role in the final fracture path.

## 4.5 Conclusion

The effect of tool eccentricity on AA6061-T651 aluminum alloy friction stir welded thick plate is evaluated in this chapter. The key findings are summarized as follows:

- Higher surface roughness average and roughness depth of the weld bead was observed with increasing eccentricity.
- Al foil inserts indicate enhanced material flow and mixing in the stir zone with increasing tool eccentricity and decreasing welding speed.
- Finer grain size is generally observed in the inner band region compared to outer band and middle SZ regions and is further refined when an eccentric setup is utilized.
- TEM analysis reveals high density of platelet-shaped precipitates in the bottom region of both aligned and 0.2 mm setups, which can be associated to the decrease in the hardness of this region. High dislocation density in the inner band region of 0.2 mm eccentric sample was also observed, but this had a negligible influence on the local hardness.



- Further softening of the stir zone lower and middle region due to eccentricity may promote a different failure path, which propagates through the SZ, as opposed to the typical HAZ fracture when a kissing bond defect of 0.2 mm depth is also present.

## **Chapter 5: Effects of tool eccentricity on dissimilar AA5052-AA6061 friction stir welds**

This chapter investigates the effect of tool eccentricity on the metallurgical and mechanical properties of dissimilar AA5052-AA6061 friction stir welds. The majority of this chapter is adapted from the published manuscript: ‘Dissimilar friction stir welding of thick plate AA5052-AA6061 aluminum alloys: effects of material positioning and tool eccentricity’, Luqman Hakim Ahmad Shah, Seyedhossein Sonbolestan, Abdelbaset R. H. Midawi, Scott Walbridge, Adrian Gerlich, *International Journal of Advance Manufacturing Processes* 2019, 105(1-4), 889-904.

### **5.1 Introduction**

The first objective emphasized on observing the effect of tool eccentricity on similar AA6061 alloy friction stir welds. This chapter further investigates this matter with regards to welding of AA5052-AA6061 dissimilar joints. One of the reasons for this approach is to prove the hypothesis regarding how tool eccentricity enhances material flow discussed at length in Chapter 4. In addition, it is worthwhile to investigate whether enhanced intermixing and mechanical interlocking between these dissimilar alloys may yield better mechanical properties, which would be of practical interest. Hence, in this chapter, the ‘performance’ aspect of materials engineering is also emphasized in addition to the ‘structure’ and ‘properties’ aspects.

As discussed in Chapter 4, marker studies have been an effective and simple approach to observe material flow in FSW [134]–[140]. Another reliable material flow observation method reported in the literature is by using similar metal, but with different alloying elements to give etching contrast, which could facilitate observations of material flow. Liu et al.[141] demonstrated the dynamics of rotational flow in FSW of Al alloys by using AA1050 and AA6061 sheets. Other dissimilar aluminum FSW works include joining between AA2xxx to AA5xxx [142], AA2xxx to AA6xxx [94], [143]–[147], AA6xxx to AA7xxx [148]–[152] and AA2xxx to AA7xxx alloys [153], [154], [163], [155]–[162].

Even so, arguably the most investigated dissimilar FSW aluminum alloy combination is between non-heat treatable AA5xxx and heat treatable AA6xxx [40,47–64]. Findings include insights on microstructural texture, thermal history, fracture behaviour, strength, and hardness. However, as mentioned earlier, most published research focuses on specimens with  $\leq 6$  mm

thickness and is not relevant to thick plate samples where the material flow and thermal history is expected to be vastly different.

The objective of this study is to investigate thick plate dissimilar FSW joints between AA5052 and AA6061 aluminum alloy plates. These materials were chosen to enable observation of the effects of tool eccentricity and base metal positioning on the stir zone material flow and thermal history of heat treatable AA6061 and non-heat treatable AA5052 alloy. While several of these past works have emphasized the importance of base metal positioning, the role of tool eccentricity as a considerable parameter on dissimilar welds has yet to be explored. In addition, as a continuation to Chapter 4, it is useful to better understanding how tool eccentricity influences dissimilar aluminum alloy friction stir welds. In this case, the differences between how the two alloys respond to etching can reveal features about the flow of material around the tool.

## 5.2 Methodology

Most of the experimental methods are described in Chapter 3. The chemical composition of AA5052 and AA6061 is presented in Appendix A. A total of eight experimental sets were designed for this study as shown in Table 5-1. The designations in the table will be referred to throughout the subsequent discussions.

Table 5-1. Experimental design for 5052-6061 dissimilar friction stir welding.

No.	Advancing side (AS)	Retreating side (RS)	Eccentricity (mm)	Designation
1	6061	6061	0	A6R6
2	5052	5052	0	A5R5
3	5052	6061	0	A5R6
4	5052	6061	0.2	A5R6-0.2
5	5052	6061	0.4	A5R6-0.4
6	6061	5052	0	A6R5
7	6061	5052	0.2	A6R5-0.2
8	6061	5052	0.4	A6R5-0.4

## 5.3 Results

### 5.3.1 Microstructural characterization

The macrograph showing the cross-section in Figure 5-1 depicts the transverse plane macrographs of dissimilar welded samples. Sharp SZ boundaries can be observed on the AS for all samples, while the boundary is not clear on the RS. Several bands can be seen protruding horizontally from the AS of the SZ throughout the thickness of specimens, which are imposed by the threaded features of the tool pin. These bands represent the distinct SZ interface between the alloys.

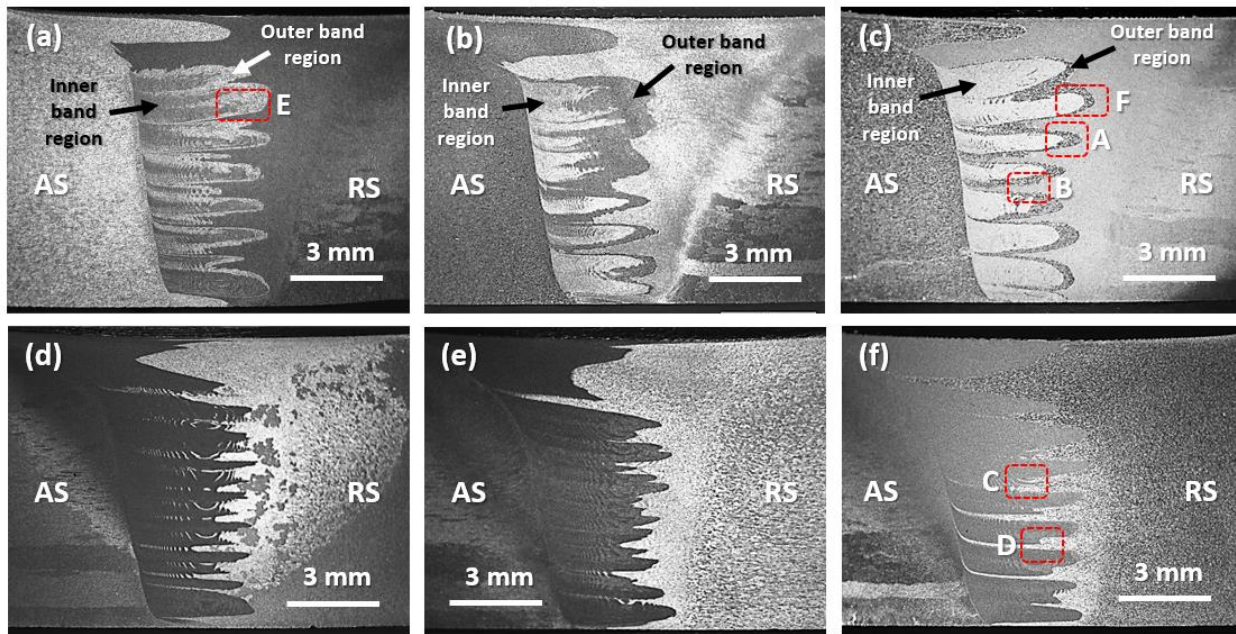


Figure 5-1. Cross-sectional macrographs of (a) A5R6, (b) A5R6-0.2, (c) A5R6-0.4, (d) A6R5, (e) A6R5-0.2, and (f) A6R5-0.4. Colour contrasts are visible between work pieces due to difference in lighting setup and slight variation in the etching period.

The measured area of the bands are summarized in Table 5-2. Widening of these bands can be observed as increasing eccentric motion is imposed. In addition, it can be observed that the A5R6 samples (Figure 5-1. Cross-sectional macrographs of(a) to (c)) formed distinct regions with colour contrast within the bands. The inner region of this band is seen to slightly decrease and increase significantly when 0.2 mm and 0.4 mm eccentricity is imposed, respectively (Table 5-2). Even so, very minimal mixing between both alloys can be seen throughout the SZ for these

specimens. On the other hand, multiple vortex-like features can be seen in the middle of A6R5 sample (Figure 5-1. Cross-sectional macrographs of(d)), more commonly known as ‘onion rings’. Onion rings are a clear indication of good material mixing [180]. Due to the clear contrast between AA6061 (dark region) and AA5052 (bright region), it seems to suggest that efficient intermixing was achieved between the alloys.

Table 5-2. Overall and inner band and area measurements.

Specimen	Overall band area (mm <sup>2</sup> )	Inner band region area (mm <sup>2</sup> )
A5R6	28.93 ± 0.34	14.10 ± 0.18
A5R6-0.2	30.50 ± 0.06	12.01 ± 0.06
A5R6-0.4	30.92 ± 0.35	17.78 ± 0.38
A6R5	32.60 ± 0.35	-
A6R5-0.2	33.01 ± 0.41	-
A6R5-0.4	34.27 ± 0.15	-

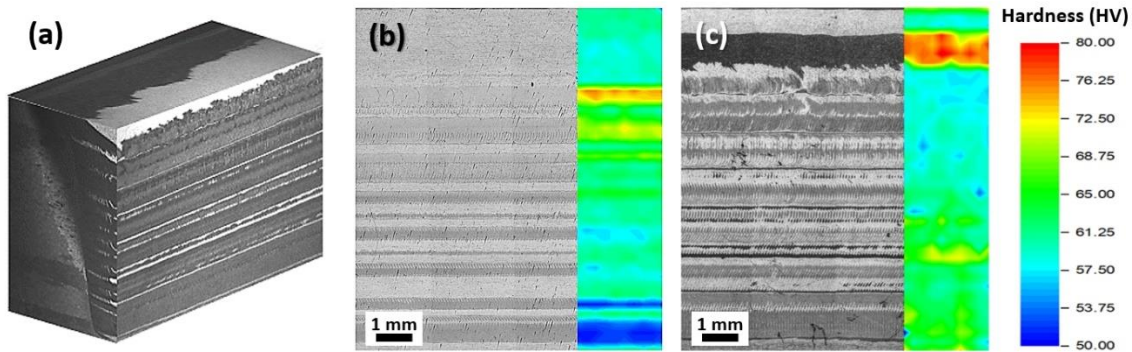


Figure 5-2. (a) 3-dimensional macrograph of A6R5 and longitudinal stir zone images of (b) A5R6 and (c) A6R5 along with microhardness maps. All images demonstrate the horizontal uniformity of the observed pattern throughout the longitudinal plane.

However, observations with increasing eccentric offset indicate a decrease in AA5052-AA6061 mixing due to less pronounced intermixing onion rings, despite the faint observation of onion rings between the colour contrast of the bands as seen in Figure 5-1. Cross-sectional macrographs of(e). In addition, Figure 5-2 shows longitudinal plane macrographs of the A5R6 and

A6R5 samples along with corresponding longitudinal plane hardness measurements. As expected, the images demonstrate the consistency of the observed features throughout the weld longitudinal plane.

To further analyze the differences between A5R6 and A6R5 samples, high magnification images and elemental mapping was done on areas marked A and B in Figure 5-1(c) as well as C and D in Figure 5-1(f), as shown in Figure 5-3. Due to the stark difference in the Mg content between parent metals (refer to Appendix A), EDX mapping of Mg (depicted as bright red) was utilized to determine the boundary between both alloys [173]. Figure 5-3(a)-(b), (e)-(f) confirm that the interfacial boundary is at the periphery of the outer region of the bands depicted in Figure 5-1. Cross-sectional macrographs of (c) (area A and B). Furthermore, both images show a high Mg content in the lightly etched locations between the inner and outer regions of the bands. This point is clear when considering the locations indicated by the black arrows in Figure 5-3 (i.e. inner band region), which are darkly etched, yet have similar Mg content to the lightly etched surrounding structure. Therefore, it can be inferred that the colour contrast originated either from differences in microstructural texture orientation or grain size, and not from material intermixing.

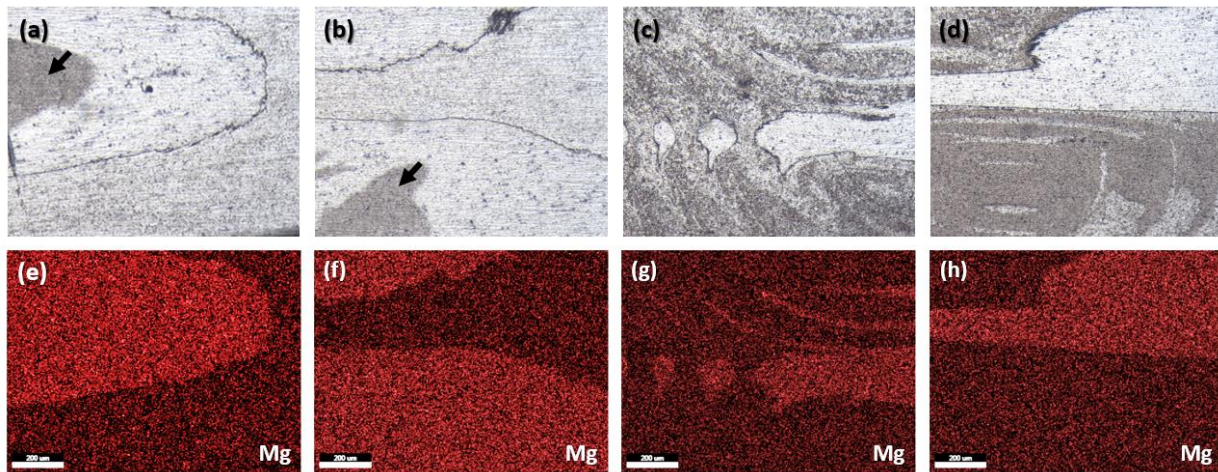


Figure 5-3. Higher magnification images of Figure 5-1(c) and Figure 5-1(f) and corresponding EDX mapping of Mg elements for regions A ((a) and (e)), B ((b) and (f)), C ((c) and (g)) and D ((d) and (h)).

In contrast, the images in Figure 5-3(c), (g) of sample A6R5-0.4 conclusively show that good mixing between AA5052 and AA6061 was achieved through formation of onion ring structures, which consists of intermittent areas of AA5052 (bright region) and AA6061 (dark

region) (area C). Such features, termed mechanical interlocking, are desirable in dissimilar friction stir welding, as they indicate enhanced integrity of the SZ [43], [49]. However, the lower region of this sample (area D) shown in Figure 5-3(d), (h) depicts minimal mixing of the parent metal, despite an observable onion ring feature in Figure 5-1(d). This suggests that the onion ring formation in the lower region of the SZ consists exclusively of AA6061 material. This can also be faintly observed in the A5R6 sample at the lower region of the SZ as shown in Figure 5-1(a).

### 5.3.2 Thermal cycle analysis

The thermal cycle of A6R6 at various mid-thickness points at different distances from the faying surface is shown in Figure 5-4. Measurements at locations AS10, AS15, and AS20 denote the position of the thermocouples on the AS being 10 mm, 15 mm, and 20 mm from the faying surface, respectively. Similarly, RS10, RS15, and RS20 designates the position of the thermocouples at the retreating side being 10 mm, 15 mm, and 20 mm from the faying surface, respectively. As expected, the two highest peaks recorded are from the closest thermocouples to the SZ, i.e. AS10 and RS10. Negligible differences in thermal history can be observed between the nearly overlapping data for AS15 and RS15 as well as between AS20 and RS20, since the points are relatively far from the stir zone and heat is expected to dissipate evenly in these regions.

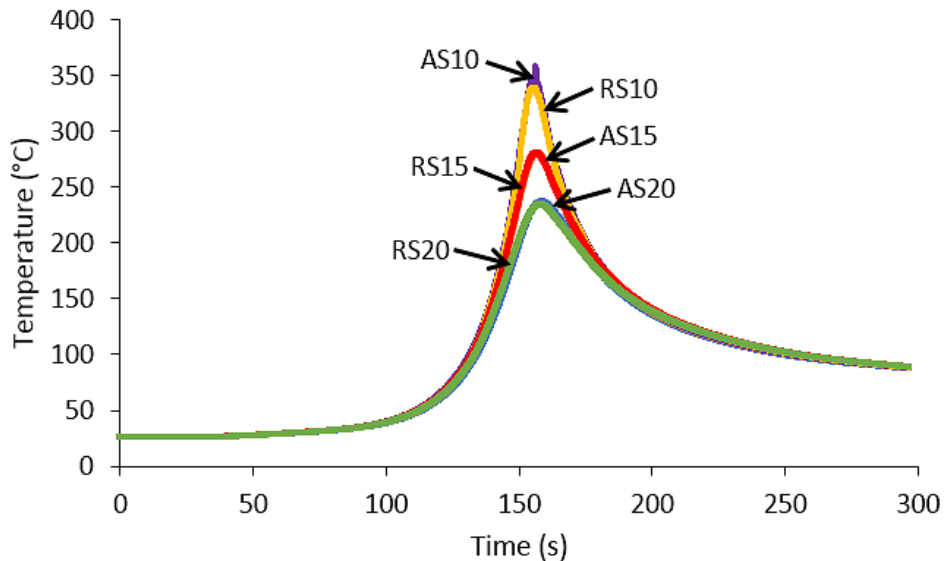


Figure 5-4. A6R6 thermal cycle at various mid-thickness points perpendicular to the faying surface.

Figure 5-5 shows the average peak values for all temperature measurement points for the A5R6 and A6R5 setups. Due to the distance from the faying surface, it can be assumed that any possible temperature change caused by the eccentric setup has dissipated and therefore temperature in this region is similar to the aligned setup. Hence, the values for all three setups are averaged and grouped in A5R6 and A6R5, respectively. In addition, A5R5 and A6R6 are also shown for reference. Error bars indicate the standard deviation over three measurements. All samples show an exponential increase of the peak temperature, with the rate of temperature increase expected to decrease until the maximum value it reached at the centre of the SZ. Except for the A5R5 samples, peak temperature measurements at AS10 consistently appear slightly higher compared to RS10 in all samples, with the difference ranging from 2°C to 21°C.

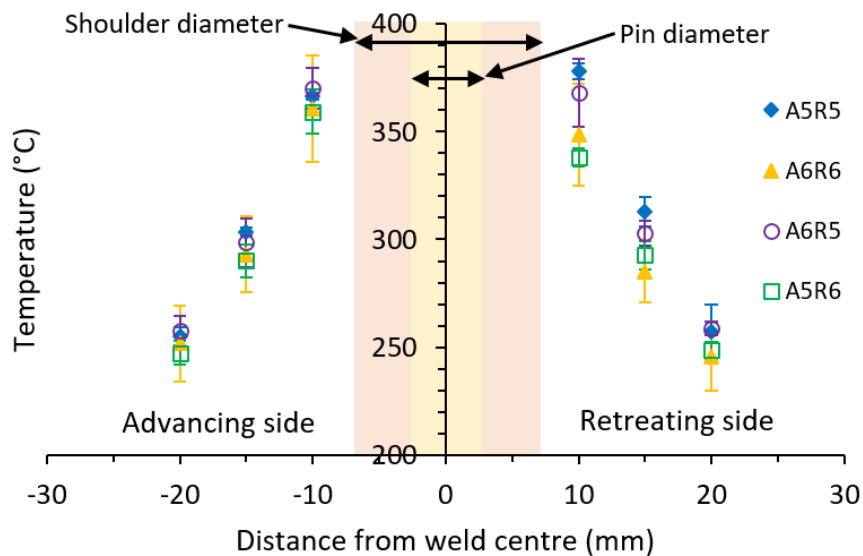


Figure 5-5. Temperature profile of various points from the weld centre.

### 5.3.3 Mechanical properties analysis

The mid-thickness hardness values of similar welded samples and dissimilar welded samples of A5R6 and A6R5 setups are shown in Figure 5-6. Analyzing the specimens designated in the AS, A5R6 reveals a gradual softening towards the SZ. In the SZ, the low hardness value continues and eventually increases to approximate AA5052 base metal values. Outside the SZ in the RS, the hardness values decrease to a minimum again, and then linearly increase towards a value of 108 HV in the AA6061 base metal.



It is evident that the A5R6 specimen mimics the hardness trend of similar AA5052 and AA6061 FSW profiles on the AS and the RS, respectively. Since the AA5052 alloy mainly occupies the AS of the SZ in the form of the bands observed, the values show a decreasing trend, but a higher value is recorded when transitioning away from the bands in the middle and RS of the SZ, where the local composition consists mainly of AA6061 material. A similar trend can be identified when the base metal position is reversed, i.e. A6R5 (Figure 5-6(b)), where the AS and RS follows the A6R6 and A5R5 trends, respectively.

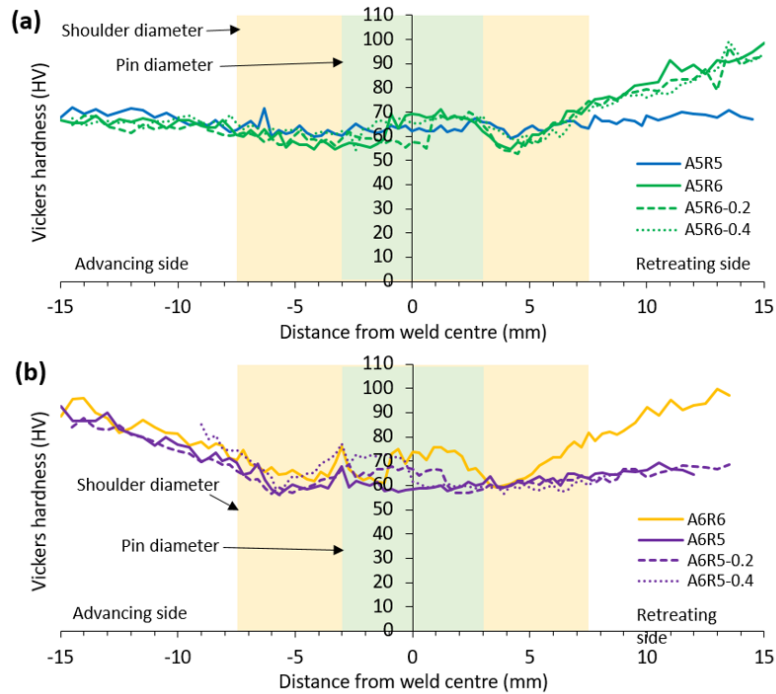


Figure 5-6. Mid-thickness hardness profiles for (a) A5R6 oriented samples and (b) A6R5 oriented samples.

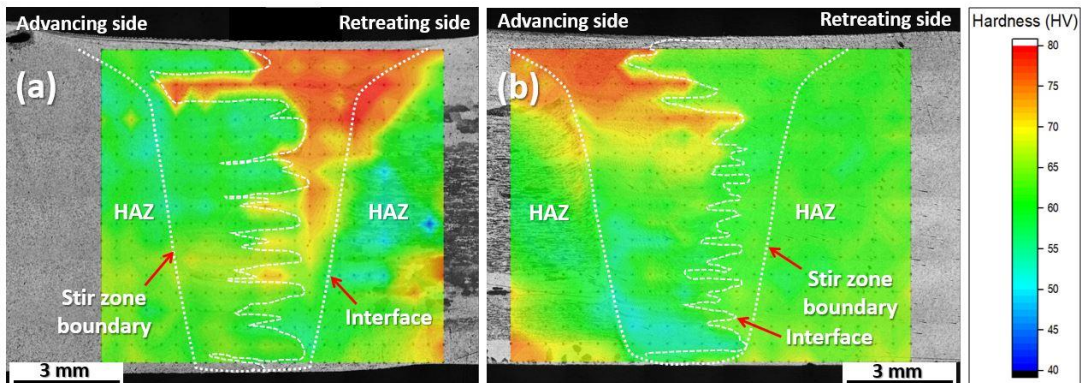


Figure 5-7. Stir zone hardness mapping of (a) A5R6 and (b) A6R5.

In addition, better material mixing in the A6R5 specimen appears to be correlated with a beneficial impact on the hardness of the joints, since gradual variation can be seen in the SZ, while the sharp SZ interface in the A5R6 weld contains a drastic change in microhardness values. This can be seen more clearly in the stir zone hardness mapping of A5R6 and A6R5 as shown in Figure 5-7. While an obvious asymmetry of hardness between the AS and RS of the top stir zone region can be observed for both samples, the A6R5 sample (Figure 5-7(b)) exhibits minimal hardness variation at the centre and bottom regions compared to the A5R6 sample (Figure 5-7(a)), where a sharp hardness ‘border’ can be seen dominating the RS of the stir zone.

The yield strength, average ultimate tensile strength (UTS), and average elongation of all the specimens are tabulated in Table 5-3 and depicted in Figure 5-8. In addition, Figure 5-9 presents the global stress-strain curve of samples taken from the tensile tests, with reference to the UTS of AA5052 and AA6061 base metals [181]. The yield strength and UTS values of dissimilar welded samples all fall in between the values of A5R5 and A6R6. However, the A6R5 group overall demonstrated higher UTS and elongation values compared to the A5R6 group. No observable trend can be seen when eccentricity is introduced for either material orientation.

Table 5-3. Transverse weld yield strength, UTS values, and elongation to fracture.

Sample	Yield strength (MPa)*	Ultimate tensile strength (MPa)	Elongation (%)
A5R5	137	216.6 ± 2.2	11.1 ± 0.3
A6R6	161	204.8 ± 2.8	5.0 ± 0.2
A6R5	141	209.8 ± 4.0	7.3 ± 0.3
A6R5-0.2	141	215.2 ± 1.4	7.6 ± 0.6
A6R5-0.4	140	209.6 ± 0.3	7.0 ± 0.6
A5R6	148	209.7 ± 1.5	6.5 ± 0.6
A5R6-0.2	144	205.4 ± 2.1	5.9 ± 0.6
A5R6-0.4	143	206.5 ± 1.1	6.1 ± 0.5

\* Values calculated using extensometer data.

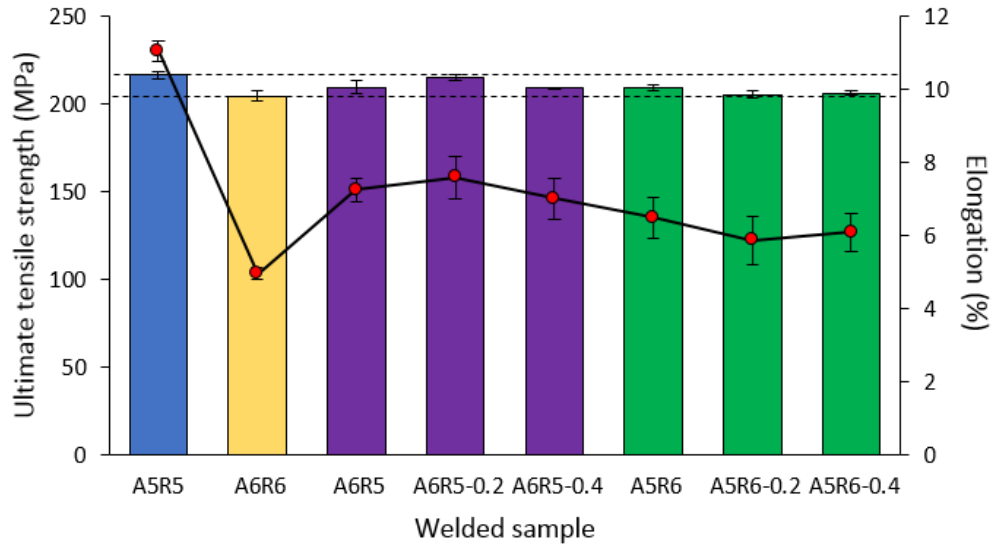


Figure 5-8. Ultimate tensile strength and elongation of samples. The bars represent the tensile strength (MPa) while the straight line and markers represent the elongation (%). Dashed lines represent tensile strength values of A5R5 and A6R6 for comparison.

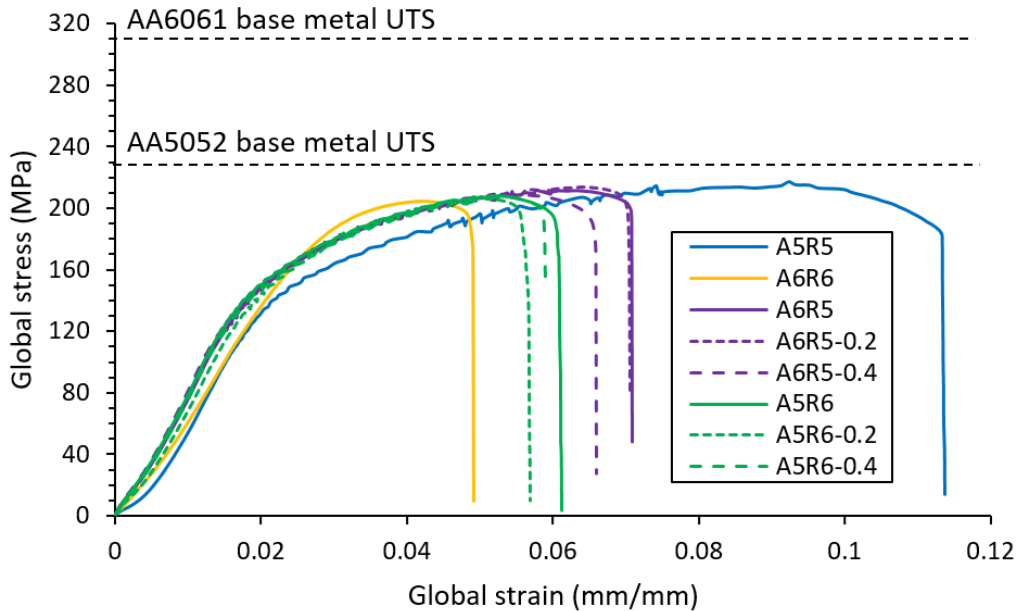


Figure 5-9. Global stress-strain curves for similar and dissimilar welded joints.

The A6R6 tensile coupons and all dissimilar welds fractured in the heat-affected zone (HAZ) of the AA6061 side, which is the area adjacent to the stir zone where the hardness is lowest (Figure 5-6). The A5R5 samples on the other hand fractured in the stir zone since the hardness is lowest in this region. Fractography was done on the samples as shown in Figure 5-10. For the

A6R6 samples, a quasi-ductile fracture mode is observed, where evidence of dimples and planar surfaces can be seen. On the other hand, a purely ductile mode is dominant in A5R5, where dimple structures are mainly observed throughout the fracture surface. Since fracture took place in the HAZ of the AA6061, all dissimilar welded samples show similar mixed fracture mode as A6R6.

Figure 5-11 depicts the DIC strain measurements for specimens A6R5-0.4 and A5R6-0.4 right before fracture. In both cases, fracture occurred in the HAZ on the AA6061 side, regardless of the base metal positioning. Interestingly, the images show that only the weld region and the AA5052 side are strained appreciably, while the AA6061 base metal endures negligible strain. The highest local strain recorded was in the HAZ of AA6061 ( $>30\%$  strain) before fracture. This suggests that the localized high straining and eventual fracture of the AA6061 HAZ is occurring after the onset of nonlinear behaviour of the AA5052, but before yielding of the AA6061.

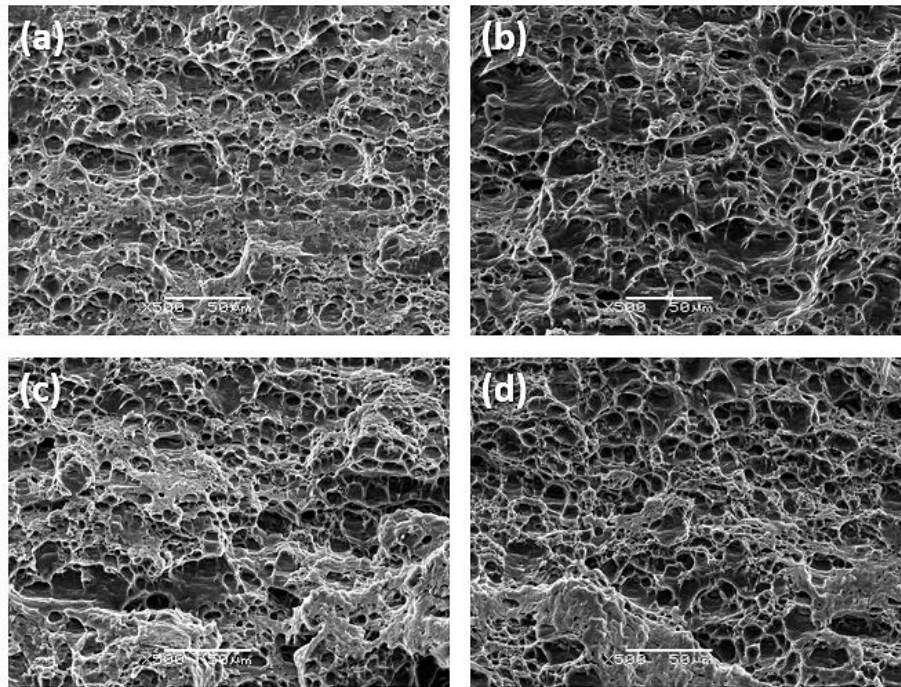


Figure 5-10. Fracture surface images obtained from tensile specimens for joints (a) A6R6, (b) A5R5, (c) A6R5, and (d) A5R6. Both dissimilar welding samples show a similar mixed fracture mode to A6R6.

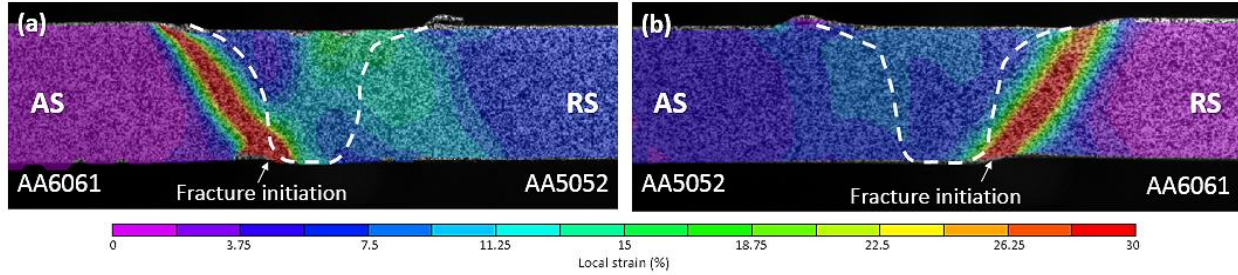


Figure 5-11. DIC images of (a) A6R5-0.4 and (b) A5R6-0.4 right before fracture. Fracture occurred in HAZ of AA6061 side.

### 5.3.4 Texture analysis

Figure 5-12(a)-(d) presents the transverse macrographs of Specimens A5R6, A5R6-0.4, A6R5, and A6R5-0.4, respectively. The white dashed lines represent the SZ boundary, while the red dashed boxes show the area of interest for electron backscatter diffraction (EBSD) analysis. Since it was found that AA6061 alloy was better suited to be placed in the AS for better mechanical performance, it is worthwhile to examine the A6R5 specimens in more detail. Thus, for the A5R6 specimens, only the top region was analyzed, while the top, middle, and bottom region were examined for A6R5 specimens. Henceforth, the direction and plane of reference will follow the normal direction (ND), transverse direction (TD), and rolling/welding direction (RD) designation, as shown in Figure 5-12(c). As such, the transverse macrographs seen in Figure 5-12 correspond to the ND-TD planes.

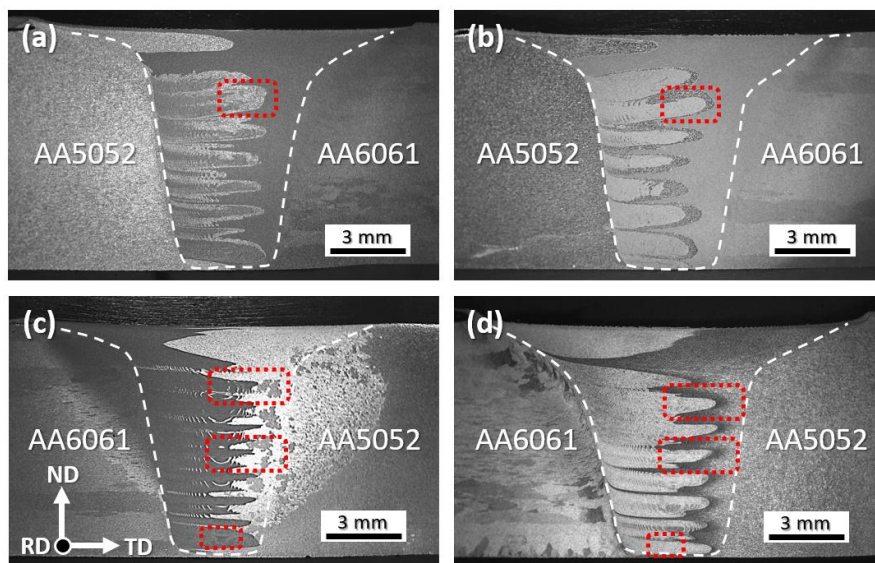


Figure 5-12. Transverse macrograph of (a) A5R6, (b) A5R6-0.4, (c) A6R5 and (d) A6R5-0.4.

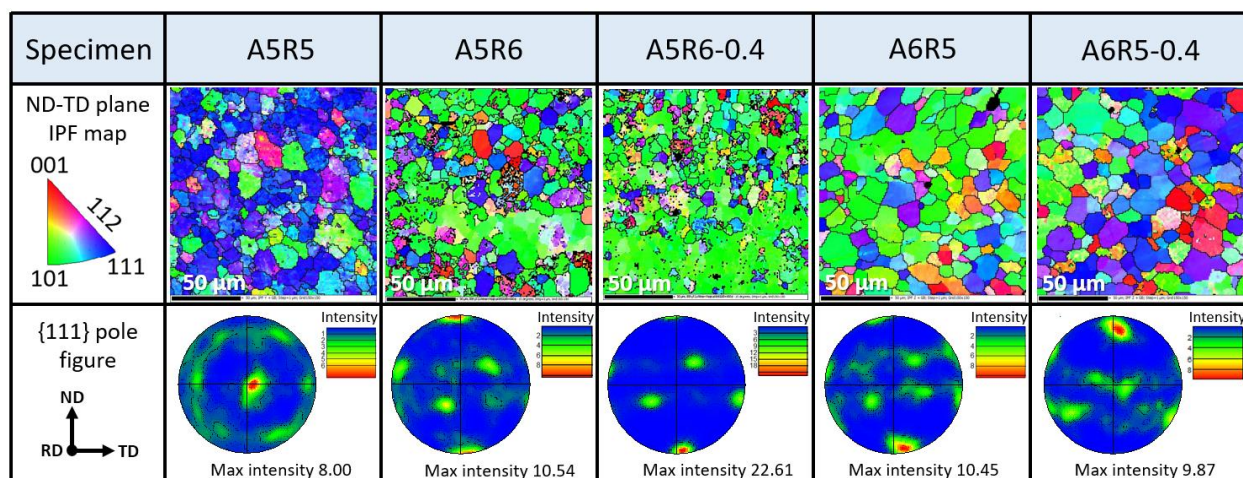


Figure 5-13. IPF maps of ND-TD plane and {111} PFs for A5R5, A5R6, and A6R5 specimens of the top region.

Figure 5-13 depicts the inverse pole figure (IPF) maps of the ND-TD plane and its respective {111} pole figures (PFs) for the top region of A5R5 (reference specimen), A5R6, and A6R5 specimens. The dark lines in the IPF maps are high angle grain boundaries (HAGBs), which are defined as any misorientation angle  $>15^\circ$ . Comparing the grain size, the grains of A6R5 specimens show a comparable size with the A5R5 specimen, but much finer grains were observed in the A5R6 specimens.

The IPF maps and {111} PF of the A5R5 sample show a strong crystallographic orientation of the {111} texture parallel to the ND-TD plane. This aligns quite well with the  $\langle 110 \rangle$  shear direction and the {111} shear plane of the tool pin, which has been well documented by previous works [117], [182]–[185]. However, a stark contrast can be observed for all dissimilar welds, where a drastic  $90^\circ$  shift of {111} plane orientation occurs from the parallel orientation of the commonly reported ND-TD plane towards the RD-TD plane. This is consistent regardless of base metal positioning and aligned or eccentric setup. While the maximum intensity of the {111} PFs for all dissimilar welding specimens show an increase compared to the A5R5 specimen, no agreeable trend can be seen with varying eccentricity and eccentric setup.

The reason for this drastic change is postulated to be due to the change in the material flow caused by the subtle differences in the base metal flow stress, which is imposed on the tool pin. A careful observation of the protruding bands originating from the AS stir zone boundary reveals that multiple onion-ring shaped features are formed by the threaded and tri-flat pin profile (Figure

5-3), which suggests chaotic material mixing, which is reported elsewhere for this type of tool geometry [71].

Figure 5-14 and Figure 5-15 shows the stir zone IPF maps (in ND-TD plane) of the A6R5 and A6R5-0.4 specimens, respectively. Since the etching contrast in the stir zone has been identified as the two distinct base metals from the respective base metal positioning (i.e. AA6061 on the left side and AA5052 on the right side), both areas were analyzed at the top and middle regions.

Both specimens generally show the same trend of equiaxed grain morphology with progressive grain refinement from the top region to the bottom region [37], [186]. The grain size of each stir zone region is also comparable despite the difference in eccentricity setup. However, the top right regions for both A6R5 and A6R5-0.4 (Figure 5-14(b) and Figure 5-15(b)) show a slightly elongated structure. One possible reason is because of the observed area being very close to the thermo-mechanically affected zone (TMAZ) and shoulder driven material flow (seen as the wider area at the top of the stir zone in Figure 5-12) that exerts larger strain and material shearing during FSW, which may induce geometrical dynamic recrystallization (GDRX) [187], [188].

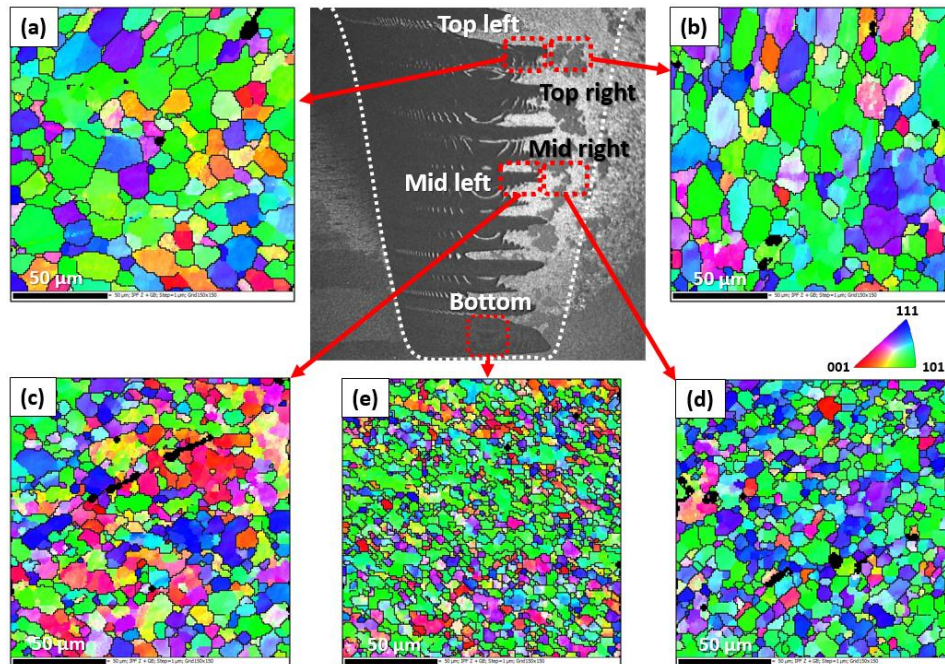


Figure 5-14. Stir zone EBSD mapping of (a) top-left, (b) top-right, (c) mid-left, (d) mid-right, and (e) bottom for A6R5.

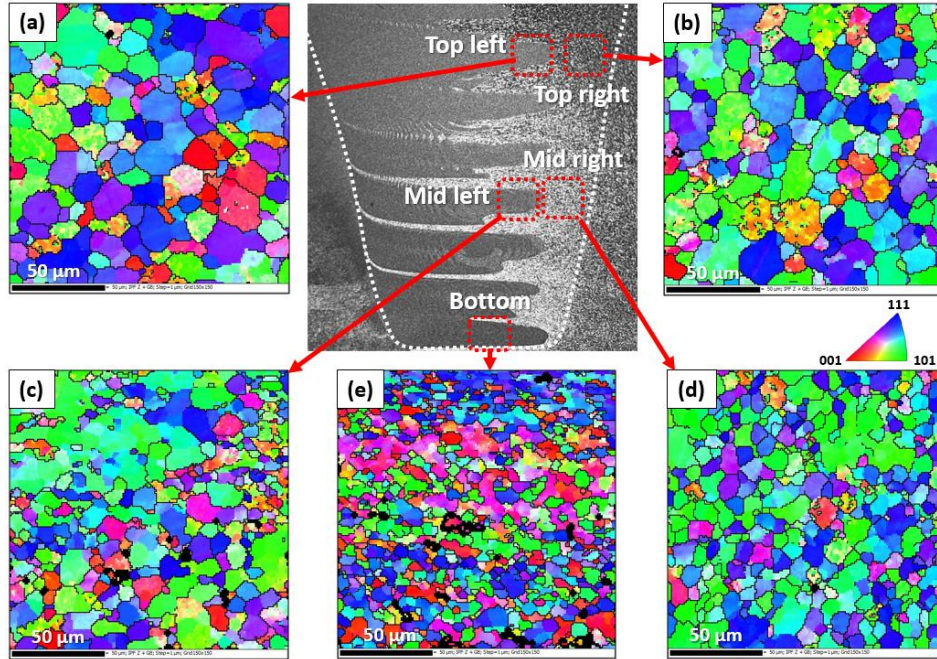


Figure 5-15. Stir zone EBSD mapping of (a) top-left, (b) top-right, (c) mid-left, (d) mid-right, and (e) bottom for A6R5-0.4.

Figure 5-16 depicts the recrystallization fraction of selected stir zone regions of A6R5 and A6R5-0.4. The percentages of recrystallized, sub-structured, and deformed grains are summarized in Figure 5-16. All regions show predominantly deformed grains, with a sizable fraction of recrystallized and sub-structured grains at the top-left regions of both samples. However, both recrystallized and sub-structured fraction decreases drastically in the mid-left region and transforms into an almost fully deformed state at the bottom region of A6R5 specimen. On the other hand, while the sub-structured fraction shows a more steady decline from the top region to the bottom, the recrystallized fraction is retained for all observed regions for A6R5-0.4.



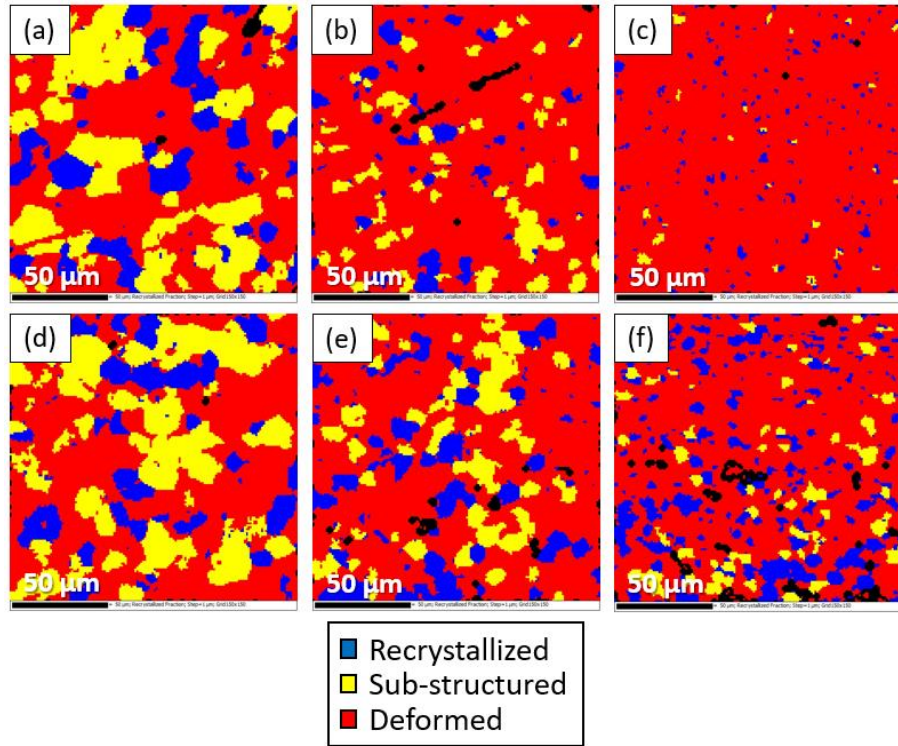


Figure 5-16. Recrystallization fraction of A6R5 stir zone regions: (a) top left, (b) mid left, (c) bottom. Recrystallization fraction of A6R5-0.4 stir zone regions: (d) top left, (e) mid left, (f) bottom.

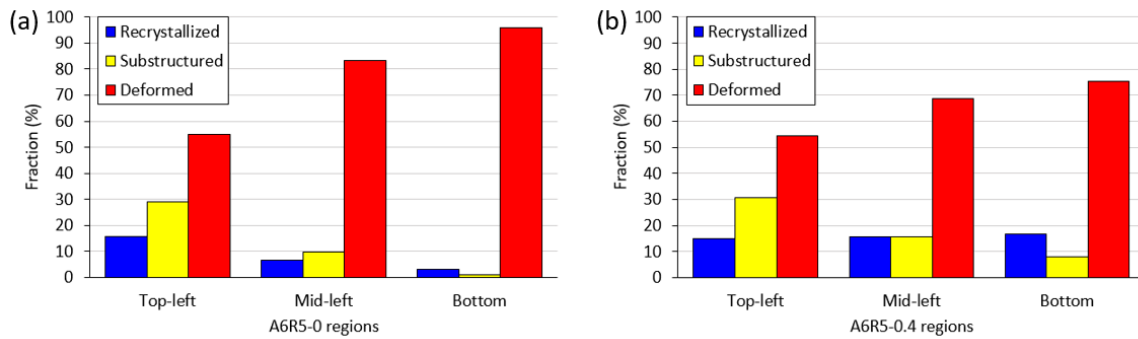
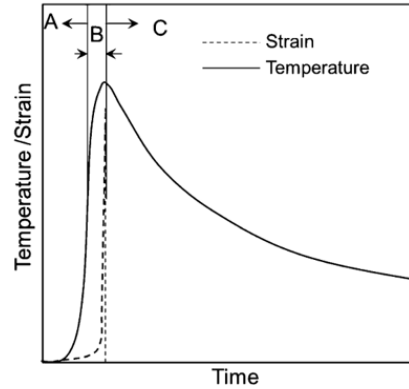


Figure 5-17. Recrystallized fraction of stir zone regions of (a) A6R5 and (b) A6R5-0.4.



	Zone A	Zone B	Zone C
Position of FSW tool	Approaching observed region	Traverses observed region	Moving away from observed region
Physical processes	<ul style="list-style-type: none"> <li>• Static recovery</li> <li>• Static recrystallization</li> <li>• Grain growth</li> </ul>	<ul style="list-style-type: none"> <li>• Dynamic recovery</li> <li>• Dynamic recrystallization</li> <li>• Grain growth</li> </ul>	<ul style="list-style-type: none"> <li>• Static recovery</li> <li>• Static recrystallization</li> <li>• Grain growth</li> </ul>

Figure 5-18. Schematic variation of temperature and strain in the stir zone of a friction stir weld with the different physical processes in each zones [97].

The observations obtained can be explained based on the thermo-mechanical processes undergone by the material during FSW. The material in an FSW joint typically undergoes several physical processes at elevated temperatures during the whole weld cycle. Figure 5-18 presents the schematic variation of temperature and strain in the stir zone of a friction stir weld with its respective physical processes that can occur in each zone [97]. The maximum temperature and maximum strain is simultaneously reached in Zone B, while Zone A and Zone C mainly undergo only a temperature cycle. Due to this distinction, the physical process differs as either a static or a dynamic process. However, since all the three zones are experienced in all FSW processes, static/dynamic recovery and recrystallization as well as grain growth contributes to a certain degree to the final structure [45]. Through neutron diffraction observations, Woo et al. also demonstrated that the preferred texture orientation in the stir zone is not the result of the thermal cycle alone but a combination of these thermo-mechanical effects [189].

Strain, strain rate, and temperature gradients can be expected throughout the thickness of the stir zone, where the majority of the heat input is generated as a result of the frictional heat at the shoulder-workpiece interface. The additional heat and subsequent extended cooling period at the top region provides the means for grain growth and dynamic/static recrystallization to occur, resulting in much coarser grains and more recrystallized and sub-structured grains (Figure 5-17). The predominantly fine grains with deformed morphology observed at the bottom region suggests

that the region undergoes severe plastic deformation but generated insufficient heat input to induce grain growth at the same time mitigated static/dynamic recrystallization. However, the consistent recrystallized fraction and a more steady decrease of substructured grains for the tool eccentric setup may suggest that additional heating occurred through larger tool-workpiece contact volume that enhances dynamic/static recrystallization and/or dynamic/static recovery of grains.

Figure 5-19 and Figure 5-20 shows the PFs, IPFs, and orientation distribution functions (ODFs, for  $\phi_2 = 45^\circ$  section) of A6R5 and A6R5-0.4 samples, respectively. The blue 3D cube mid-left of the image represents the designated plane of reference. As presented earlier, the PFs and IPFs of both samples indicate that a strong  $\{111\}$  texture orientation plane normal to the normal direction (RD-TD plane) is observed throughout the top, middle, and bottom region, with the exception of top left region of A6R5-0.4 where the IPF of the RD-TD plane showed a preferred  $\{112\}$  orientation. The maximum intensity of the IPFs is also seen to be increasing from the top region to the bottom region, indicative of an increasing preference to the  $\{111\}$  texture orientation in the RD-TD plane.

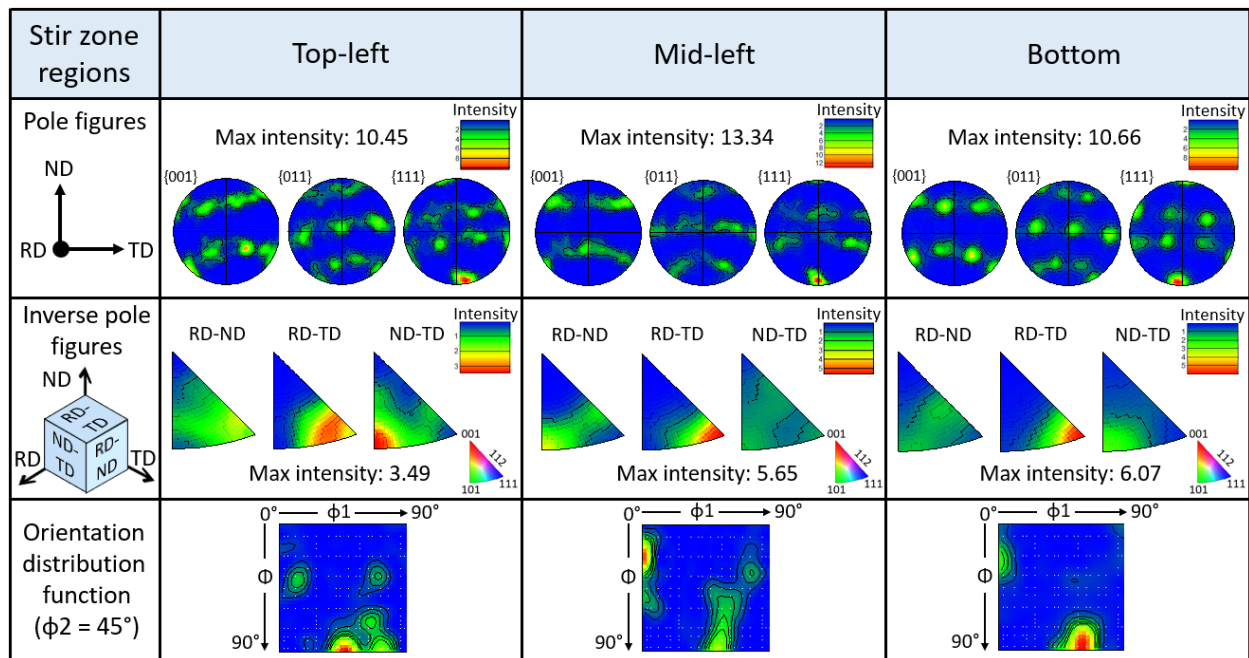


Figure 5-19. PFs, IPFs, and ODFs of A6R5 stir zone regions.

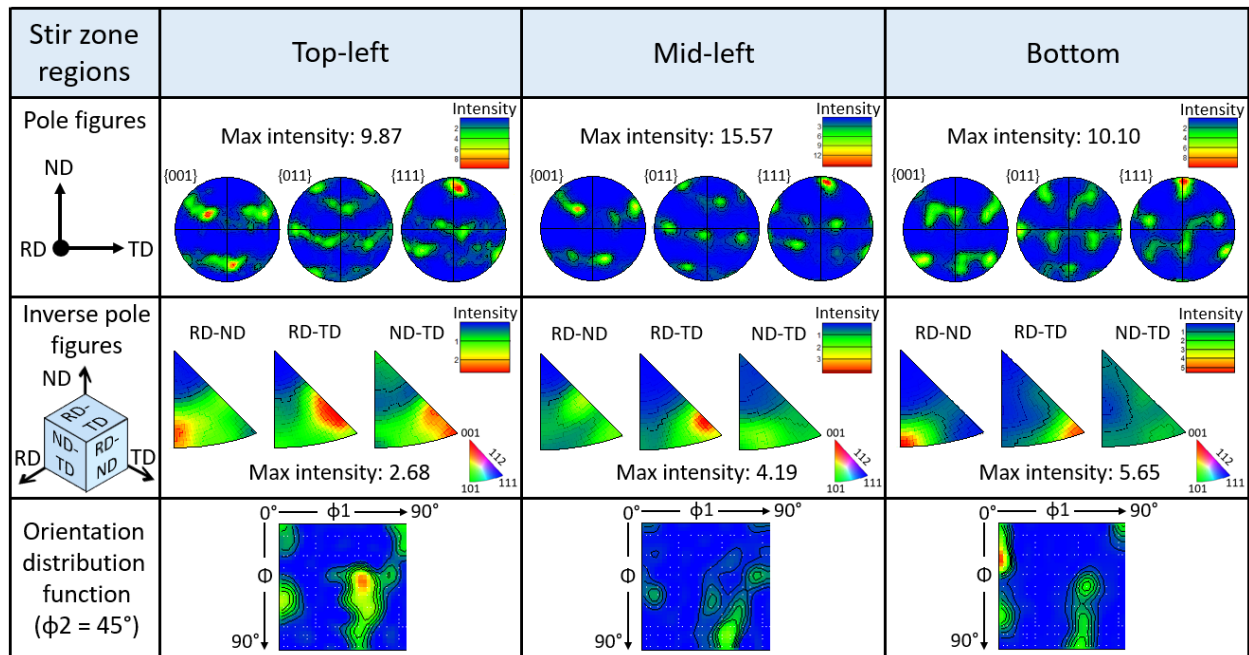


Figure 5-20. PFs, IPFs, and ODFs of A6R5-0.4 stir zone regions.

Table 5-4. Texture and fibre components for selected stir zone regions of A6R5 and A6R5-0.4 (after Hirsch and Locke[190]).

Stir zone region	A6R5	A6R5-0.4
Top left	Rotated W	Z and rotated W
Mid left	Rotated W	Rotated W
Bottom	Rotated W	Rotated W

Referring to Figure 5-13 and based on works by Toth et al.[191] and Li et al.[192], all the  $\{111\}$  PFs of dissimilar welding indicate a predominant  $\{111\}\langle -11-2 \rangle A_i^*$  ideal shear texture. Similar results were reported by Wang et al.[164]. In addition, the texture components of the stir zone regions of the A6R5 specimens were analyzed and summarized in Table 5-4 based on [190], [193]. Both stir zones consist primarily of a rotated W  $\{001\}\langle 110 \rangle$  component, with the exception of the top left of A6R5-0.4, where a  $\{111\}\langle 1-10 \rangle$  Z component is also present. It can be seen that the texture morphology in the A6R5 specimens are more consistent throughout the stir zone. These texture components are commonly associated with rolling/deformation processes, confirming that severe plastic deformation occurred in both cases, as depicted in Figure 5-17.

## 5.4 Discussion

### 5.4.1 Effect of base material positioning on material mixing

In dissimilar FSW, an important parameter that emerges relates to the selection of the alloy that should be placed on the advancing side to achieve the desired quality of the weld, e.g., better microstructure, better tensile properties at room temperature, or avoidance of weld defects. As a rule of thumb, it has been generally suggested that a harder material should be placed in the advancing side [74], [144], [148], [153], [164], [165], [194]. This region undergoes more rigorous shearing activity, as indicated by the sharp stir zone boundaries (Figure 5-1), and higher peak temperature (Figure 5-5). More importantly, the rigorous shearing of the harder material facilitates the intermixing of the stir zone. In the present study, the results seem to suggest that AA6061, which is the harder material, is the better option to be placed in the AS since more intermixing between base metals could be observed (Figure 5-1(c)). However, since the hardness value is temperature dependent, and material at the leading side of the tool does undergo preheating, the flow stress of the material needs to be considered as well. Hardness ( $H$ ) can be directly correlated to flow stress of material ( $\sigma$ ) at a given constant strain ( $\varepsilon$ ) through a constraint factor,  $C$  [195]:

$$H(\varepsilon) = C \cdot \sigma(\varepsilon) \quad (\text{Eq.5-1})$$

Therefore, the observable change in temperature dependent flow stress appears to be linearly related to the change in hardness of the samples as temperature increases.

In this regard, the UTS of alloys can be seen as a good approximation of flow stress of materials. Figure 5-21 shows the UTS of selected Al alloys as a function of temperature available in [196]. Due to data limitations, the UTS of AA2024-T351 can be considered to be similar to that of AA2024-T3, while the UTS of AA6061-T651 is similar to the T6 temper condition. As can be seen in Figure 5-21, all of the Al alloys show a decreasing trend with increasing temperature, eventually plateauing as the melting temperature is reached. This figure also illustrates that AA6061 maintains a higher UTS (flow stress) compared to AA5052 up to the maximum stir zone temperature range (80% to 90% melting temperature of alloy). It can therefore be suggested that AA6061 is better suited to be placed in the AS to facilitate plastic deformation and material intermixing.

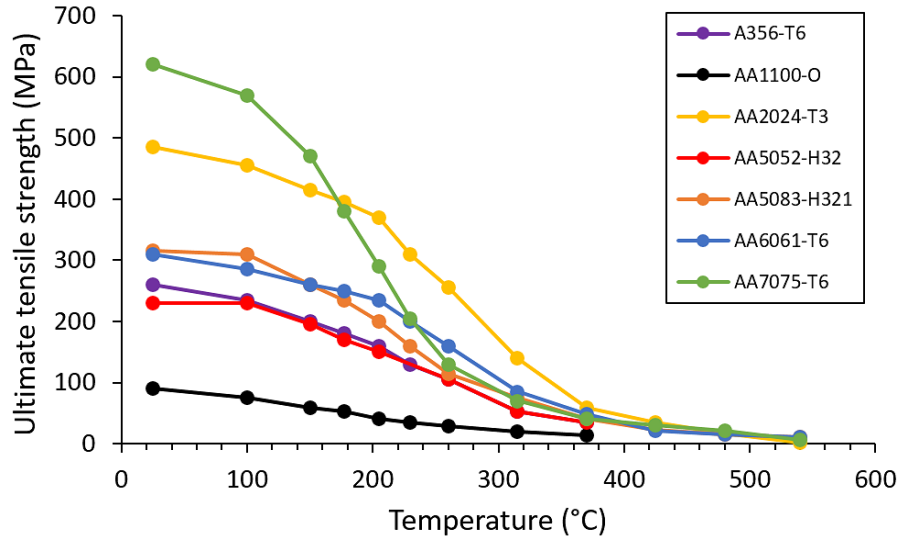


Figure 5-21. Ultimate tensile strength vs. temperature for various Al alloys [196].

To further understand the significance of flow stress in determining the metal positioning, Table 5-5 shows the previous works done on FSW of dissimilar Al, which focuses on the effect of base material positioning on material mixing. While numerous other works on dissimilar aluminum alloy FSW joints are available [48], most are not included here due to lack of comparable data such as the dependency of the UTS on temperature. Note that the preferred material on the AS in the following discussion is based on achieving a higher degree of material mixing in the SZ.

Table 5-5 shows that the preferred AS base metals are materials with higher UTS (higher hardness) at ambient temperature (refer to Figure 5-21), except for works by Khodir and Shibayanagi, Guo et al. and Park et al. [150], [154], [173]. By considering the UTS vs. temperature data, however, some of these exceptions can be further explained. In the cases of Guo et al. [150] and Khodir and Shibayanagi [154], the AA7075 alloy has a higher room temperature UTS compared to AA2024 and AA6061. This alloy is unique in the sense that its UTS drops significantly with increasing temperature and matches that of AA2024 and AA6061 above 250°C, beyond which, its UTS becomes even lower (especially when considering the peak SZ temperature). It is known that the work piece at the leading edge of the tool undergoes preheating before undergoing the plastic deformation process, thus the sheared material is already at an elevated temperature before tool contact. Therefore, it is postulated that because of this unique

feature, both AA2024 and AA6061 alloy are seen as a better candidates for AS positioning, despite having a lower UTS at room temperature compared to AA7075.

Table 5-5. Previous works on dissimilar Al FSW with reported preferred base metal positioning [94], [154], [156], [173], [197]–[200].

No.	Author(s)	Year	Thickness (mm)	Dissimilar material	Optimum AS material for mixing	Material with higher UTS at 25°C
1	Lee et al.	2003	4	A356 & AA6061	AA6061	AA6061
2	Khodir & Shibayanagi	2008	3	AA2024-T351 & AA7075-T6	AA2024	AA7075
3	Park et al.	2010	2	AA5052-H32 & AA6061-T6	AA5052	AA6061
4	Guo et al.	2012	4.4	AA1100 & AA6063-T5	AA6063	AA6063
5	Thibeault	2012	12.7	A356 & AA6061-T6	AA6061	AA6061
6	Izadi et al.	2013	6.35	AA2024-T351 & AA6061-T6	AA2024	AA2024
7	Guo et al.	2014	6.3	AA6061-T6 & AA7075-T6	AA6061	AA7075
8	Kishore	2015	-	AA5083 & AA6061	AA5083	AA5083
9	Our work	2019	9.5	AA5052-H32 & AA6061-T651	AA6061	AA6061

On the other hand, works by Park et al.[173], which utilized similar alloys and temper/hardened conditions to the current study suggested that AA5052 is a better AS material. This can be attributed to the use of thin 2 mm samples, which significantly impacts the heat generation and the dynamics of the material flow, as seen in observations of only a singular onion ring formation in their work. In addition, the advance per revolution ( $APR = v/\omega$ ) used in their work was 0.05 mm/rev compared to 0.08 mm/rev in the current study, which indicates more heat

was produced due to the relatively lower APR. This suggests a starkly different temperature distribution may be present, subsequently effecting the overall microstructural evolution and hardness change. While a rather negligible temperature difference can be suggested for thin sheets FSW, a study by Martinez et al. on joints in 13 mm thick AA7449 alloy suggested that the top and bottom of the stir zone peak temperature can differ by as much as 148°C [201].

Even though exceptions may exist, it can be seen that UTS vs. temperature is a better indication of optimum base material positioning, which agrees well with previous works [43], [165]. It should also be noted that material mixing is not governed by flow stress alone. A more precise analysis on this matter should also consider other factors such as material adhesion, welding parameters, and material thickness. In addition, as discussed in Section 4.4.1, the pin profile such as the threaded with three flats profile used in this study also play a major role in facilitating the formation of multiple horizontal bands, which enhances mechanical interlocking of the alloys [94].

#### **5.4.2 Effect of eccentricity on material deposition**

Although its influence on mechanical properties appears to be minimal, tool eccentricity shows an observable trend with regards to stir zone material flow. Figure 5-22 illustrates a schematic top view of a material deposition mechanism. The material deposition around the tool follows the Schneider-Nunes kinematic model [117]. In the RS, the material in the leading end of the tool (Quadrant II) is simply extruded at the trailing end of the tool's RS (Quadrant III). In contrast, the material at the leading end of the tool's AS (Quadrant I) is rotated several times before being deposited at the trailing end of the AS (Quadrant IV). The horizontal bands seen in Figure 5-1 are therefore materials accumulated from Quadrant I and deposited in Quadrant IV, indicative of a 'first-in last-out' trend, i.e. the first material accumulated will be the last deposited [97]. More evidence of this is the fact that the predominant SZ material on the AS is the same as the base material positioned on this side as shown in Figure 5-1 and Figure 5-3.



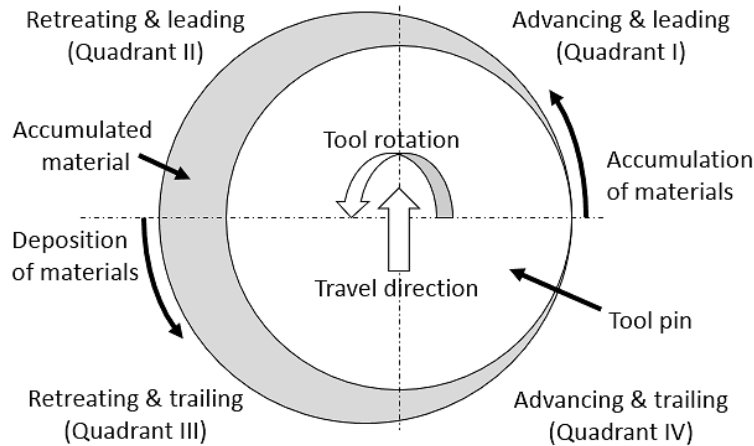


Figure 5-22. Top view schematic of material deposition mechanism adapted from [97].

The effect of eccentricity on material deposition can therefore be hypothesized as follows. In the case of A5R6, both alloys were systematically deposited in their respective quadrants, forming a distinct interface. However, expansion of the horizontal band area with increasing eccentricity suggests that more shearing and material accumulation was initiated at Quadrant I, which results in more AS material deposited in Quadrant IV. This can be attributed to an increase in shear surface radius with larger magnitudes of eccentricity, retaining the AS material longer in the rotational field, effectively enhancing the material shearing activity [202]. While it is postulated that the colour contrasts (Figure 5-1) between the inner and outer regions are caused by a change in the local shearing activity and texture orientation due to tool eccentricity, more extensive work is needed to confirm this.

On the other hand, the high flow stress from the harder AA6061 material placed in the AS in the A6R5 specimen suggests that portions of the accumulated AA6061 in Quadrant I are effectively sheared and mixed with the softer AA5052, increasing the intermixing between both materials. However, when more eccentricity is imposed up to 0.4 mm, a larger volume of Quadrant I material is accumulated and subsequently deposited in Quadrant IV. It is postulated that this larger volume of deposited AS material would consequently hinder intermixing with the RS material by producing highly sheared zones (onion ring formation) only within itself (Figure 5-3(h)). Further investigation regarding changes in applied force, torque, temperature, strain, and strain rates may also help to explain the effect of tool eccentricity on the overall FSW process and material deposition.

### 5.4.3 Effect of microstructural evolution on mechanical properties

Heat input is an FSW process variable, which significantly influences the weld properties. As mentioned earlier, temperature measurements of A6R6 and dissimilar welding the samples consistently show a higher peak temperature on the AS, 10 mm from the faying surface (AS10) as compared to the RS temperature at a similar distance (RS10). This agrees well with previous findings by others [171], [172], [203], [204]. It is suggested that this is due to higher shearing activity occurring in the AS compared to the RS as observed by the clear stir zone boundary in the AS in Figure 5-1 and as discussed in the description of Figure 5-22 [116]. However, A5R5 shows approximately 11°C higher average peak temperature with narrow scatter at RS10 compared to AS10. The reason for this anomaly is currently unknown.

Measurements of the heat affected zone (HAZ) hardness showed negligible differences between aligned and eccentric setups for both A5R6 and A6R5. Even so, as mentioned earlier, minor differences in stir zone hardness due to the work piece positioning was observed. Hardness can be linearly correlated to the yield strength ( $\sigma_y$ ) of the material. In general, yield strength is dependent on the state of microstructure and includes three contributions from the linear addition rule [205]:

$$\sigma_y = \sigma_i + \sigma_{ss} + \sigma_{ppt} \quad (\text{Eq.5-2})$$

where  $\sigma_i$  is the intrinsic strength of Al matrix,  $\sigma_{ss}$  is the strength contribution from solid solution strengthening, and  $\sigma_{ppt}$  is the strength contribution from the precipitates alone or from the precipitates and natural aging clusters. In heat treatable alloys such as AA6061,  $\sigma_{ppt}$  plays a significant role in enhancing the strength of the material. However, through the welding thermal cycle, the metastable strengthening precipitates are both partially dissolved and partially coarsened into undesirable precipitates, which leads to a decrease in strength [97].

Since the SZ peak temperature of AA6xxx series Al alloys has been measured in previous works to be generally  $\geq 70\%$  of the melting temperature [206]–[208], the heat is sufficient to dissolve the strengthening precipitates and partially restore the hardness in this region. This is done through reprecipitation of particles via natural aging after the welding process, hence the noticeable ‘W’ shape hardness profile [209]. However, the low value regions of the profile in welded heat-treatable alloys such as AA6061 has been attributed to the dissolution of needle-

shaped  $\beta''$  strengthening precipitates and the growth of rod-shaped  $\beta'$  or platelet-shaped  $\beta$  non-strengthening precipitates [125], [182], [210]. Growth of these precipitates during the cooling leg of the thermal cycle leads to solute depletion in the Al matrix. This in turn reduces the density of precipitates, subsequently softening the HAZ region.

Based on work by Frigaard et al.[210], the initiation temperature for dissolution of  $\beta''$  precipitates and growth of  $\beta'$  precipitates (during the cooling period) is predicted to be 220°C. It is evident that all measured temperatures in Figure 5-5 are well beyond this threshold. Interestingly, the hardness profiles (Figure 5-6) indicate that the softened region of HAZ is rather large, covering more than 15 mm from the weld centre on both sides, even though the lowest value is close to the SZ. Figure 5-23 demonstrates the correlation between the observed hardness and the temperature measurements. The hardness shows a gradual increase in both directions towards the base metal (BM) value of 108 HV, in good agreement with the peak temperature reaching just above the dissolution temperature of  $\beta''$  precipitates, a threshold reached at a larger distance from the weld centre.

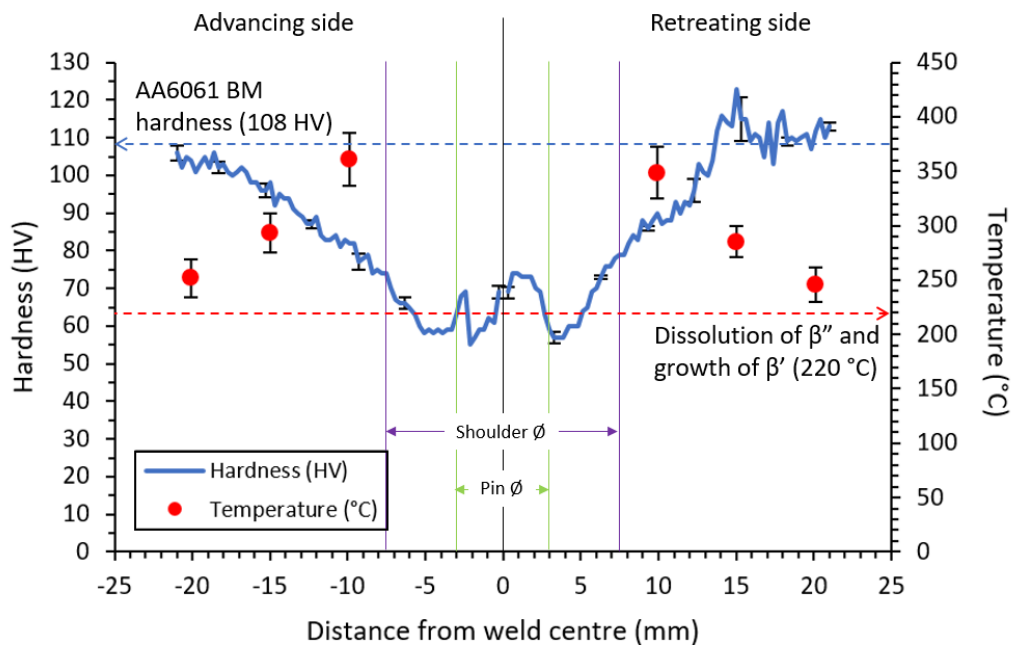


Figure 5-23. Temperature and hardness profile of A6R6 with respect to distance from weld centre.

On the other hand, the strength of non-heat treatable AA5052 alloys relies on solid solution strengthening ( $\sigma_{ss}$ ) and dislocations formed during cold working [97]. The bowl-shaped hardness

profile of AA5052 can be attributed to stress relief and recovery in the strained structure, i.e. reduced dislocation density in the SZ. The inherent dislocation densities in 5xxx series Al alloy base materials depend on the tempering conditions. Previous work by Sato et al.[182] on AA5083-O alloy showed that the hardness change is effectively negligible, while Peel et al.[211] demonstrated that the reduction in dislocation density after welding of AA5083-H19 caused a pronounced softening in the weld region. Since the current work utilizes base material with an H32 temper (strain hardened and stabilized with a lower dislocation density), the hardness reduction is kept at a minimum, gradually increasing towards the base metal values outside the stir zone.

Figure 5-8 shows that overall, the dissimilar welded samples demonstrate a better tensile strength and elongation compared to A6R6. This can be explained in terms of the global stress-strain curves summarized in Figure 5-9. As can be seen in this figure, A6R6 exhibits a smooth straining curve until fracture. In contrast, A5R5 reaches a higher elongation, but with serrated curves throughout the plastic region. This phenomenon is caused by the Portevin Le Chatelier (PLC) effect, due to period pinning of dislocations by larger Mg atoms in the solid solution [212]–[214]. The plastic region of the curve shows a sudden upward spike when the dislocation movements are pinned by the Mg atoms, followed by an abrupt dip once the load is sufficient enough to overcome it, repeating the process until fracture. Similarly, the same PLC effect could be observed for the dissimilar welded samples. In addition, the local strain distribution DIC images in Figure 5-11 further reveal that other than the HAZ of AA6061 side and the SZ, all dissimilar samples show local straining in the AA5052 side where the PLC effect takes place. This proves that the enhanced elongation in the dissimilar welded samples (Figure 5-9) were facilitated by the straining of AA5052 side, but this is also limited by the lower ductility of AA6061 HAZ which experiences strain localization early in the test. Therefore, it is suggested that a viable option to enhance the strength and elongation of AA6061 FSW joints is by pairing it with AA5052 instead of the typical similar alloy welding.

## **5.5 Conclusion**

Dissimilar friction stir welding (FSW) of AA5052-AA6061 was successfully conducted with different base material positioning and tool eccentricity setup. The findings from this study can be summarized as follows:

- An increase in the transverse weld ultimate tensile strength and elongation can be achieved with all dissimilar welding setup, in comparison with similar AA6061 FSW joints.
- Positioning the AA6061 on the advancing side (AS) results in better overall mechanical properties in dissimilar welds with up to 215 MPa UTS and 7.6% elongation, and was associated with better material intermixing.
- Higher peak temperatures were generally observed in the AS regardless of base material positioning, where peak temperatures of more than 350°C were recorded by the thermocouple located closest to the stir zone.
- Tool eccentricity enhances AS material flow in the stir zone, but reduces dissimilar material mixing when higher eccentricity is present, particularly when the AA6061 is positioned on the AS.
- A strong {111} texture parallel to the RD-TD plane was observed for all dissimilar welded samples, as opposed to the typical orientation preference to the ND-TD plane, which is roughly parallel to the shear plane of the tool pin.
- Increasingly fine equiaxed grains can be observed for A6R5 and A6R5-0.4 specimens from the top to the bottom of the stir zone.
- All stir zone regions for A6R5 specimens consistently show a strong rotated W {100}<1-10> rolling/deformation texture component.

## Chapter 6: Effects of tool eccentricity on process response variables of friction stir welds

This chapter evaluates the effects of tool eccentricity on process response variables of AA6061 friction stir welds. Most of the information presented here is taken from the submitted manuscript ‘Evolution of process parameters in friction stir welding of AA6061 aluminum alloy by varying tool eccentricity’, which is currently under review in the International Journal of Advanced Manufacturing Technology.

### 6.1 Introduction

In FSW, independent process variables such as spindle rotational speed and weld speed set prior to welding significantly effects the process response variables such as force, torque, and strain rate, which in turn effect the weld outcome [97]. It is therefore of paramount importance to analyze such dependent process variables to understand the mechanism of the process.

Information is scarce in literature with regards to evaluating the effect of tool eccentricity on the process response variables, despite its existence in almost all of the FSW processes with varying severity. Yan et al. examined inherent tool eccentricity using a high resolution linear variable displacement transducer (LVDT) and reported that the eccentricity (tool runout) was decreased from 0.03 mm before welding process to 0.015 mm during the welding process [60]. Another inherent eccentricity study (up to 0.03 mm) conducted by Zaeh et al. concluded that tool eccentricity has a major influence in amplifying the oscillations of the process force ( $F_x$  and  $F_y$ ) amplitudes, but can be neglected for extremely low values of 0.001 mm [61].

In addition, work was conducted by Gerken et al. to relate the multiaxial force interaction at each tool rotation to the material extrusion mechanism using a high-speed camera setup at up to a 5 kHz sampling rate [215]. They reported fluctuations on the observed in-plane forces and forge force ( $F_z$ ) with opposing maximum and minimum synchronization and attributed this to slight tool eccentricity during the welding process, though the eccentricity value was not measured.

Due to the complex material flow in FSW, the strain and strain rate also remain an intriguing discussion among researchers, particularly since empirical characterization of these material parameters directly affect the recrystallization and recovery during the cooling period and resulting final microstructure [188], [216]. Thus, efforts have been made to correlate the grain size

and temperature measurements within the stir zone during welding, and accelerate the cooling conditions to suppress recovering and grain growth in order to arrive at an estimate of the strain rate during processing based on the relationship between the Zener-Hollomon parameter ( $Z$ ) and recrystallized grain size ( $d$ ) [110], [217]. Reliable strain rate values can be approximated using the Zener-Hollomon relationship if local peak temperature and average grain size can be obtained accurately [110]. In this study, the Zener-Hollomon parameter ( $Z$ ) for aluminum alloys [218] is utilized to deduce the strain rate,  $\dot{\epsilon}$  ( $s^{-1}$ ) of the stir zone through its relationship with the subgrain size,  $w$  (in  $\mu m$ ), i.e.:

$$w = [-0.6 + 0.08 \log Z]^{-1} \quad (\text{Eq.6-1})$$

where

$$Z = \dot{\epsilon} \exp\left(\frac{18772}{T_p}\right) \quad (\text{Eq.6-2})$$

and  $T_p$  is the peak temperature (in Kelvin) attained during FSW [210].

Since static recrystallization occurs along with dynamic recrystallization once the tool traverses a particular plane, a degree of grain growth can be expected during the cooling cycle and should also be considered [97], [216]. Therefore, to obtain more accurate estimates of the strain rate, several works by others employed two methods to retain the as-deformed microstructure without the effects of grain growth, recovery and recrystallization during the cooling period [97], [216]. The first one is the ‘stop-action’ technique [219], i.e. rapidly stopping the tool rotational and translational motion during FSW [187], [216], [220]–[222]. In some cases, the tool pin was slightly modified to intentionally break when the rotation was suddenly accelerated, effectively embedding the pin in the workpiece and preserving the material flow at the periphery of the tool pin [103]. Another equally important approach is the subsequent quenching, i.e. rapidly quenching the processed region, usually by cryogenic solutions, in order to suppress further microstructural transformation [220].

In light of the analysis on process response variables mentioned earlier, to the best of the authors’ knowledge, no force and torque measurements have been reported for artificial tool eccentricity, i.e. FSW process using tool eccentricity of  $\geq 0.1$  mm [57]. Therefore in this study, the response variables measured during FSW of AA6061 alloy, namely the  $x$ -axis,  $y$ -axis, and  $z$ -axis forces, spindle torque, and power were analyzed to elucidate the effects of tool eccentricity on the welding process. In addition, thermal history of the stir zone was examined to correlate heat

generation to the resulting multi-axial forces and torque. Finally, the influence of tool alignment on strain rate was evaluated using the cryogenic quenching method to preserve the microstructures during deformation with better fidelity.

## 6.2 Methodology

### 6.2.1 Force and torque analysis

As shown in Figure 6-1, the tool consists of two components, namely the tool sleeve (Figure 6-1(a)) which is connected to the tool holder, and the pin insert (Figure 6-1(b)), which is fixed inside the tool sleeve using a side screw. The outer diameter of the tool sleeve was modified accordingly with an asymmetrical offset of 0.1 mm and 0.2 mm to produce the desired tool eccentric motion of 0.2 mm and 0.4 mm, respectively, once the tool sleeve is fixed on the tool holder. The tolerance for both of the fabricated offset is  $\pm 0.025$  mm.

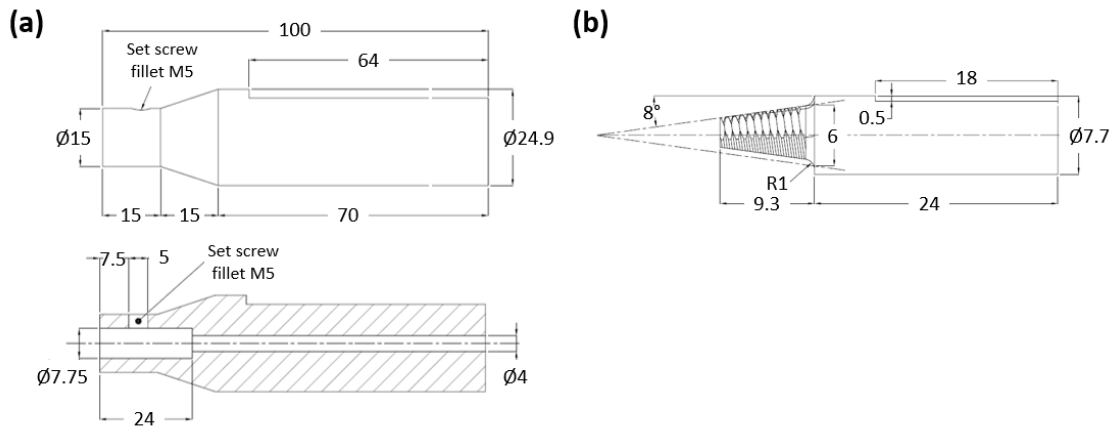


Figure 6-1. Design of the (a) tool sleeve and (b) pin insert. Dimensions are in millimeters.

A displacement-controlled friction stir welding method was used while force and torque measurements were analyzed through the built-in capability of the MTI gantry FSW machine available in the Centre de Soudage par Friction Malaxage (CSFM), at Université du Québec à Chicoutimi (UQAC) in Chicoutimi, Quebec, Canada. The sampling rate for the force and torque output was 27 Hz. The designations for the varying tool setup and weld speed conditions shown in



Table 6-1 will be used throughout in the following sections. Each set off conditions was repeated three times to obtain averages and ranges of the measured values.

Table 6-1. Designation of samples with varying tool setup and weld speed.

Tool setup	Weld speed (mm/min)			
	45	63	90	125
Aligned	A-45	A-63	A-90	A-125
0.2 mm eccentricity	0.2-45	0.2-63	0.2-63	0.2-125
0.4 mm eccentricity	0.4-45	0.2-63	0.2-63	0.4-125

## 6.2.2 Strain rate analysis

A separate set of experiments were required to observe the microstructural evolution and strain rate of the same alloy through cryogenic rapid quenching. Bead-on-plate welds were made parallel to the rolling direction (RD) using the typical tool design. Due to limitations, only three specimens were prepared for this experiment, as tabulated in Table 6-2.

Table 6-2. Designation of specimens for strain rate analysis.

Tool setup	Rotational speed (rpm)	
	710	1120
Aligned	A-710	A-1120
0.4 mm eccentricity	-	E-1120

To inhibit grain growth and morphological changes associated with the cooling period, a cryogenic rapid quenching process was devised using a mixture of ethylene glycol and purified water to provide a subzero freezing point. This solution can reach a minimum freezing point of approximately  $-50\text{ }^{\circ}\text{C}$  with a 55% water mixture [223]. Liquid nitrogen was incrementally poured into the ethylene glycol +  $\text{H}_2\text{O}$  liquid mixture until a cryogenic temperature of approximately  $-40\text{ }^{\circ}\text{C}$  was achieved, where the mixture begins to solidify. Then, as it begins to melt, the mixture was used to quench the welds. The mixture is poured on the workpiece immediately after the tool traverse motion is stopped and subsequently pulled out from the thick plate. This method can

provide a more rapid quench compared to using liquid nitrogen since nitrogen forms a thin vapour layer once in contact with the workpiece, which insulates it and lowers the cooling rate.

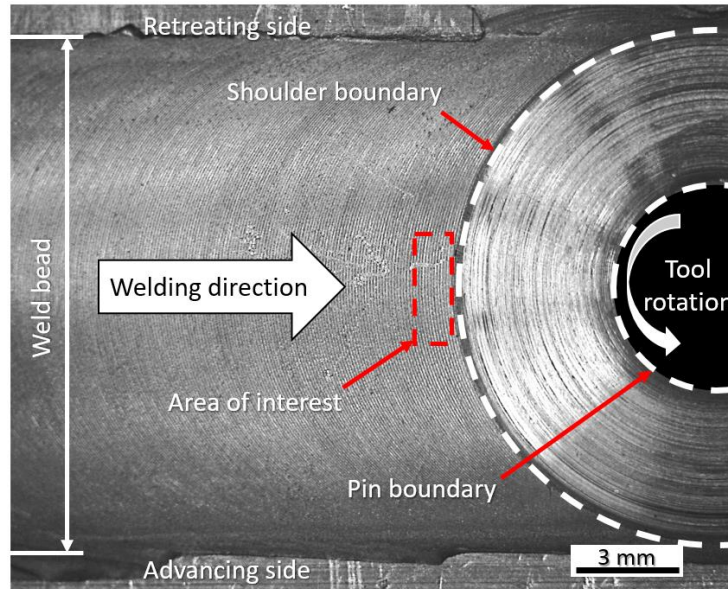


Figure 6-2. Extracted area for EBSD analysis.

Samples for high-resolution electron backscatter diffraction (EBSD) analysis were extracted from the top plane of the stir zone (SZ), immediately behind the final shoulder area, as shown in Figure 6-2. The motivation behind the selection of the area is due to several reasons. Firstly, Suhuddin et al. reported that the extruded material behind the pin underwent additional deformation induced by the shoulder [224]. Hence, analyzing the area just outside this region would be more viable since a more mechanically stable SZ microstructure can be expected. In addition, thermally activated grain morphology during cooling period can be inhibited through rapid quenching by constantly pouring the cryogenic mixture. Moreover, it is possible to monitor the top surface's temperature using a contact-based thermometer to ensure cryogenic conditions are maintained throughout the cooling period.

Other than the setup mentioned in this section, the experimental methods for the thermal cycle measurements, high speed camera observations and metallurgical characterization can be referred to in Chapter 3.

## 6.3 Results

### 6.3.1 Force and torque measurements

The tri-axial forces ( $F_x$ ,  $F_y$ ,  $F_z$ ) and torque ( $M_z$ ) temporal variations throughout the whole welding process for the three eccentricity conditions are presented in Figure 6-3. The weld forward travel speed for all tool setup conditions is 63 mm/min. The variations generally follow similar patterns during the six stages in all setup conditions.

In Stage 1, no values were recorded except for the obvious sharp peak of torque to initiate spindle rotation. Once the pin slowly plunges and makes contact with the workpiece (Stage 2),  $F_z$  increases followed by a slight decrease when heat generation increases, which further softens the material directly under the pin tip. Meanwhile,  $M_z$  steadily increases since more surface area of the pin is in contact with the workpiece. Stage 3 corresponds to the shoulder contact during the plunge stage where  $F_z$  and  $M_z$  peak with an abrupt increase in tool-workpiece contact. Both process variables decrease and stabilize during the 5 s dwelling period (Stage 4) once the heat generation is sufficient to plastically deform the workpiece with minimal forge force and torque.

The tool is finally traversed linearly in Stage 5, which abruptly increases  $F_x$  and  $F_y$  simultaneously, and eventually stabilizing all the tri-axial forces and torque within a short period of time. Note that the longitudinal force exhibits a negative value due to the opposite direction (backward) resistance from the workpiece. All values drop to zero once the tool is finally pulled out of the workpiece (Stage 6).

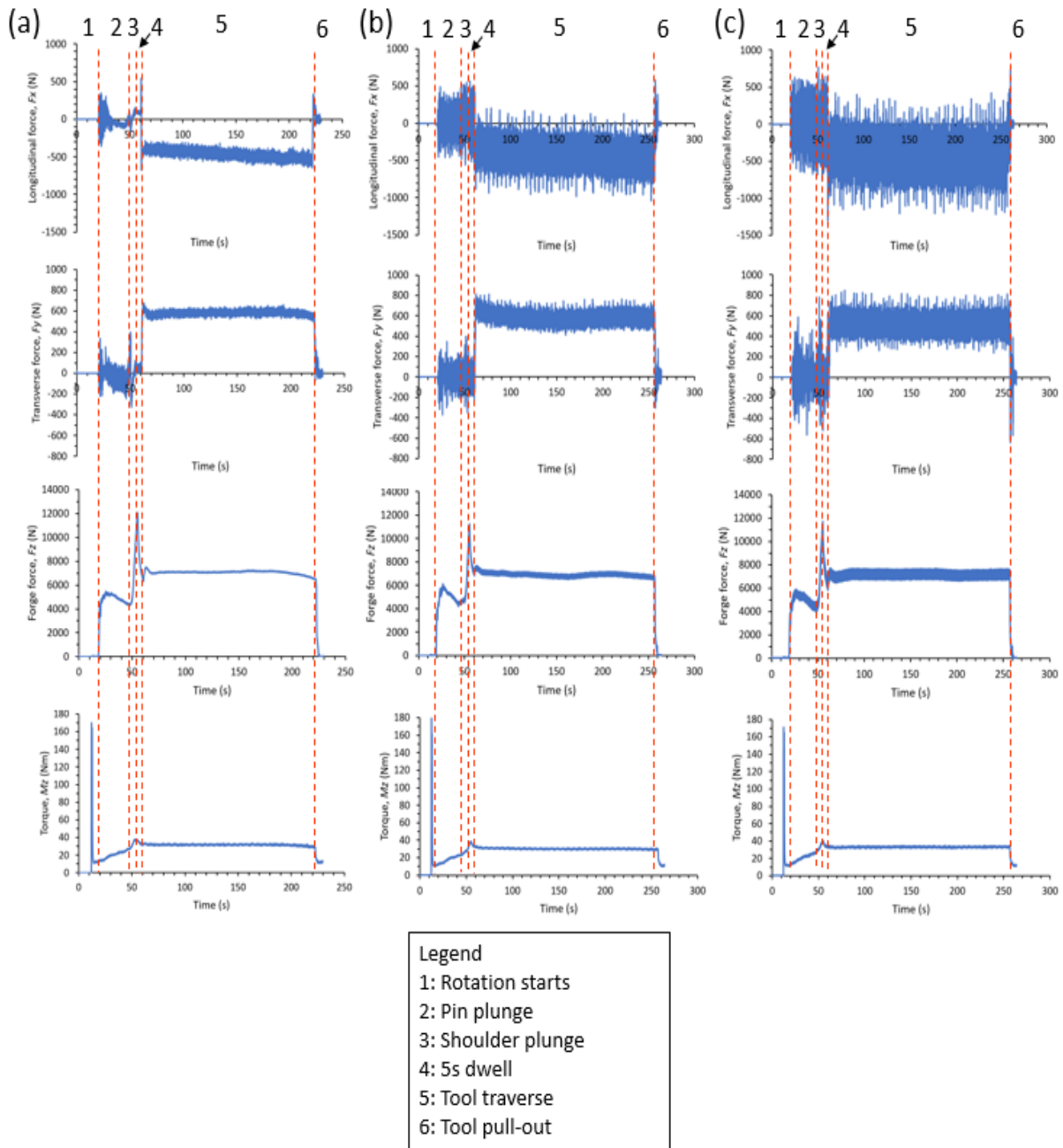


Figure 6-3. The forces ( $F_x$ ,  $F_y$ ,  $F_z$ ) and torque ( $M_z$ ) history throughout the whole welding process for (a) A-63 (b) 0.2-63 and (c) 0.4-63 samples.

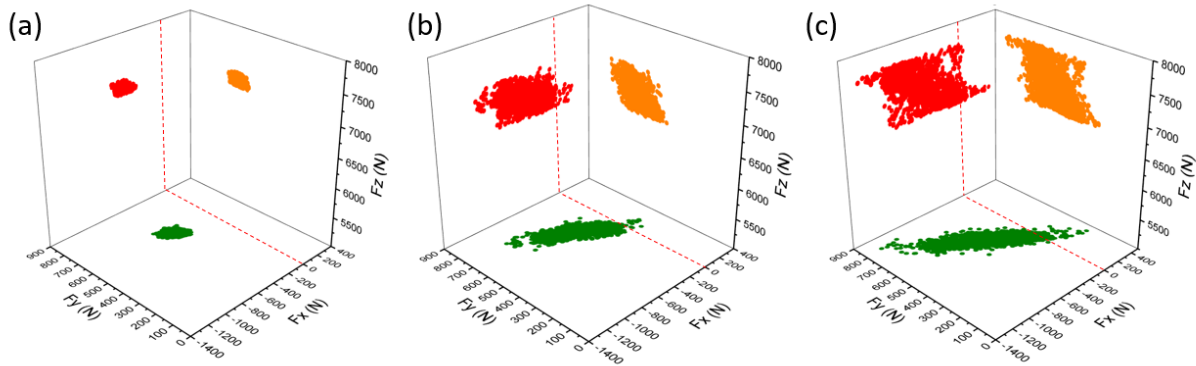


Figure 6-4. 3D plots showing relationships between the longitudinal ( $F_x$ ), traverse ( $F_y$ ) and forge ( $F_z$ ) forces for (a) A-63, (b) 0.2-63 and (c) 0.4-63 under steady state welding. The red dashed lines separate the positive and negative values recorded for  $F_x$ .

While these observations hold true for all the conditions mentioned in

Table 6-1, a glaring difference is observed in the fluctuations of the tri-axial forces values throughout the welding process when the tool eccentricity is increased up to 0.4 mm. Interestingly, both cases of 0.2 mm and 0.4 mm eccentricity setup occasionally also show positive values for the longitudinal force. These observations are further evident when examining the 3D plots showing the relationships between the tri-axial forces during steady state (traverse motion) (Stage 5) in Figure 6-4. A-63 data shows a narrow clustering of all forces (Figure 6-4(a)), with increasing scatter in the data when eccentricity increases from 0.2 mm (Figure 6-4(b)) to 0.4 mm (Figure 6-4(c)). From the scatter plot of 0.4-63 (Figure 6-4(c)), it can also be generalized that the tri-axial forces simultaneously reach a maximum and minimum but with a varying degree of concentration.

To further examine this, the individual normalized values of the torque and tri-axial forces were plotted during the steady state period for weld 0.4-63 during an arbitrary 3 s period, as depicted in Figure 6-5. Torque values exhibit an erratic oscillation, and do not show any similarities compared to the tri-axial forces throughout the steady state. However, the data also shows that the peaks and valleys of the tri-axial forces generally match each other as shown by the dashed lines, i.e. a larger  $F_x$  value signifies a larger  $F_y$  and  $F_z$  value, and likewise a smaller  $F_x$  coincides with lower values of  $F_y$  and  $F_z$ , as can also be seen in Figure 6-4(c). Note that, while the normalized values in Figure 6-5 show the forge force variance to be relatively small, the absolute value for the  $F_z$  is in fact the largest force imposed on the tool by one order of magnitude larger than the longitudinal and transverse forces. These results are slightly different from the results

reported by Gerken et al.[215], where maximum in-plane forces were observed during the minimum  $F_z$ , and minimum in-plane forces were recorded with a maximum forge force  $F_z$ .

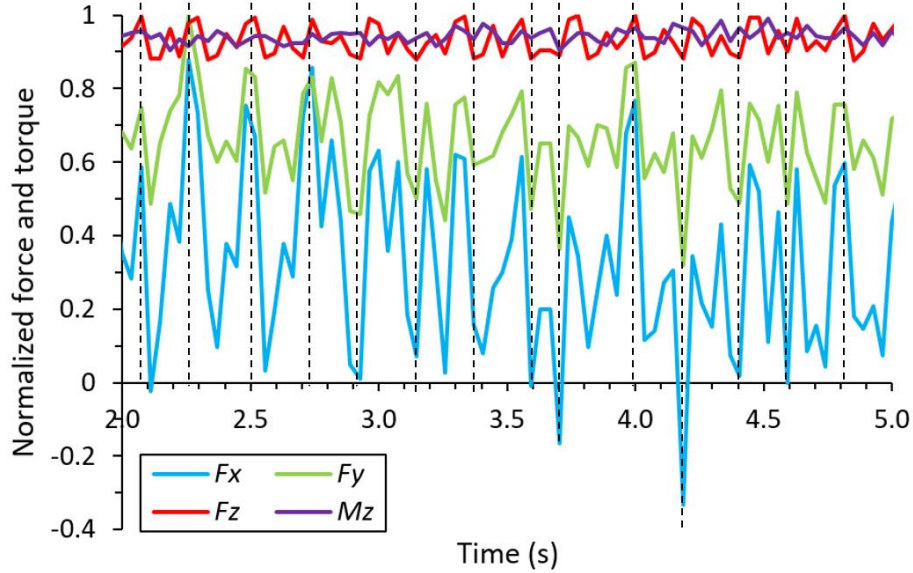


Figure 6-5. Normalized values of the torque and tri-axial forces during steady state for 0.4-63 sample.

Figure 6-6 depicts the average force, torque and power absolute values in steady state (Stage 5) as a function of weld speed under different tool setup conditions. The root mean squared method was utilized to take into account the sinusoidal fluctuation in the measurements. Power,  $P$  ( $\text{Nms}^{-1}$ ) was calculated as follows:

$$P = (\bar{X}_{F_x} \cdot \bar{X}_{v_x}) + (\bar{X}_{M_z} \cdot \bar{X}_{\omega}) \quad (\text{Eq.6-3})$$

where  $\bar{X}_{F_x}$  is the average longitudinal force (N),  $\bar{X}_{v_x}$  is the average instantaneous velocity ( $\text{ms}^{-1}$ ),  $\bar{X}_{M_z}$  is the average spindle torque (Nm) and  $\bar{X}_{\omega}$  is the average rotational speed ( $\text{rads}^{-1}$ ). All The power components resulting from the transverse force,  $F_y$ , and forge force,  $F_z$ , were not included since the instantaneous velocities for both cases were not recorded and are also expected to be negligible.

In general, all samples show an increase in the tri-axial forces as well as a slight increase in torque as the weld speed increases from 45 mm/min to 125 mm/min, with the forge force ( $F_z$ ) showing the greatest increase. Similarly, the weld power (Figure 6-6(e)) exhibits an increasing trend for all tool setup conditions with increasing weld speed. This agrees well with earlier works,

which suggests that more material is processed per unit time at higher weld speed [225]–[227]. By dividing power with the weld speed (converted to mm/s), the specific weld energy (kJ/mm) can be calculated. The specific weld energy obtained for this study is within the range of 2.40 kJ/mm to 4.07 kJ/mm.

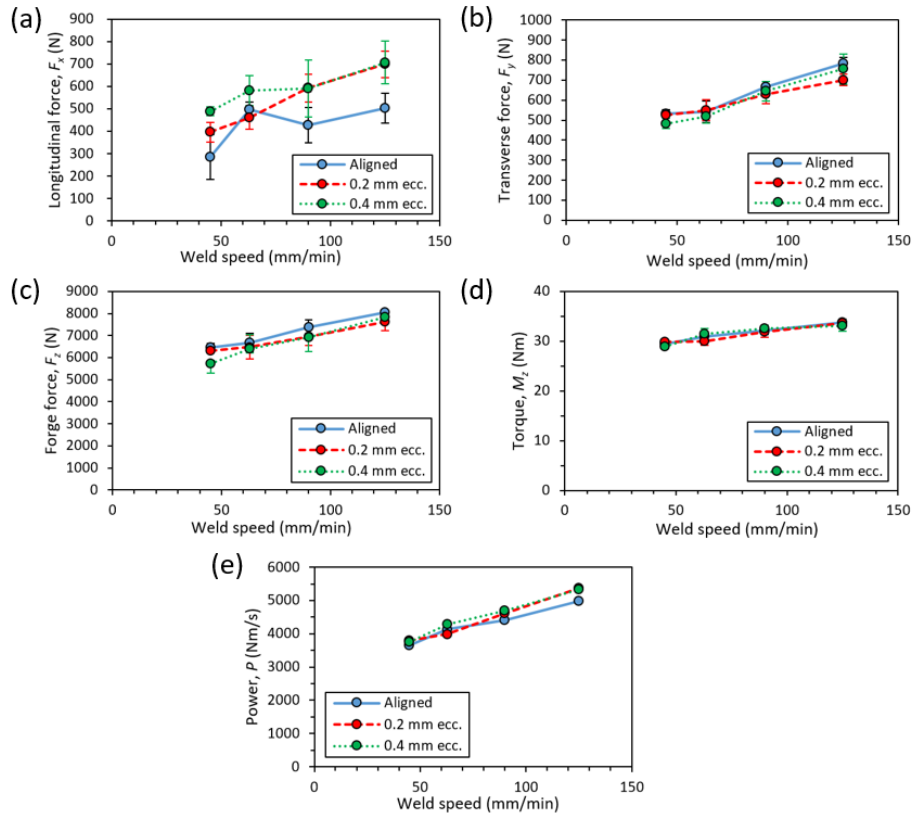


Figure 6-6. Force, torque and power average absolute values in steady state as a function of weld speed under different tool setup conditions: (a) Longitudinal force,  $F_x$ , (b) Transverse force,  $F_y$ , (c) Forge force,  $F_z$ , (d) Torque,  $M_z$  and (e) Power,  $P$ .

In addition, both the tools with eccentricity of 0.2 mm and 0.4 mm have shown higher longitudinal force compared to the aligned tool setup. This can be attributed to the increased in tool travel distance in each rotation when eccentricity is observed [101], which suggests more tool-workpiece interaction volume, hence more force is required per rotation. Because of this, power for the eccentric setups show noticeable deviation from aligned values with increasing weld speed since more work is needed to process more material volume per rotation. However,  $F_y$  and  $F_z$  values for the eccentric setups seems to indicate similarities with the aligned setup based on the overlap shown in the graphs.

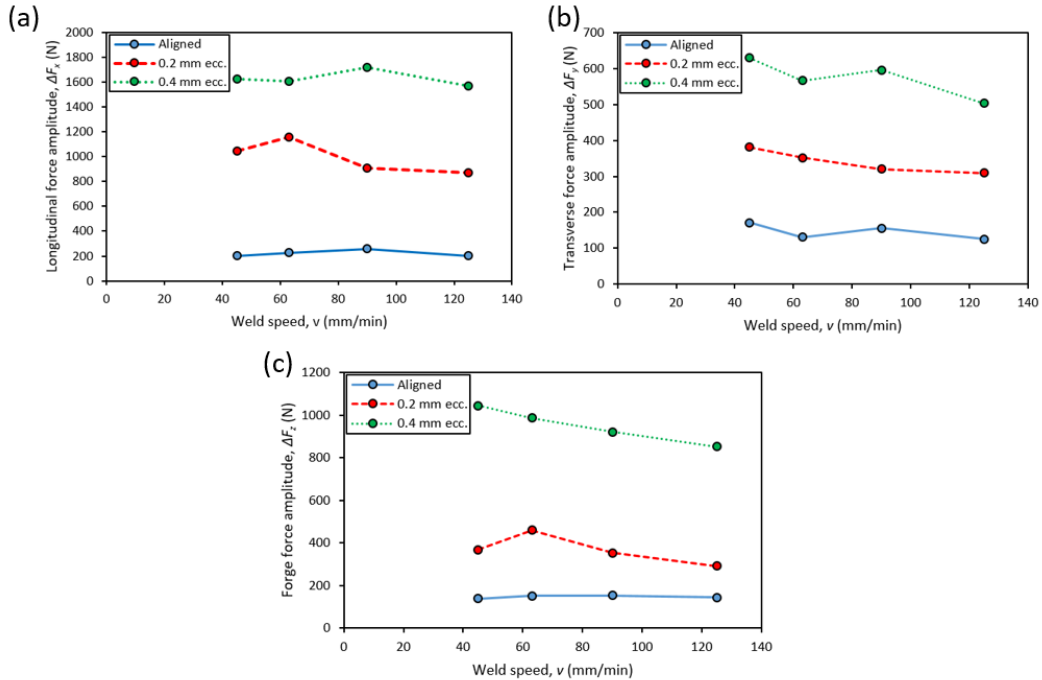


Figure 6-7. Tri-axial forces maximum oscillation amplitude during steady state.

The maximum oscillation amplitudes of the tri-axial forces during steady state are shown in Figure 6-7. The amplitude values are lowest in all aligned tool setup conditions but increase with eccentricity, and gradually peak at maximum eccentricity. In addition, the weld speed seems to have a minimal impact on these values.

### 6.3.2 High-speed camera observations

To ensure the validity of the values measured through high-speed camera (HSC) images, the tool was jogged (free rotation) at 56 rpm and the eccentricity was measured using a dial gauge with tolerance of  $\pm 0.013$  mm (0.0005 in). The tool was then jogged with 1120 rpm (actual rotational speed used) while the motion was captured using the camera and subsequently compared. Table 6-3 demonstrates that the values measured using the dial gauge and camera are in very good agreement, and therefore the HSC method can reliably measure the eccentricity during the welding process.

The comparison between the eccentricity change between the MTI gantry FSW machine in UQAC and the Jafo universal milling machine available in University of Waterloo is shown in Figure 6-8. Note that in the jog stage, the MTI gantry FSW machine eccentricity values are slightly



larger for the eccentric setups compared to the intended values due to the tolerance of the tool sleeve design. Moreover, in both machines, the A-63 samples also showed eccentricity values < 0.05 mm, which is typical of any milling system [57].

Table 6-3. Eccentricity measurements using dial gauge (at 56 rpm) and camera (at 1120 rpm).

Eccentricity (mm)	Dial gauge values <sup>a</sup> (mm)	Camera values (mm)
0 (aligned setup)	0.046 ± 0.013	0.046 ± 0.008
0.2	0.234 ± 0.013	0.257 ± 0.006
0.4	0.381 ± 0.013	0.406 ± 0.015

<sup>a</sup> Values were converted from inches

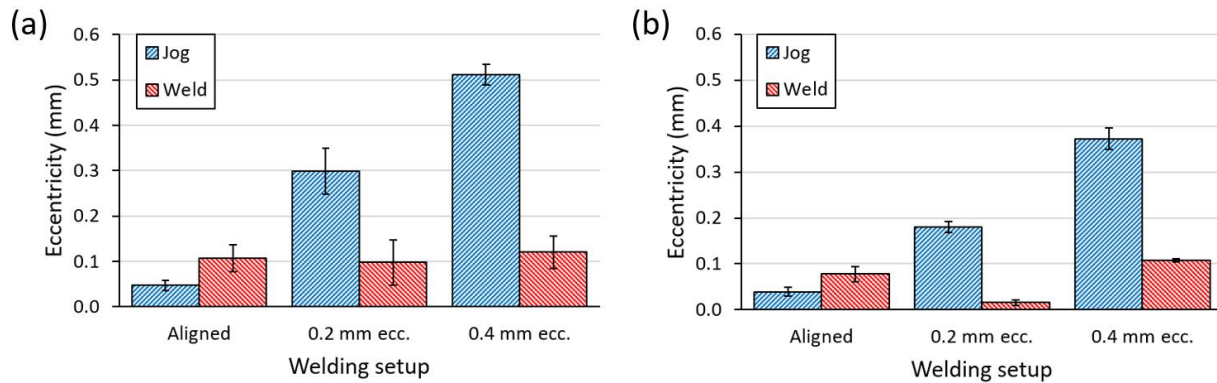


Figure 6-8. Eccentricity comparison during jog and welding process with various eccentricity setup under 63 mm/min weld speed for (a) MTI gantry FSW machine and (b) Jafo universal milling machine.

Table 6-4. Percentage change in eccentricity between jog and weld.

Machine	Aligned	0.2 mm eccentricity	0.4 mm eccentricity
MTI gantry FSW	130%	-67%	-77%
Jafo	100%	-91%	-71%

Figure 6-8 demonstrates that, during the welding process, A-63 samples recorded an increase in eccentricity values. This is in contrast with both eccentric setup conditions, where a significant decrease in eccentricity was measured during the actual FSW process when the tool is

within the material. The percentage change of increase (positive) and decrease (negative) in eccentricity is summarized in Table 6-4.

### 6.3.3 Temperature measurements

The thermal history of the tool shoulder for A-63 sample is shown in Figure 6-9. The temperature rapidly peaks to the melting solidus temperature of AA6061 ( $T_m = 582\text{ °C}$ ) [181] in the plunging period, followed by a slight drop during the 5 s dwell time and stabilizing at a temperature slightly under  $T_m$  during the traverse period, until finally decreasing abruptly during tool pull out period and gradually cooling to ambient temperature.

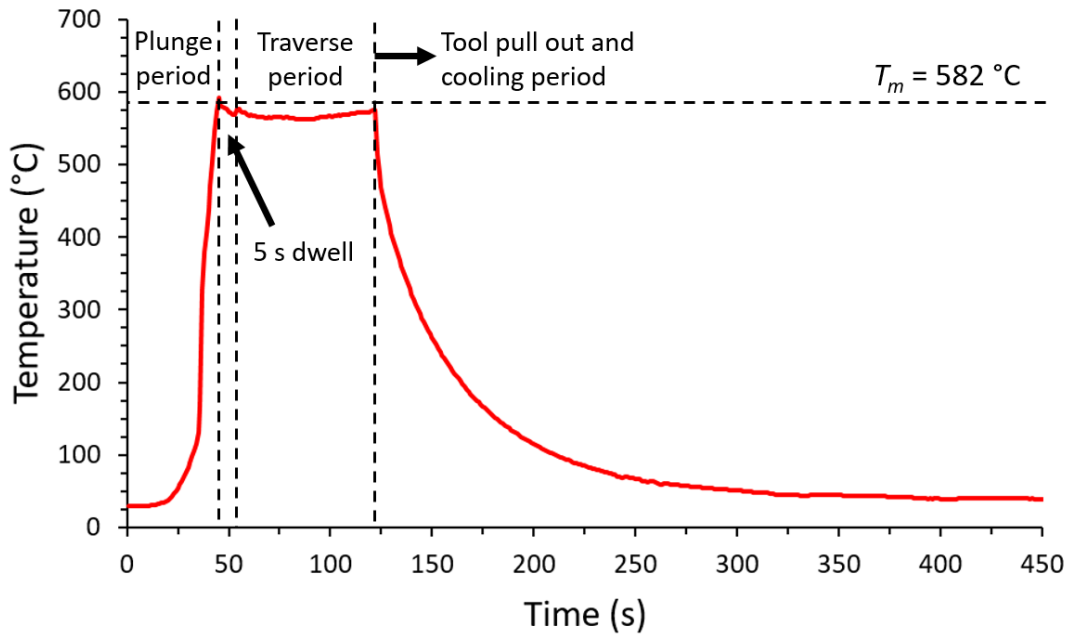


Figure 6-9. Thermal history during FSW with A-63 setup.

Figure 6-10 depicts the tool shoulder average peak temperature during steady state with varying weld speed for the A-1120 setup (Figure 6-10(a)) and varying rotational speed for the A-63 setup (Figure 6-10(b)). In both cases, the values obtained for the eccentric setups were deemed inconsistent, possibly due to the immense fluctuating tri-axial forces during the welding stage. The data shown in Figure 6-10(a) indicate that all values are in the range of  $0.98T_m$  to  $1.00T_m$ , with the largest difference of  $\Delta T_m = 18\text{ °C}$ . At higher weld speeds, the temperature approaches the solidus temperature while the error bars (based on three trials per weld speed) also become larger. This suggests that the weld speed shows minimal impact on the steady state peak temperatures, despite

an increase in the rate of advancement per revolution (APR, i.e. weld speed/rotational speed) from 0.04 mm/rev to 0.11 mm/rev. Note that, due to limitations, the force and torque measurements were conducted under constant rotational speed of 1120 rpm only, and therefore only Figure 6-10(a) is discussed with regards to force and torque measurements.

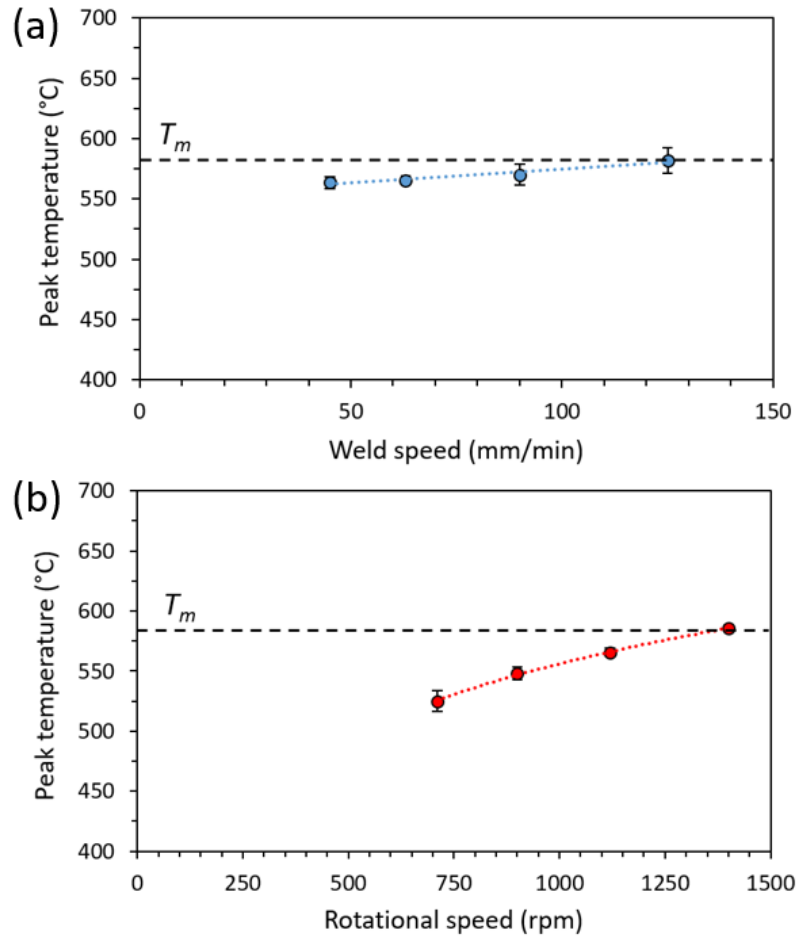


Figure 6-10. Tool shoulder average peak temperature measured during steady state of aligned setup with (a) varying weld speed and (b) varying rotational speed.

On the other hand, Figure 6-10(b) depicts the average peak temperature during traverse period of the aligned samples as a function of rotational speed. Peak temperature showed an increasing trend as rotational speed is increased, but reaches maximum value at approximately the solidus temperature of AA6061. All values are in the range of  $0.93T_m$  to  $1.00T_m$ , with the largest difference of  $\Delta T_m = 61$  °C. These values are particularly important when discussing the strain rate results, particularly for the peak temperature for 710 rpm (A-710) and 1120 rpm (A-1120). While relatively similar heating rate from the thermal history (not shown) was observed for both samples,

the peak temperature observed in the A-1120 sample is higher (566 °C) compared to the A-710 sample (525 °C), stabilizing just below the solidus temperature of the alloy ( $T_m = 582$  °C).

As mentioned earlier, inconsistencies and instability of the thermal history were recorded for the 0.4 mm eccentric setup, likely due to the rigorous vibration on the system induced by the tool's eccentric motion [228], making all the measured peak values to be higher than the base metals solidus temperature, ranging from 600 °C to 626 °C with no observable trend. It is speculated that the addition of eccentricity may cause an increase in heating rate and possibly higher peak temperature. However, due to the self-regulated 'slip-stick' mechanism, which will be discussed in detail in the discussion section [202], the peak temperature for A-1120 has shown to stabilize just below the solidus temperature, which is already close to the maximum value. Therefore, it can be safely approximated that the 0.4 mm eccentric setup (E-1120) will produce a similar peak temperature to the aligned tool setup.

### 6.3.4 Strain rate and texture analysis

Figure 6-11 presents the inverse pole figure (IPF) maps for all three samples. The high angle boundaries ( $> 15^\circ$ ) are shown as black lines, while the white dashed lines represent the boundary between bands of grains that formed in layers that were spaced at a distance equal to the APR, i.e. 0.089 mm/rev for A-710 and 0.056 mm/rev for both A-1120 and E-1120, respectively. The welding direction is upwards. The white lines are inclined at an angle since the observed area is slightly deviated from the stir zone centre and towards the retreating side of the stir zone.

In general, the IPF maps show the formation of equiaxed grains on the top surface of the stir zone. Furthermore, with similar tool setup, the A-710 specimen exhibits finer grains compared to the A-1120 sample. Interestingly, when the rotational speed is fixed, the weld made with the eccentric tool, specimen E-1120, has a much finer grains as compared to A-1120 and A-710. This seems to indicate that eccentricity significantly enhances shearing activity in the stir zone, refining grains into much smaller sizes.

The subgrain size, peak temperature and calculated strain rate of samples are shown in Table 6-5. The grain sizes were measured using the ASTM E112-13 linear intercept method. Note that due to the very fine nature of E-1120 grains obtained in this study, only HAGBs were considered for the subgrain sizes of samples. The strain rates were then calculated using Equation 6-1 and 6-2. The calculated strain rates show values with differences in one or two orders

of magnitude between each other. The strain rate range is between  $0.17 \text{ s}^{-1}$  to  $51.94 \text{ s}^{-1}$ , where the A-1120 sample show the lowest strain rate. In contrast, the value increased significantly by two orders of magnitude higher for the E-1120 sample. This further supports the hypothesis that shearing activity is enhanced using the eccentric tool.

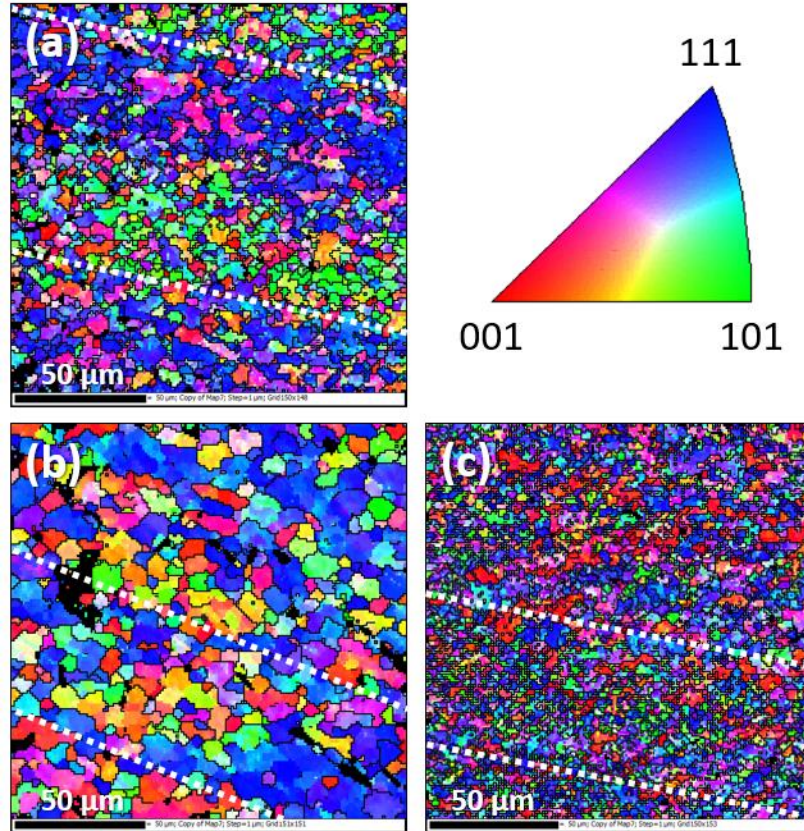


Figure 6-11. IPF maps of (a) A-710, (b) A-1120 and (c) E-1120. The HAGBs are represented by the black lines. Welding direction is upwards.

Table 6-5. Subgrain size, peak temperature and calculated strain rate of samples.

Tool setup	Rotational speed (rpm)	EBSD subgrain size, $w$ ( $\mu\text{m}$ )	Peak temperature, $T_p$ (in Kelvin)	Calculated strain rate, $\dot{\epsilon}$ ( $\text{s}^{-1}$ )
Aligned	710	$4.24 \pm 0.68$	798.15	1.71
	1120	$8.63 \pm 0.88$	839.15	0.17
Eccentric	1120	$3.18 \pm 1.54$	839.15	51.94

Figure 6-12 depicts the pole figures (PFs), inverse pole figures (IPFs), and orientation distribution function (ODF) of all samples based on the area observed in Figure 6-11. Similar to the texture analysis in Chapter 5, the PFs and IPFs are based on the normal direction (ND), rolling direction (RD) which coincides with the welding direction, and transverse direction (TD). Likewise, the plane of reference is indicated by RD-TD plane (top plane), ND-TD plane (front plane, perpendicular to the rolling direction), and RD-ND plane (side plane, parallel to the rolling direction).

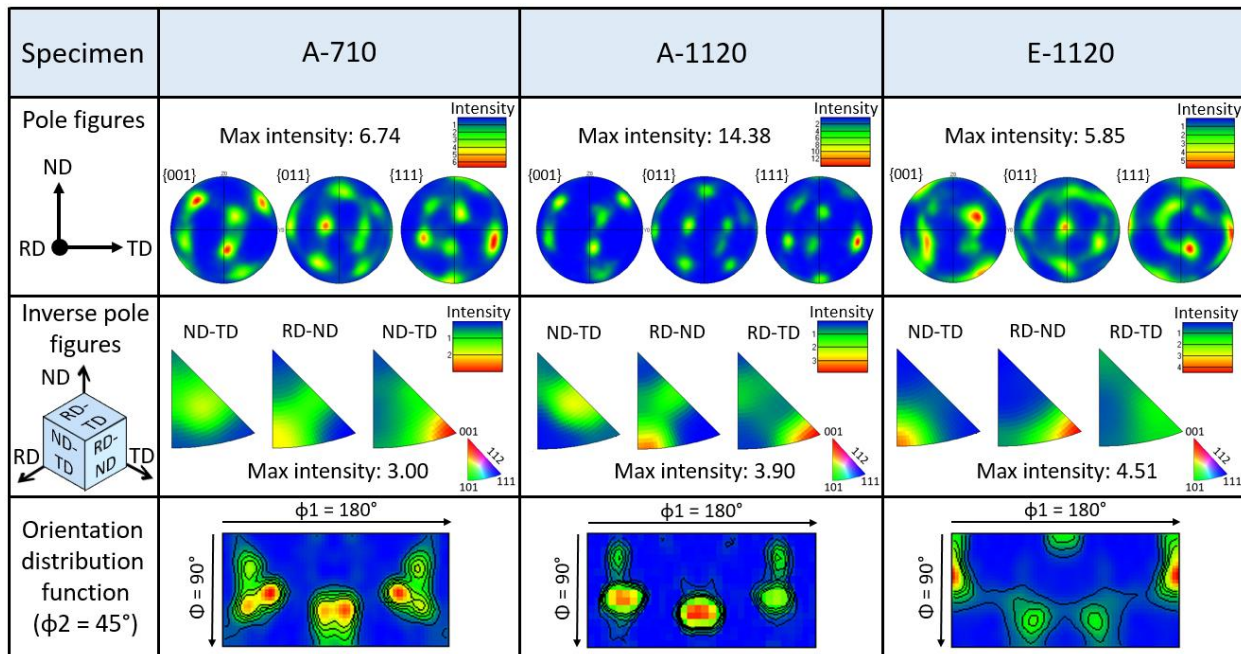


Figure 6-12. PFs, IPFs and ODF of all samples.

The PFs indicate that, as rotational speed increased from 710 rpm to 1120 rpm, the maximum intensity increases while keeping the same texture orientation. However, the intensity decreases when tool eccentricity is employed, indicative of a more random texture. It is known that torsional textures are not preserved when high total strains are applied [229]. In the case of E-1120 sample where the strain rate value is two orders of magnitude larger than A-1120, it is therefore plausible that the texture experienced more intense randomization due to the higher strains and strain rates.

In addition, further differences in texture are observed in the IPFs due to eccentric alignment. To understand this, Figure 6-13 shows a schematic of the preferred plane orientations for A-1120 and E-1120 samples with reference to the shoulder interface. For simplicity of

discussion, the tilt angle is considered to be  $0^\circ$ . The schematic shows the preferred orientation of the  $\{111\}$  planes (blue planes) and  $\{011\}$  planes (green planes) immediately behind the tool shoulder. For A-1120, the  $\{111\}$  plane is roughly parallel to the shoulder surface, which corresponds to the directions with the maximum shear stresses [182]. As a result of this dominant orientation of the shear deformation, the IPFs for A-710 and A-1120 exhibit a maximum intensity of the  $\{111\}$  plane towards the ND (i.e. RD-TD plane), in conjunction with high intensity of the  $\{011\}$  plane being plane normal to the TD (i.e RD-ND plane) (Figure 6-12(a)). Previous works have also reported similar observations with regards to the workpiece-pin interface, where the  $\{111\}$  plane and  $\langle 011 \rangle$  direction are preferentially oriented parallel to the pin surface [117], [182]–[184].

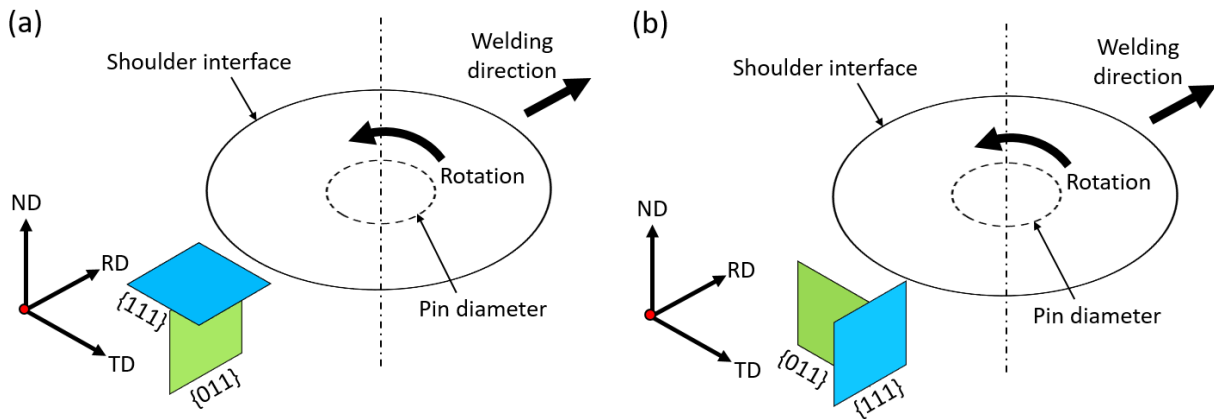


Figure 6-13. Schematic of the preferred  $\{111\}$  and  $\{011\}$  plane orientations at the shoulder interface for (a) A-1120 and (b) E-1120 samples.

However, the IPFs of the E-1120 sample show an approximately  $90^\circ$  shift of the  $\{111\}$  and  $\{011\}$  plane towards the TD (ND-RD plane) and the RD (ND-TD plane), respectively, as shown in Figure 6-13(b). This  $90^\circ$  shift of the  $\{111\}$  plane was also observed in the traverse plane of dissimilar Al alloy welding when tool eccentricity was utilized, as discussed in Chapter 5. It is postulated that the reason for this is due to the more erratic material flow induced by the tool eccentric motion, and suggests that the dominant orientation of shear strains is different for the eccentric tool. Further work such as material flow simulation using numerical modeling may be applied to better explain this phenomenon.

Finally, the ODF based on the Euler angles  $\phi_1$ ,  $\phi_2$  and  $\phi$  (showing the  $\phi_2 = 45^\circ$  section) is also presented in Figure 6-12. Based on works by Hirsch et al.[190], both A-710 sample and A-1120 sample can be identified as having a strong  $\{111\}\langle 11-2 \rangle$  Y texture component. In contrast,

with the eccentric setup, the E-1120 sample show morphological changes towards a strong  $\{112\}\langle 011\rangle$  A texture component. These textures are commonly associated with rolling/deformation processes, suggesting that, in both cases, severe plastic deformation occurred.

## 6.4 Discussion

### 6.4.1 Force evolution in eccentricity setup

Figure 6-3 clearly demonstrates that analyzing the results using only average values such as those in Figure 6-6 is insufficient since the rigorous oscillations caused by tool eccentricity are not observable, which can be misleading. Increase in fluctuation amplitude with increasing eccentricity (Figure 6-7) demonstrates that the tool undergoes cyclic bending for each rotation, which is clearly detrimental to the longevity of the tool [96]. Interestingly, Figure 6-4(b) and Figure 6-4(c) demonstrate sizable  $F_x$  positive values for eccentric samples, suggesting that the tool underwent a forward ‘push’ by the workpiece towards the welding direction, contrary to what might be expected in the FSW process. It is postulated that the eccentric motion of the tool increases the hydrostatic pressure during the deposition stage at the wake of the tool [215], which resists the tool’s backward motion at this instance, thereby recording a positive value. Given that the current setup is incapable of precisely pinpointing the instantaneous position of the tool for each force and torque conditions, future studies will look into synchronizing the camera observations with the process response variables for accurate correlation.

Camera measurements as shown in Figure 6-8 have demonstrated that the aligned samples with  $< 0.05$  mm of inherent eccentricity show an increase in eccentricity during the FSW process for both machines. This is in contrast to previous findings by Yan et al., which suggested that the effect of their initial tool runout of 0.03 mm was suppressed during FSW processing to 0.015 mm [60]. One possible reason for this is due to the 6.4 mm material thickness and 300 rpm rotational speed used in their work, which is significantly lower than this study. This would adversely affect the hydrostatic pressure formed around the tool, which changes the rigidity of the machine and material system. In addition, the reason for the eccentricity increase in this study can be attributed to two factors, namely: the asymmetric tool design and the rigidity of the components of the spindle system.



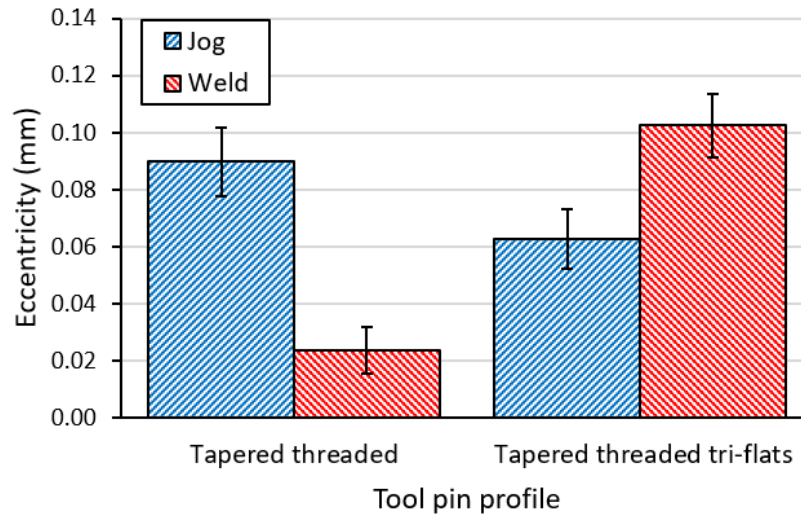


Figure 6-14. Eccentricity change in A-63 setup caused by the difference in tool pin profile.

The tool profile consists of tapered threaded pin with three flats. The design is intended to enhance vertical and rotational material transport as well as enable better material mixing [15], [17], [57], [73], [230]. However, due to the asymmetric nature of the pin, an uneven force distribution in the shear zone surrounding the tool during welding can be expected. Mehta et al. suggested that a triangular pin exerts more transverse force on the pin compared to a cylindrical tool and can be detrimental to the tool's durability [96], [231]. The increase in the horizontal forces may be the reason for the observed increase in eccentricity even in the aligned setups. Figure 6-14 shows eccentricity value change during jog and weld conditions using similar A-63 setup but with different tool pin profile, namely a tapered threaded tool and a tapered threaded tool with tri-flats. Note that the three measurements were taken for both pin design and the decreasing and increasing trend is consistent for both tools, respectively. The former pin design is conical in nature, thus a relatively even force distribution imposed on the pin is expected during welding. As a result, the inherent eccentricity was effectively suppressed to a minimum during the steady state period. In contrast, with the three flats design, while beneficial to the weld outcome, seems to aggravate the eccentricity even with minimal initial eccentricity value.

In addition, the spindle consists of enclosed components such as the shaft, bearings and housing [232], all of which are designed with respective tolerances, which may be subjected to a slight increase due to wear. During the jogging stage, no load is imposed onto the spindle, thus only the inherent eccentricity formed by the tool holder and/or collet was detected. During the welding stage, however, a high load (up to 8 kN) was imposed on to the inner components of the

spindle, which increases the observed eccentricity. Any ‘loose’ component would be subjected to the high load and would be firmly fixed at a certain rotational offset during the process. Therefore, the spindle’s tolerance could have also contributed to this value. Note that the eccentricity increase during the aligned setup for MTI gantry FSW and Jafo machines are 0.061 mm to 0.039 mm, respectively, which is an acceptable tolerance value and to a certain degree a manifestation of a difference in machine rigidity and spindle tolerance in each machine.

Since vibrations of the milling table were observed during the welding process, careful measurements were done to take into account of any effect deriving from the independent oscillation of the camera due to the vibration of the stage. During the steady state of the welding process, the eccentric tool setup samples with  $\geq 0.2$  mm shows a dampening effect on both machines with most of the values decreasing in close proximity to 0.1 mm. With the inherent eccentricity of the aligned tool, asymmetry of tool design and tolerance of the spindle components, the results show that the eccentricity was effectively dampened by the system, but consequently, the tool undergoes larger force fluctuations as the eccentricity becomes larger. This cyclic bending can therefore be potentially detrimental to the tool life, particularly if higher weld speed and lower rotational speed is utilized. The reason for the significant decrease of 0.2 mm tool eccentricity setup during welding in Jafo machine (Figure 6-8(b)) is currently unknown, but it is postulated that the eccentric positioning during tool fixture was opposite to the inherent eccentricity and tolerance of the system, which would significantly mitigate the imposed eccentricity.

## 6.4.2 Correlation between force, torque and temperature

Figure 6-10 suggests that weld speed has minimal impact on the heat generation during steady state despite the increase in power (Figure 6-6(e)), which is in contrast with suggestions from literature [225], [233]. The plausible reason for this is because of precautions taken in selecting the appropriate parameters to account for the thickness of the base metal plates utilized in this work, compared to the thin aluminum sheets ( $\leq 6$  mm) used in most FSW studies. To avoid tool breakage, a 16 mm/min plunge rate and 5 s dwell was used, which facilitates maximum heating rate up to the solidus of AA6061 as shown in Figure 6-9. The temperature is then kept consistent in close proximity to  $T_m$  during the translational motion. Therefore, regardless of the weld speed used, the peak temperature would remain close, since similar rotational speed, plunge rate and dwell time were used in all cases.

Since the peak temperature values are already close to the solidus temperature, local melting of the workpiece would transition the sticking frictional condition of the tool-workpiece interaction to a slipping mechanism. This phenomenon was observed by Gerlich et al. and Yamamoto et al. in friction stir spot welding (FSSW) of Al alloys and Firouzdor et al. in works on Al to Mg FSW [234]–[238]. The decrease in the tool-workpiece coefficient of friction would cause the torque to decrease, cooling the temperature ephemerally until the temperature dips below  $T_m$ . This in turn will transition the slipping condition to sticking condition again, forming a stick-slip oscillation at the interface, as suggested by Schneider et al. [202].

It is thus understandable that despite the severe fluctuations observed in the tri-axial forces for the eccentric setups in Figure 6-3, the torque for all conditions remains relatively similar. This unique self-regulating mechanism ensures that workpiece temperature in the FSW process would inhibit bulk melting and cause other liquid to solid transition issues and defects commonly associated with fusion welding [239]. However, while the thin ‘stick-slip’ layer formed adjacent to the tool stabilizes the torque values, the increase in weld speed results in higher average  $F_x$  values (Figure 6-6(a)), which in turn results in a higher power requirement (Figure 6-6(e)) to process more material in each rotation. This suggests that the thin stick-slip layer stabilizes the shear stress at the tool-workpiece interface, as indicated by the similar torque values, but shows minimal impact on the normal stress. Hence, changes in force values were observed.

Moreover, previous work by Essa et al. reported that the peak temperature measured by an infrared device on the top surfaces of the advancing side for AA1050 and AA5754 alloys show a decrease with increasing pin eccentricity [101]. They attributed this to the higher cooling rate, in which higher heat generation by the 0.8 mm pin eccentricity results in faster cooling. While no reliable measurements were obtained for eccentric tool setups in this work, it can also be inferred that an increase in heat generation is expected with increasing eccentricity, since a larger travel distance of the tool results in more tool-workpiece contact area. However, the aligned tool specimen temperature measurements indicate that the peak temperature is already  $\geq 0.98T_m$ . Therefore, any additional heating would only increase the heating rate but would eventually peak around the solidus temperature, where the stick-slip mechanism will self-regulate the system, as evidenced by the negligible differences in the average torque (Figure 6-6(d)).

The temperature measurements shown in Figure 6-10 include minor error bars, which demonstrate that the experimental setup is repeatable and robust. Such in-situ temperature

measurements have been reported in the literature to obtain actual values of the stir zone thermal history [208], [236], [237], [240]. However, the shortcoming of this method is that such measurements are essentially an average temperature for the whole thermocouple circumferential and translational motion, since the tool is consistently rotating while traversing at the same time. Further validations from simulations could therefore enhance these findings.

### **6.4.3 Correlation between strain rate and rotational speed**

Previous works have reported that higher rotational speeds strongly correlate to higher strain and strain rates [19], [110], [241]. The maximum strain rates reported in literature to date has been summarized by Kumar et al. as shown in Figure 6-15 [19]. In general, the maximum strain rate exhibits an increasing trend with increasing tool rotational speed. However, the calculated strain rates in this study seem to show a decreasing trend with higher rotational speed. The reduced strain rate calculated for the A-1120 specimen compared to that of the A-710 specimen made with a reduced rotation speed is counter-intuitive, and likely indicates that either the actual strains are lower due to local surface melting and tool slippage, or that there was still unsuppressed grain growth on cooling [110].

In addition, Gerlich et al. conducted FSSW strain rate measurements on AA6061 and obtained a maximum peak temperature of 541 °C and strain rate values in the range of 55 – 395 s<sup>-1</sup> [110]. The difference in the strain rate range is likely due to the difference in the method (spot welds versus linear welds), the rotational speed (3000 rpm versus 1120 rpm) as well as the finer grain sizes observed in the base material since it had a reduced thickness (6.3 mm versus 9.5 mm). The highest peak temperature in our strain rate work (566 °C for A-1120) is slightly higher but remains below the solidus temperature of the alloy (582 °C).

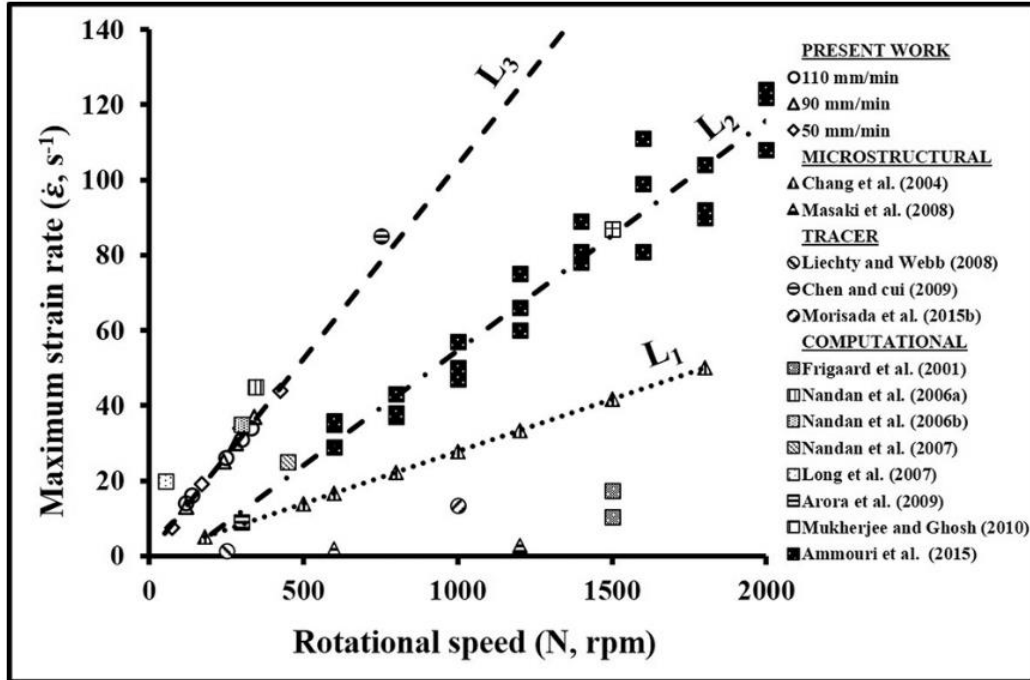


Figure 6-15. Comparison of maximum strain rate available in literature with various welding conditions taken from [19].

## 6.5 Conclusion

Friction stir welding of thick-plate AA6061 aluminum alloy was successfully conducted to observe the effect of tool eccentricity on the process variables. The most important findings are as follows:

### Forces and torque

- Tri-axial forces, torque and power show an increasing trend as weld forward travel speed increases in all tool setup conditions.
- Although eccentricity increases tool tri-axial forces, resulting torque remains similar.
- The eccentricity in the aligned setup increased during welding, while eccentric tool setups show a significant decrease in eccentricity during welding.

### Strain rate

- Peak temperature of the aligned setup increases with increasing rotational speed, but remains below the 582 °C solidus temperature of AA6061.

- Grain refinement of the stir zone is observed for all welding conditions, with the 0.4 mm eccentricity setup having the finest average grain size of 3.18  $\mu\text{m}$ .
- The highest strain rate of 51.94  $\text{s}^{-1}$  was obtained through the eccentric sample with a significant increase of two orders of magnitude higher compared to the aligned tool.
- The IPFs of the E-1120 sample show an approximately 90° shift of the {111} and {110} plane from the generally preferred RD-TD plane and ND-RD plane towards the ND-RD plane and ND-TD plane, respectively.

## **Chapter 7: Conclusion**

### **7.1 Comprehensive summary**

In an attempt to close the loop of this study, the main findings regarding the effects of tool eccentricity on thick plate AA6061 alloy can be concluded with reference to the ‘tetrahedral components’ of materials characterization as introduced in Section 1.3, namely properties, performance, structure, and process.

#### **7.1.1 Properties**

Within the scope of this research, several effects of tool eccentricity can be observed in both the macrostructural and microstructural level, which are linked to the changes in the material’s interaction with the FSW tool. From Section 4.3, there is compelling evidence of higher surface roughness average and roughness depth of the weld bead with increasing eccentricity (Figure 4-3). This is in conjunction with observed enhanced material flow and mixing based on the observations of expanded periodic bands (Figure 4-4). It is postulated that this is mainly due to the increasing inclusions of advancing side material in the stir zone, as discussed in Section 4.4.3. In addition, grain refinement is generally seen in all observed regions when eccentric setup is utilized (Figure 4-6), indicative of enhanced shearing of the stir zone with increasing tool eccentricity (more on this in Section 7.1.4).

Iterations using dissimilar aluminium alloy FSW reveal a similar outcome, where expansions of these periodic bands were clearly observed with increasing tool eccentricity (Figure 5-1 and Table 5-2). Since these bands originated from the advancing side material, it further proves that tool eccentricity accumulates more advancing side material at each rotation, eventually depositing it in the advancing side again in a ‘first-in-last-out’ manner (Figure 5-22). However, in the case of dissimilar alloy FSW, eccentricity seems to limit the intermixing between the alloys, particularly when a higher flow stress material was utilized in the advancing side.

## 7.1.2 Performance

While macrostructural and microstructural changes were observed in the stir zone due to the eccentric setup, the results from this study seem to show minimal effect on the overall mechanical performances. For FSW of AA6061, expansion of the soft region because of larger tool eccentricity does correlate well with the enlargement of the periodic bands in the stir zone (Figure 4-10). This was also observed in the dissimilar FSW of AA5052-AA6061, particularly in the heat-treatable AA6061 side.

The results presented in Figure 5-8 have shown a general increase in ultimate tensile strength and elongation for all dissimilar welding setup in comparison with similar AA6061 FSW joints, largely due to the Portevin Le Chatelier (PLC) effect as observed in Figure 5-9. However, no apparent trend can be seen in the mechanical performance when the tool eccentricity was increased up to 0.4 mm (Figure 5-8). This is largely due to the properly welded tensile samples fracturing mainly in the HAZ of AA6061 and not in the stir zone where microstructural changes occurred.

Even so, special care should be taken in fabricating the weld joint to avoid the presence of a kissing bond defect. Such defect as small as 0.2 mm could potentially change the local strain build-up location and crack propagation path to be inside the stir zone due to the expansion of the ‘soft zone’ at the lower half of the stir zone, as mentioned earlier. This would detrimentally effect the joint strength and fatigue life.

## 7.1.3 Structure

Further microstructural characterization of the stir zone resulted in several interesting observations as a result of tool eccentricity setup in similar AA6061 FSW. In particular, TEM analysis reveals a high density of platelet-shaped precipitates in the bottom region of both aligned and 0.2 mm setups (Figure 4-7), which can be associated to the decrease in the hardness of this region mentioned in Section 7.1.2. However, high dislocation density with overgrown  $\beta''$  precipitates were observed in the inner band region of the 0.2 mm eccentric sample, in contrast to the low dislocation density and dissolved strengthening precipitates observed in the aligned sample (Figure 4-9). Interestingly, this microstructural evolution showed negligible influence on the local hardness, since in both samples, the local softening in these regions are comparable (Figure 4-10).



Texture analysis in similar FSW have suggested that the preferred texture orientation of the  $\{111\}$  and  $\{011\}$  planes evolved when eccentric setup was applied. The top surface IPFs of 0.4 eccentric sample (E-1120) showed an approximately  $90^\circ$  shift of the  $\{111\}$  and  $\{110\}$  plane from the generally preferred RD-TD plane and ND-RD plane towards the ND-RD plane and ND-TD plane, respectively (Figure 6-12). In addition, aligned samples have a strong  $\{111\}\langle 11-2 \rangle$  Y rolling texture component, while the eccentric sample show morphological changes towards a strong  $\{112\}\langle 110 \rangle$  A rolling texture component, both suggesting occurrence of severe plastic deformation. It is postulated that the eccentric tool slightly altered the material flow of the plastically deformed material, but, as stated earlier, does not impose a significant effect on the general mechanical and physical properties.

On the other hand, such a  $90^\circ$  textural shift was also observed in the transverse plane of both aligned and eccentric setup dissimilar welded samples (Figure 5-19 and Figure 5-20). A strong  $\{111\}$  texture parallel to the RD-TD plane was observed for both samples, as opposed to the typical orientation preference to the ND-TD plane, which is roughly parallel to the shear plane of the tool pin. In addition, all stir zone regions for both specimens consistently show a strong rotated W  $\{100\}\langle 1-10 \rangle$  rolling/deformation texture component. It can be concluded that, in the case of dissimilar welding, the effect of tool eccentricity on the texture evolution is negligible.

#### **7.1.4 Process**

Process response variables, particularly force and strain rate, have shown to be the most affected by eccentric setup. Fluctuations of tri-axial forces can be observed when larger eccentricity is imposed on the tool (Figure 6-3). These fluctuations compliment very well the proposed kinematics in Section 4.4.3, where larger negative linear velocity (tool backward movement) can be expected with larger eccentricity setup.

In addition, the calculated strain rates was between  $0.17$  to  $51.94 \text{ s}^{-1}$  (Table 6-5), where the 0.4 mm eccentric sample (E-1120) show a significant increase of two orders of magnitude higher compared to its aligned sample (A-1120) counterpart. Since the maximum oscillation amplitude of the tri-axial forces and the strain rate measured increased with increasing eccentricity, it can be understood that unnecessary additional normal stress and shear stress are imposed on the tool, which may be detrimental to the tool life.

Interestingly, torque values remain similar for all aligned and eccentric conditions within the limited welding parameters tested. This was postulated to be due to the self-regulating stick-slip mechanism during FSW due to local melting (Section 6.4.2). The tool shoulder temperature measurements have shown peak temperatures to be in very close proximity to the solidus temperature of AA6061 for the range of parameters where torque measurements were also conducted, suggesting the occurrence of this mechanism (Figure 6-10).

Another notable observation was the ‘dampening effect’ during the welding process (Figure 6-8). The eccentricity in the aligned setup increased during welding, while eccentric tool setups show a significant decrease in eccentricity during welding. These observations suggest that, as discussed in Section 6.4.1, the eccentricity was effectively dampened by the FSW machine/system, but consequently, the tool undergoes larger force fluctuations as the eccentricity becomes larger. As mentioned earlier, this cyclic bending can therefore be potentially detrimental to the tool life, particularly if a higher weld speed and lower rotational speed are utilized.

## **7.2 Overall summary**

In conclusion, while several works have suggested the advantages of eccentric tool design on joint quality, based on the results obtained in this study, the author is of the opinion that tool eccentricity should be minimized when the FSW process is to be applied on thick-plate aluminium alloys. The reason for this recommendation is that, while negligible improvements can be seen in the joint’s mechanical performance despite observable changes in the joint’s properties and structure, unnecessary loadings are imposed on the tool, which would be detrimental to the tool life, and by extension, the FSW machine itself. Where thick-plate FSW of aluminium alloys is concerned, the disadvantages do seem to outweigh the advantages of utilizing tools with artificial eccentricity ( $\geq 0.2$  mm). However, based on the findings here, it suggests that modest values ( $< 0.05$  mm) of random eccentricity related to the values of tolerance on typical spindles do not appear to have a notable effect on joint performance.

While it is still not common practice, it is suggested that, prior to the welding process, the tool should be jogged/free rotated and the tool eccentricity should be checked using a dial gauge each time it is firmly secured onto the spindle. Any eccentricity exceeding 0.05 mm should be fixed to avoid any possibility of introducing undesired properties as an outcome of unintentionally large tool eccentricity.

Finally, it is worth noting that the conclusion and recommendations made here are based on the limited scope of this study, which includes the compliance of the milling machine, welding parameters, tool design and material thickness. Other than the future work suggested below, iterations on a wider parameter range, alternative tool design and material thickness would be worthwhile to explore.

### **7.3 Future outlook and suggestions**

Since the strain rate in the stir zone is enhanced with eccentric setup, it would be of interest to expand such setup to friction stir processing (FSP) of metal matrix composites (MMCs), where FSP is mainly utilized to refine the composite particles in the stir zone. Tool eccentricity is postulated to enhance such refinement and distribute the secondary phases more uniformly because of the enhanced strain rate imposed.

In addition, simulation of heat generation and strain rate for tool eccentricity setup could support and validate the empirical work conducted in this study. Further experiments on strain rate by expanding the parameters would be of future interest as well to validate the initial results of this study. Additional observations on the possible change on the joint's residual stress would also be worthwhile.

Works on modelling would also be valuable to confirm and elucidate the observations of the dynamic material flow in the stir zone, as well as the change in crystallographic texture orientation when an eccentric tool is employed.

Finally, in Section 4.4.4, tool eccentricity is seen to be potentially detrimental when kissing bond is present. Therefore, it would be of interest to expand this evaluation to determine the critical kissing bond length that would initiate premature failure.

## References

- [1] R. S. Mishra and M. W. Mahoney, *Friction Stir Welding and Processing*, 1st ed. Materials Park, Ohio: ASM International, 2007.
- [2] H. Bisadi, A. Tavakoli, M. T. Sangsaraki, and K. T. Sangsaraki, "The influences of rotational and welding speeds on microstructures and mechanical properties of friction stir welded Al5083 and commercially pure copper sheets lap joints," *Mater. Des.*, vol. 43, pp. 80–88, 2013.
- [3] X. Cao and M. Jahazi, "Effect of tool rotational speed and probe length on lap joint quality of a friction stir welded magnesium alloy," *Mater. Des.*, vol. 32, no. 1, pp. 1–11, 2011.
- [4] L. Zhou, H. J. Liu, and Q. W. Liu, "Effect of rotation speed on microstructure and mechanical properties of Ti-6Al-4V friction stir welded joints," *Mater. Des.*, vol. 31, no. 5, pp. 2631–2636, 2010.
- [5] P. Cavaliere, a. Squillace, and F. Panella, "Effect of welding parameters on mechanical and microstructural properties of AA6082 joints produced by friction stir welding," *J. Mater. Process. Technol.*, vol. 200, no. 1–3, pp. 364–372, May 2008.
- [6] M. N. James, D. G. Hattingh, and G. R. Bradley, "Weld tool travel speed effects on fatigue life of friction stir welds in 5083 aluminium," *Int. J. Fatigue*, vol. 25, no. 12, pp. 1389–1398, 2003.
- [7] K. A. Hassan, P. B. Prangnell, A. F. Norman, D. A. Price, and S. W. Williams, "Effect of welding parameters on nugget zone microstructure and properties in high strength aluminium alloy friction stir welds," *Sci. Technol. Weld. Join.*, vol. 8, no. 4, pp. 257–268, 2003.
- [8] M. A. Gharacheh, A. H. Khokabi, G. H. Daneshi, B. Shalchi, and R. Sarrafi, "The influence of the ratio of 'rotational speed/traverse speed'(w/v) on mechanical properties of AZ31 friction stir welds," *Int. J. Mach. Tools Manuf.*, vol. 46, no. 15, pp. 1983–1987, 2006.
- [9] G. Buffa, J. Hua, R. Shivpuri, and L. Fratini, "Design of the friction stir welding tool using the continuum based FEM model," *Mater. Sci. Eng. A*, vol. 419, pp. 381–388, 2006.
- [10] H. Fujii, L. Cui, M. Maeda, and K. Nogi, "Effect of tool shape on mechanical properties and microstructure of friction stir welded aluminum alloys," *Mater. Sci. Eng. A*, vol. 419, pp. 25–31, 2006.
- [11] Y. Huang, X. Y. X. Meng, Z. Lv, and J. Cao, "Numerical design of high depth-to-width ratio friction stir welding," *J. Mater. Process. Technol.*, vol. 252, pp. 233–241, 2018.
- [12] A. Arora, A. De, and T. Debroy, "Toward optimum friction stir welding tool shoulder diameter," *Scr. Mater.*, vol. 64, pp. 9–12, 2011.
- [13] N. H. Othman, M. Ishak, and L. H. Shah, "Effect of shoulder to pin ratio on magnesium alloy Friction Stir Welding," in *IOP Conference Series: Materials Science and*

- Engineering*, 2017, vol. 238, no. 1.
- [14] R. Nandan, T. DebRoy, and H. K. D. H. Bhadeshia, "Recent advances in friction-stir welding - Process, weldment structure and properties," *Prog. Mater. Sci.*, vol. 53, no. 6, pp. 980–1023, 2008.
  - [15] R. S. Mishra and Z. Y. Ma, "Friction stir welding and processing," *Mater. Sci. Eng. R*, vol. 50, no. 1–2, pp. 1–78, 2005.
  - [16] A. C. de O. Miranda, A. Gerlich, and S. Walbridge, "Aluminum friction stir welds: Review of fatigue parameter data and probabilistic fracture mechanics analysis," *Eng. Fract. Mech.*, vol. 147, no. January 2016, pp. 243–260, 2015.
  - [17] R. Rai, A. De, H. K. D. H. Bhadeshia, and T. DebRoy, "Review: friction stir welding tools," *Sci. Technol. Weld. Join.*, vol. 16, no. 4, pp. 325–342, 2011.
  - [18] Y. N. Zhang, X. Cao, S. Larose, and P. Wanjara, "Review of tools for friction stir welding and processing," *Can. Metall. Q.*, 2012.
  - [19] R. Kumar, V. Pancholi, and R. P. Bharti, "Material flow visualization and determination of strain rate during friction stir welding," *J. Mater. Process. Technol.*, vol. 255, no. July 2017, pp. 470–476, 2018.
  - [20] M. S. Sidhu and S. S. Chatha, "Friction Stir Welding – Process and its Variables : A Review," *Int. J. Emerg. Technol. Adv. Eng.*, vol. 2, no. 12, p. 5, 2012.
  - [21] A. L. Biro, B. F. Chenelle, and D. A. Lados, "Processing, microstructure, and residual stress effects on strength and fatigue crack growth properties in friction stir welding: A review," *Metall. Mater. Trans. B Process Metall. Mater. Process. Sci.*, vol. 43, no. 6, pp. 1622–1637, 2012.
  - [22] L. Dubourg and P. Dacheux, "Design and properties of FSW tools : a literature review," *6th Int. Symp. Frict. Stir Weld.*, p. 2, 2006.
  - [23] W. Woo, Z. Feng, X. Wang, and S. A. David, "Neutron diffraction measurements of residual stresses in friction stir welding: a review," *Sci. Technol. Weld. Join.*, vol. 16, no. 1, pp. 23–32, 2011.
  - [24] T. R. McNelley, S. Swaminathan, and J. Q. Su, "Recrystallization mechanisms during friction stir welding/processing of aluminum alloys," *Scr. Mater.*, vol. 58, no. 5, pp. 349–354, 2008.
  - [25] K. Deplus, A. Simar, W. Van Haver, and B. De Meester, "Residual stresses in aluminium alloy friction stir welds," *Int. J. Adv. Manuf. Technol.*, vol. 56, no. 5–8, pp. 493–504, 2011.
  - [26] A. K. Lakshminarayanan and V. Balasubramanian, "Process parameters optimization for friction stir welding of RDE-40 aluminium alloy using Taguchi technique," *Trans. Nonferrous Met. Soc. China*, vol. 18, pp. 548–554, 2008.
  - [27] X. He, F. Gu, and A. Ball, "A review of numerical analysis of friction stir welding," *Prog. Mater. Sci.*, vol. 65, pp. 1–66, 2014.

- [28] A. Simar, Y. Bréchet, B. De Meester, A. Denquin, C. Gallais, and T. Pardoën, “Integrated modeling of friction stir welding of 6xxx series Al alloys: Process, microstructure and properties,” *Prog. Mater. Sci.*, 2012.
- [29] C. C. Tutum and J. H. Hattel, “Numerical optimisation of friction stir welding: review of future challenges,” *Sci. Technol. Weld. Join.*, vol. 16, no. 4, pp. 318–324, 2011.
- [30] O. Lorrain, J. Serri, V. Favier, H. Zahrouni, and M. El Hadrouz, “A contribution to a critical review of friction stir welding numerical simulation,” *J. Mech. Mater. Struct.*, vol. 4, no. 2, pp. 351–369, 2009.
- [31] D. M. Neto and P. Neto, “Numerical modeling of friction stir welding process: A literature review,” *Int. J. Adv. Manuf. Technol.*, vol. 65, no. 1–4, pp. 115–126, 2013.
- [32] B. T. Gibson *et al.*, “Friction stir welding: Process, automation, and control,” *J. Manuf. Process.*, vol. 16, no. 1, pp. 56–73, 2014.
- [33] N. Mendes, P. Neto, A. Loureiro, and A. P. Moreira, “Machines and control systems for friction stir welding: A review,” *Mater. Des.*, vol. 90, pp. 256–265, 2016.
- [34] G. K. Padhy, C. S. Wu, and S. Gao, “Auxiliary energy assisted friction stir welding – status review,” *Sci. Technol. Weld. Join.*, vol. 20, no. 8, pp. 631–649, 2015.
- [35] P. L. Threadgill, A. J. Leonard, H. R. Shercliff, and P. J. Withers, “Friction stir welding of aluminium alloys,” *Int. Mater. Rev.*, vol. 54, no. 2, pp. 49–93, 2009.
- [36] C. A. W. Olea, L. Roldo, T. R. Strohaecker, and J. F. Dos Santos, “Friction stir welding of precipitate hardenable aluminium alloys: A Review,” *Weld. World*, vol. 50, no. 11–12, pp. 78–87, 2006.
- [37] G. Çam and S. Mistikoglu, “Recent developments in friction stir welding of Al-Alloys,” *J. Mater. Eng. Perform.*, vol. 23, no. 6, pp. 1936–1953, 2014.
- [38] S. K. Tiwari, D. K. Shukla, and R. Chandra, “Friction-Stir-Welding-of-Aluminum-Alloys-A-Review,” vol. 7, no. 12, pp. 1315–1320, 2013.
- [39] G. Çam, “Friction stir welded structural materials: beyond Al-alloys,” *Int. Mater. Rev.*, vol. 56, no. 1, pp. 1–48, 2011.
- [40] K. Singh, G. Singh, and H. Singh, “Review on friction stir welding of magnesium alloys,” *J. Magnes. Alloy.*, vol. 6, no. 4, pp. 399–416, 2018.
- [41] F. Simoes and D. M. Rodrigues, “Material flow and thermo-mechanical conditions during Friction Stir Welding of polymers: Literature review, experimental results and empirical analysis,” *Mater. Des.*, vol. 59, pp. 344–351, 2014.
- [42] S. Eslami, P. J. Tavares, and P. M. G. P. Moreira, “Friction stir welding tooling for polymers: review and prospects,” *Int. J. Adv. Manuf. Technol.*, vol. 89, no. 5–8, pp. 1677–1690, 2017.
- [43] L. H. Shah, N. H. Othman, and A. Gerlich, “Review of research progress on aluminium–magnesium dissimilar friction stir welding,” *Sci. Technol. Weld. Join.*, vol. 23, no. 3, pp. 256–270, 2018.

- [44] S. A. Hussein, A. S. M. Tahir, and A. B. Hadzley, “Characteristics of aluminum-to-steel joint made by friction stir welding: A review,” *Mater. Today Commun.*, vol. 5, pp. 32–49, 2015.
- [45] L. E. Murr, “A review of FSW research on dissimilar metal and alloy systems,” *J. Mater. Eng. Perform.*, vol. 19, no. 8, pp. 1071–1089, 2010.
- [46] T. DebRoy and H. K. D. H. Bhadeshia, “Friction stir welding of dissimilar alloys – a perspective,” *Sci. Technol. Weld. Join.*, vol. 15, no. 4, pp. 266–270, 2010.
- [47] K. P. Mehta and V. J. Badheka, “A review on dissimilar friction stir welding of copper to aluminum: Process, properties, and variants,” *Mater. Manuf. Process.*, vol. 31, no. 3, pp. 233–254, 2016.
- [48] X. Wang, Y. Pan, and D. A. Lados, “Friction stir welding of dissimilar Al/Al and Al/Non-Al alloys: A review,” *Metall. Mater. Trans. B*, vol. 49, no. 4, pp. 2097–2117, 2018.
- [49] A. Simar and M.-N. Avettand-Fenoel, “State of the art about dissimilar metal friction stir welding,” *Sci. Technol. Weld. Join.*, vol. 22, no. 5, pp. 389–403, 2017.
- [50] I. Galvão, A. Loureiro, and D. M. Rodrigues, “Critical review on friction stir welding of aluminium to copper,” *Sci. Technol. Weld. Join.*, vol. 21, no. 7, pp. 523–546, 2016.
- [51] B. Vijaya Ramnath, S. Abhishek Subramanian, R. Rakesh, S. Sharun Krishnan, and A. L. Ashwin Ramanathan, “A review on friction stir welding of aluminium metal matrix composites,” *IOP Conf. Ser. Mater. Sci. Eng.*, vol. 390, no. 1, 2018.
- [52] H. S. Arora, H. Singh, and B. K. Dhindaw, “Composite fabrication using friction stir processing - A review,” *Int. J. Adv. Manuf. Technol.*, vol. 61, no. 9–12, pp. 1043–1055, 2012.
- [53] M. N. Avettand-Fènoël and A. Simar, “A review about Friction Stir Welding of metal matrix composites,” *Mater. Charact.*, vol. 120, pp. 1–17, 2016.
- [54] O. S. Salih, H. Ou, W. Sun, and D. G. McCartney, “A review of friction stir welding of aluminium matrix composites,” *Mater. Des.*, vol. 86, pp. 61–71, 2015.
- [55] R. J. Seethaler and I. Yellowley, “The identification of radial runout in milling operations,” *J. Manuf. Sci. Eng.*, vol. 121, no. 3, p. 524, 1999.
- [56] W. A. Kline and R. E. DeVor, “The effect of runout on cutting geometry and forces in end milling,” *Int. J. Mach. Tool Des. Res.*, vol. 23, no. 2–3, pp. 123–140, 1983.
- [57] L. H. Shah, S. Walbridge, and A. Gerlich, “Tool eccentricity in friction stir welding: a comprehensive review,” *Sci. Technol. Weld. Join.*, vol. 24, no. 6, pp. 566–578, 2019.
- [58] N. Guo, M. R. Wang, Q. Meng, L. Zhou, and D. Y. Tang, “Effect of tool eccentricity on surface periodic banded structures in friction stir welding,” *IOP Conf. Ser. Mater. Sci. Eng.*, vol. 103, no. 1, 2015.
- [59] R. Fonda, A. Reynolds, C. R. Feng, K. Knipling, and D. Rowenhorst, “Material Flow in Friction Stir Welds,” *Metall. Mater. Trans. A*, vol. 44, no. 1, pp. 337–344, 2013.

- [60] J. H. Yan, M. A. Sutton, and A. P. Reynolds, "Processing and banding in AA2524 and AA2024 friction stir welding," *Sci. Technol. Weld. Join.*, vol. 12, no. 5, pp. 390–401, 2007.
- [61] M. F. Zaeh and P. Gebhard, "Dynamical behaviour of machine tools during friction stir welding," *Prod. Eng. Res. Dev.*, vol. 4, pp. 615–624, 2010.
- [62] Y. Mao, L. Ke, F. Liu, Q. Liu, C. Huang, and L. Xing, "Effect of tool pin eccentricity on microstructure and mechanical properties in friction stir welded 7075 aluminum alloy thick plate," *Mater. Des.*, vol. 62, pp. 334–343, 2014.
- [63] S. Amini, M. R. Amiri, and A. Barani, "Investigation of the effect of tool geometry on friction stir welding of 5083-O aluminum alloy," *Int. J. Adv. Manuf. Technol.*, vol. 76, no. 1–4, pp. 255–261, 2015.
- [64] Y. Chen *et al.*, "Influence of tool pin eccentricity on microstructural evolution and mechanical properties of friction stir processed Al-5052 alloy," *Mater. Sci. Eng. A*, vol. 739, pp. 272–276, 2019.
- [65] L. H. Shah, S. Guo, S. Walbridge, and A. Gerlich, "Effect of tool eccentricity on the properties of friction stir welded AA6061 aluminum alloys," *Manuf. Lett.*, vol. 15, pp. 14–17, 2018.
- [66] A. Oosterkamp, L. D. Oosterkamp, and A. Nordeide, "'Kissing Bond' Phenomena in Solid-State Welds of Aluminum Alloys," *Weld. J.*, no. August, pp. 225–231, 2004.
- [67] B. Li, Y. Shen, and W. Hu, "The study on defects in aluminum 2219-T6 thick butt friction stir welds with the application of multiple non-destructive testing methods," *Mater. Des.*, vol. 32, no. 4, pp. 2073–2084, 2011.
- [68] M. Kadlec, R. Ružek, and L. Nováková, "Mechanical behaviour of AA 7475 friction stir welds with the kissing bond defect," *Int. J. Fatigue*, vol. 74, pp. 7–19, 2015.
- [69] C. Zhou, X. Yang, and G. Luan, "Effect of kissing bond on fatigue behavior of friction stir welds on Al 5083 alloy," *J. Mater. Sci.*, vol. 41, no. 10, pp. 2771–2777, 2006.
- [70] K. Kumar and S. V. Kailas, "The role of friction stir welding tool on material flow and weld formation," *Mater. Sci. Eng. A*, vol. 485, no. 1–2, pp. 367–374, 2008.
- [71] P. A. Colegrove and H. R. Shercliff, "CFD modelling of friction stir welding of thick plate 7449 aluminium alloy," *Sci. Technol. Weld. Join.*, vol. 11, no. 4, pp. 429–441, 2006.
- [72] S. J. Vijay and N. Murugan, "Influence of tool pin profile on the metallurgical and mechanical properties of friction stir welded Al-10wt.% TiB<sub>2</sub> metal matrix composite," *Mater. Des.*, vol. 31, no. 7, pp. 3585–3589, 2010.
- [73] K. Elangovan and V. Balasubramanian, "Influences of pin profile and rotational speed of the tool on the formation of friction stir processing zone in AA2219 aluminium alloy," *Mater. Sci. Eng. A*, vol. 459, no. 1–2, pp. 7–18, 2007.
- [74] R. Palanivel, P. Koshy Mathews, N. Murugan, and I. Dinaharan, "Effect of tool rotational speed and pin profile on microstructure and tensile strength of dissimilar friction stir



- welded AA5083-H111 and AA6351-T6 aluminum alloys,” *Mater. Des.*, vol. 40, pp. 7–16, 2012.
- [75] F. Gratecap, M. Girard, S. Marya, and G. Racineux, “Exploring material flow in friction stir welding: Tool eccentricity and formation of banded structures,” *Int. J. Mater. Form.*, vol. 5, no. 2, pp. 99–107, 2012.
- [76] M. Boz and A. Kurt, “The influence of stirrer geometry on bonding and mechanical properties in friction stir welding process,” *Mater. Des.*, vol. 25, pp. 343–347, 2004.
- [77] K. Elangovan and V. Balasubramanian, “Influences of tool pin profile and welding speed on the formation of friction stir processing zone in AA2219 aluminium alloy,” *J. Mater. Process. Technol.*, vol. 200, no. 1–3, pp. 163–175, May 2008.
- [78] K. Elangovan, V. Balasubramanian, and M. Valliappan, “Influences of tool pin profile and axial force on the formation of friction stir processing zone in AA6061 aluminium alloy,” *Int. J. Adv. Manuf. Technol.*, vol. 38, no. 3–4, pp. 285–295, 2008.
- [79] K. Elangovan, V. Balasubramanian, and S. Babu, “Predicting tensile strength of friction stir welded AA6061 aluminium alloy joints by a mathematical model,” *Mater. Des.*, vol. 30, no. 1, pp. 188–193, 2009.
- [80] G. Padmanaban and V. Balasubramanian, “Selection of FSW tool pin profile , shoulder diameter and material for joining AZ31B magnesium alloy – An experimental approach,” *Mater. Des.*, vol. 30, no. 7, pp. 2647–2656, 2009.
- [81] S. Babu, K. Elangovan, V. Balasubramanian, and M. Balasubramanian, “Optimizing friction stir welding parameters to maximize tensile strength of AA2219 aluminum alloy joints,” *Met. Mater. Int.*, vol. 15, no. 2, pp. 321–330, 2009.
- [82] C. N. Suresha, B. M. Rajaprakash, and S. Upadhya, “A study of the effect of tool pin profiles on tensile strength of welded joints produced using friction stir welding process,” *Mater. Manuf. Process.*, vol. 26, no. 9, pp. 1111–1116, 2011.
- [83] S. Gopalakrishnan and N. Murugan, “Prediction of tensile strength of friction stir welded aluminium matrix TiCp particulate reinforced composite,” *Mater. Des.*, vol. 32, no. 1, pp. 462–467, 2011.
- [84] H. K. Mohanty, M. M. Mahapatra, P. Kumar, P. Biswas, and N. R. Mandal, “Modeling the Effects of Tool Shoulder and Probe Profile Geometries on Friction Stirred Aluminum Welds Using Response Surface Methodology,” pp. 493–503, 2012.
- [85] A. Kumar and L. S. Raju, “Influence of tool pin profiles on friction stir welding of copper,” *Mater. Manuf. Process.*, vol. 27, no. 12, pp. 1414–1418, 2012.
- [86] K. Ramanjaneyulu, G. M. Reddy, A. V Rao, and R. Markandeya, “Structure-property correlation of AA2014 friction stir welds: role of tool pin profile,” *J. Mater. Eng. Perform.*, vol. 22, no. 8, pp. 2224–2240, 2013.
- [87] H. Khodaverdizadeh, A. Heidarzadeh, and T. Saeid, “Effect of tool pin profile on microstructure and mechanical properties of friction stir welded pure copper joints,” *Mater. Des.*, vol. 45, pp. 265–270, 2013.

- [88] W. Xu, J. Liu, H. Zhu, and L. Fu, "Influence of welding parameters and tool pin profile on microstructure and mechanical properties along the thickness in a friction stir welded aluminum alloy," *Mater. Des.*, vol. 47, pp. 599–606, 2013.
- [89] M. Bahrami, M. K. B. Givi, K. Dehghani, and N. Parvin, "On the role of pin geometry in microstructure and mechanical properties of AA7075/SiC nano-composite fabricated by friction stir welding technique," *Mater. Des.*, vol. 53, no. 519–527, 2014.
- [90] P. Motalleb-Nejad, T. Saeid, A. Heidarzadeh, K. Darzi, and M. Ashjari, "Effect of tool pin profile on microstructure and mechanical properties of friction stir welded AZ31B magnesium alloy," *Mater. Des.*, vol. 59, no. 221–226, 2014.
- [91] J. Marzbanrad, M. Akbari, P. Asadi, and S. Safaee, "Characterization of the influence of tool pin profile on microstructural and mechanical properties of friction stir welding," *Metall. Mater. Trans. B*, vol. 45, no. 5, pp. 1887–1894, 2014.
- [92] K. P. Mehta and V. J. Badheka, "Effects of Tool Pin Design on Formation of Defects in Dissimilar Friction Stir Welding," *Procedia Technol.*, vol. 23, pp. 513–518, 2016.
- [93] P. Goel *et al.*, "Investigation on the effect of tool pin profiles on mechanical and microstructural properties of friction stir butt and scarf welded aluminium alloy 6063," *Metals (Basel)*, vol. 8, no. 1, p. 74, 2018.
- [94] H. Izadi, J. Fallu, A. Abdel-Gwad, T. Liyanage, and A. P. Gerlich, "Analysis of tool geometry in dissimilar Al alloy friction stir welds using optical microscopy and serial sectioning," *Sci. Technol. Weld. Join.*, vol. 18, no. 4, pp. 307–313, 2013.
- [95] K. J. Colligan, X. Junde, and J. R. Pickens, "Welding tool and process parameter effects in friction stir welding of aluminum alloys," in *Friction stir welding and processing II*, 2003, pp. 181–190.
- [96] M. Mehta, A. De, and T. DebRoy, "Material adhesion and stresses on friction stir welding tool pins," *Sci. Technol. Weld. Join.*, vol. 19, no. 6, pp. 534–540, 2014.
- [97] R. S. Mishra, P. S. De, and N. Kumar, *Friction stir welding and processing: Science and engineering*. Switzerland: Springer International Publishing, 2014.
- [98] A. C. Nunes Jr., "Metal flow in friction stir welding," in *Materials Science and Technology 2006/ASM International*, 2006, pp. 15–19.
- [99] W. . Thomas and E. . Nicholas, "Friction stir welding for the transportation industries," *Mater. Des.*, vol. 18, no. 4–6, pp. 269–273, 1997.
- [100] R. W. Fonda and J. F. Bingert, "Texture variations in an aluminum friction stir weld," *Scr. Mater.*, vol. 57, no. 11, pp. 1052–1055, 2007.
- [101] A. R. S. Essa, M. M. Z. Ahmed, A. K. Y. A. Mohamed, and A. E. El-Nikhaily, "An analytical model of heat generation for eccentric cylindrical pin in friction stir welding," *J. Mater. Res. Technol.*, vol. 5, no. 3, pp. 234–240, 2016.
- [102] R. Burek, D. Wydrzyński, J. Andres, and A. Wrońska, "Effect of tool eccentricity on microstructure and properties of FSW joints made of Al 7075 T6 alloy," *Adv. Sci.*

- Technol. Res. J.*, vol. 11, no. 4, pp. 333–338, 2017.
- [103] Z. W. Chen, T. Pasang, and Y. Qi, “Shear flow and formation of nugget zone during friction stir welding of aluminium alloy 5083-O,” *Mater. Sci. Eng. A*, vol. 474, no. 1–2, pp. 312–316, 2008.
- [104] H. Bin Chen, K. Yan, T. Lin, S. Ben Chen, C. Y. Jiang, and Y. Zhao, “The investigation of typical welding defects for 5456 aluminum alloy friction stir welds,” *Mater. Sci. Eng. A*, vol. 433, no. 1–2, pp. 64–69, 2006.
- [105] H. R. Doude, J. A. Schneider, and A. C. Nunes, “Influence of the tool shoulder contact conditions on the material flow during friction stir welding,” *Metall. Mater. Trans. A Phys. Metall. Mater. Sci.*, vol. 45, no. 10, pp. 4411–4422, 2014.
- [106] P. A. Colegrove and H. R. Shercliff, “3-Dimensional CFD modelling of flow round a threaded friction stir welding tool profile,” *J. Mater. Process. Technol.*, vol. 169, no. 2, pp. 320–327, 2005.
- [107] H. Schmidt and J. Hattel, “Modelling heat flow around tool probe in friction stir welding,” *Sci. Technol. Weld. Join.*, vol. 10, no. 2, pp. 176–186, 2005.
- [108] N. Zaman, A. Noor, Z. A. Khan, and S. K. Shihab, “Investigations on tunneling and kissing bond defects in FSW joints for dissimilar aluminum alloys,” *J. Alloys Compd.*, vol. 648, pp. 360–367, 2015.
- [109] L. Svensson *et al.*, “Microstructure and mechanical properties of friction stir welded aluminium alloys with special reference to AA 5083 and AA 6082,” *Sci. Technol. Weld. Join.*, vol. 5, no. 5, pp. 285–296, 2000.
- [110] A. Gerlich, M. Yamamoto, and T. H. North, “Strain rates and grain growth in Al 5754 and Al 6061 friction stir spot welds,” *Metall. Mater. Trans. A*, vol. 38, no. 6, pp. 1291–1302, 2007.
- [111] A. H. Feng, D. L. Chen, and Z. Y. Ma, “Microstructure and low-cycle fatigue of a friction-stir-welded 6061 aluminum alloy,” *Metall. Mater. Trans. A*, vol. 41, pp. 2626–2641, 2010.
- [112] L. H. Ahmad Shah, S. Sonbolestan, R. H. Midawi, S. Walbridge, and A. Gerlich, “Dissimilar friction stir welding of thick plate AA5052-AA6061 aluminum alloys: effects of material positioning and tool eccentricity,” *Int. J. Adv. Manuf. Technol.*, vol. 105, no. 1–4, pp. 889–904, 2019.
- [113] C. D. Marioara, S. J. Andersen, H. W. Zandbergen, and R. Holmestad, “The influence of alloy composition on precipitates of the Al-Mg-Si system,” *Metall. Mater. Trans. A*, vol. 36, pp. 691–702, 2005.
- [114] I. Radisavljevic, A. Zivkovic, N. Radovic, and V. Grabulov, “Influence of FSW parameters on formation quality and mechanical properties of Al 2024-T351 butt welded joints,” *Trans. Nonferrous Met. Soc. China*, vol. 23, no. 12, pp. 3525–3539, 2013.
- [115] H. Jamshidi Aval, S. Serajzadeh, and a. H. Kokabi, “Evolution of microstructures and mechanical properties in similar and dissimilar friction stir welding of AA5086 and

- AA6061,” *Mater. Sci. Eng. A*, vol. 528, no. 28, pp. 8071–8083, Oct. 2011.
- [116] A. P. Reynolds, “Flow visualization and simulation in FSW,” *Scr. Mater.*, vol. 58, no. 5, pp. 338–342, 2008.
- [117] J. Schneider and A. C. Nunes, “Characterization of plastic flow and resulting microtextures in a friction stir weld,” *Metall. Mater. Trans. B*, vol. 35, no. 8, pp. 777–783, 2004.
- [118] C. Hamilton, S. Dymek, and M. Blicharski, “A model of material flow during friction stir welding,” *Mater. Charact.*, vol. 59, no. 9, pp. 1206–1214, 2008.
- [119] Y. S. Sato, H. Kokawa, M. Enomoto, and S. Jogan, “Microstructural evolution of 6063 aluminum during friction-stir welding,” *Metall. Mater. Trans. A*, vol. 30, no. 9, pp. 2429–2437, 1999.
- [120] J.-Q. Su, T. W. Nelson, R. Mishra, and M. Mahoney, “Microstructural investigation of friction stir welded 7050- T651 aluminium,” *Acta Mater.*, vol. 51, pp. 713–729, 2003.
- [121] M. H. Jacobs, “The structure of the metastable precipitates formed during ageing of an Al-Mg-Si alloy,” *Philos. Mag.*, vol. 26, pp. 1–13, 1972.
- [122] H. W. L. Phillips, “The constitution of alloys of aluminium with magnesium, silicon, and iron,” *J. Inst. Met.*, vol. 72, no. 7, p. 151, 1946.
- [123] D. L. Zhang and L. Zheng, “The quench sensitivity of cast Al-7 wt pct Si-0.4 wt pct Mg alloy,” *Metall. Mater. Trans. A*, vol. 27, pp. 3983–3991, 1996.
- [124] Y. S. Sato, M. Urata, and H. Kokawa, “Parameters controlling microstructure and hardness during friction-stir welding of precipitation-hardenable aluminum alloy 6063,” *Metall. Mater. Trans. A*, vol. 33, no. 3, pp. 625–635, 2002.
- [125] W. Woo, H. Choo, D. W. Brown, and Z. Feng, “Influence of the tool pin and shoulder on microstructure and natural aging kinetics in a friction-stir-processed 6061-T6 aluminum alloy,” *Metall. Mater. Trans. A*, vol. 38, no. 1, pp. 69–76, 2007.
- [126] S. J. Andersen, “Quantification of the Mg<sub>2</sub>Si b” and b’ phases in AlMgSi alloys by transmission electron microscopy,” *Metall. Mater. Trans. A*, vol. 26A, pp. 1931–1937, 1995.
- [127] X. Wang, S. Esmaili, and D. J. Lloyd, “The sequence of precipitation in the Al-Mg-Si-Cu alloy AA6111,” *Metall. Mater. Trans. A*, vol. 37, pp. 2691–2699, 2006.
- [128] P. Seppehrband, X. Wang, H. Jin, and S. Esmaili, “Interactive microstructural phenomena during non-isothermal annealing of an Al-Mg-Si-Cu alloy,” *Mater. Charact.*, vol. 137, pp. 212–221, 2018.
- [129] S. Esmaili, D. J. Lloyd, and W. J. Poole, “Modeling of precipitation hardening for the naturally aged Al-Mg-Si-Cu alloy AA6111,” *Acta Mater.*, vol. 51, pp. 3467–3481, 2003.
- [130] S. J. Andersen, H. W. Zandbergen, J. Jansen, C. Traeholt, U. Tundal, and O. Reiso, “The crystal structure of the b” phase in Al-Mg-Si alloys,” *Acta Mater.*, vol. 46, no. 9, pp. 3283–3298, 1998.

- [131] C. Mandache, D. Levesque, L. Dubourg, and P. Gougeon, “Non-destructive detection of lack of penetration defects in friction stir welds,” *Sci. Technol. Weld. Join.*, vol. 17, no. 4, pp. 295–303, 2012.
- [132] S. Delrue, M. Tabatabaeipour, J. Hettler, and K. Van Den Abeele, “Applying a nonlinear, pitch-catch, ultrasonic technique for the detection of kissing bonds in friction stir welds,” *Ultrasonics*, vol. 68, pp. 71–79, 2016.
- [133] S. Guo, L. Shah, R. Ranjan, S. Walbridge, and A. Gerlich, “Effect of quality control parameter variations on the fatigue performance of aluminum friction stir welded joints,” *Int. J. Fatigue*, vol. 118, pp. 150–161, 2018.
- [134] A. P. Reynolds, “Visualisation of material flow in autogenous friction stir welds,” *Sci. Technol. Weld. Join.*, vol. 5, no. 2, pp. 120–124, 2000.
- [135] T. Dickerson, H. R. Shercliff, and H. Schmidt, “A weld marker technique for flow visualization in friction stir welding,” *4th Int. Symp. Frict. Stir Weld.*, pp. 14–16, 2003.
- [136] T. U. Seidel and A. P. Reynolds, “Visualization of the material flow in AA2195 friction-stir welds using a marker insert technique,” *Metall. Mater. Trans. A*, vol. 32, no. 11, pp. 2879–2884, 2001.
- [137] H. N. B. Schmidt, T. L. Dickerson, and J. H. Hattel, “Material flow in butt friction stir welds in AA2024-T3,” *Acta Mater.*, vol. 54, no. 4, pp. 1199–1209, 2006.
- [138] M. Guerra, C. Schmidt, J. C. McClure, L. E. Murr, and A. C. Nunes, “Flow patterns during friction stir welding,” *Mater. Charact.*, vol. 49, pp. 95–101, 2003.
- [139] O. Lorrain, V. Favier, H. Zahrouni, and D. Lawrjaniec, “Understanding the material flow path of friction stir welding process using unthreaded tools,” *J. Mater. Process. Technol.*, vol. 210, no. 4, pp. 603–609, 2010.
- [140] D. Q. Qin, L. Fu, and Z. K. Shen, “Visualisation and numerical simulation of material flow behaviour during high-speed FSW process of 2024 aluminium alloy thin plate,” 2019.
- [141] X. C. Liu, Y. F. Sun, Y. Morisada, and H. Fujii, “Dynamics of rotational flow in friction stir welding of aluminium alloys,” *J. Mater. Process. Tech.*, vol. 252, pp. 643–651, 2018.
- [142] M. Gulbudak and Y. Bozkurt, “The effect of process parameters on the material position of dissimilar friction stir welded AA2024-T3 / 5754-H22 joints,” *Kov. Mater.*, vol. 55, pp. 21–31, 2017.
- [143] M. M. Moradi, H. Jamshidi Aval, R. Jamaati, S. Amir Khanlou, and S. Ji, “Microstructure and texture evolution of friction stir welded dissimilar aluminum alloys: AA2024 and AA6061,” *J. Manuf. Process.*, vol. 32, no. April, pp. 1–10, 2018.
- [144] S. T. Amancio-Filho, S. Sheikhi, J. F. dos Santos, and C. Bolfarini, “Preliminary study on the microstructure and mechanical properties of dissimilar friction stir welds in aircraft aluminium alloys 2024-T351 and 6056-T4,” *J. Mater. Process. Technol.*, vol. 206, no. 1–3, pp. 132–142, 2008.

- [145] A. Scialpi, L. A. C. De Filippis, and P. Cavaliere, “Influence of shoulder geometry on microstructure and mechanical properties of friction stir welded 6082 aluminium alloy,” *Mater. Des.*, vol. 28, no. 4, pp. 1124–1129, 2007.
- [146] J. H. Ouyang and R. Kovacevic, “Material Flow and Microstructure in the Friction Stir Butt Welds of the Same and Dissimilar Aluminum Alloys,” *J. Mater. Eng. Perform.*, vol. 11, pp. 51–63, 2002.
- [147] P. Cavaliere, A. De Santis, F. Panella, and A. Squillace, “Effect of welding parameters on mechanical and microstructural properties of dissimilar AA6082–AA2024 joints produced by friction stir welding,” *Mater. Des.*, vol. 30, no. 3, pp. 609–616, 2009.
- [148] L. Giraud, H. Robe, C. Claudin, C. Desrayaud, P. Bocher, and E. Feulvarch, “Investigation into the dissimilar friction stir welding of AA7020-T651 and AA6060-T6,” *J. Mater. Process. Technol.*, vol. 235, pp. 220–230, 2016.
- [149] R. I. Rodriguez, J. B. Jordon, P. G. Allison, T. Rushing, and L. Garcia, “Microstructure and mechanical properties of dissimilar friction stir welding of 6061-to-7050 aluminum alloys,” *Mater. Des.*, vol. 83, pp. 60–65, 2015.
- [150] J. F. Guo, H. C. Chen, C. N. Sun, G. Bi, Z. Sun, and J. Wei, “Friction stir welding of dissimilar materials between AA6061 and AA7075 Al alloys effects of process parameters,” *Mater. Des.*, vol. 56, pp. 185–192, Apr. 2014.
- [151] O. Gopkalo, X. Liu, F. Long, M. Booth, A. P. Gerlich, and B. J. Diak, “Non-isothermal thermal cycle process model for predicting post-weld hardness in friction stir welding of dissimilar age-hardenable aluminum alloys,” *Mater. Sci. Eng. A*, vol. 754, pp. 205–215, 2019.
- [152] R. I. Rodriguez, J. B. Jordon, P. G. Allison, T. W. Rushing, and L. Garcia, “Corrosion effects on fatigue behavior of dissimilar friction stir welding of high-strength aluminum alloys,” *Mater. Sci. Eng. A*, vol. 742, pp. 255–268, 2019.
- [153] A. Barbini, J. Carstensen, and J. dos Santos, “Influence of Alloys Position, Rolling and Welding Directions on Properties of AA2024/AA7050 Dissimilar Butt Weld Obtained by Friction Stir Welding,” *Metals (Basel)*, vol. 8, no. 4, p. 202, 2018.
- [154] S. A. Khodir and T. Shibayanagi, “Dissimilar friction stir welded joints between 2024-T3 aluminum alloy and AZ31 magnesium alloy,” *Mater. Trans.*, vol. 48, no. 9, pp. 2501–2505, 2007.
- [155] P. Cavaliere, R. Nobile, F. W. Panella, and a. Squillace, “Mechanical and microstructural behaviour of 2024–7075 aluminium alloy sheets joined by friction stir welding,” *Int. J. Mach. Tools Manuf.*, vol. 46, no. 6, pp. 588–594, May 2006.
- [156] V. R. Kishore, J. Arun, R. Padmanabhan, and V. Balasubramanian, “Parametric studies of dissimilar friction stir welding using computational fluid dynamics simulation,” *Int. J. Adv. Manuf. Technol.*, vol. 80, pp. 91–98, 2015.
- [157] P. Cavaliere and F. Panella, “Effect of tool position on the fatigue properties of dissimilar 2024-7075 sheets joined by friction stir welding,” *J. Mater. Process. Technol.*, vol. 206,

- pp. 249–255, 2008.
- [158] P. Bahemmat and M. Haghpanahi, “Study on dissimilar friction stir butt welding of AA7075-O and AA2024-T4 considering the manufacturing limitation,” *Int. J. Adv. Manuf. Technol.*, vol. 59, pp. 939–953, 2012.
- [159] A. A. M. Silva, E. Arruti, G. Janeiro, E. Aldanondo, P. Alvarez, and A. Echeverria, “Material flow and mechanical behaviour of dissimilar AA2024-T3 and AA7075-T6 aluminium alloys friction stir welds,” *Mater. Des.*, vol. 32, no. 4, pp. 2021–2027, 2011.
- [160] J. Tang and Y. Shen, “Numerical simulation and experimental investigation of friction stir lap welding between aluminum alloys AA2024 and AA7075,” *J. Alloys Compd.*, vol. 666, pp. 493–500, 2016.
- [161] N. Zaman, A. Noor, Z. A. Khan, and A. K. Mukhopadhyay, “Mechanical and microstructural behavior of friction stir welded similar and dissimilar sheets of AA2219 and AA7475 aluminium alloys,” *J. Alloys Compd.*, vol. 695, pp. 2902–2908, 2017.
- [162] P. L. Niu, W. Y. Li, N. Li, Y. X. Xu, and D. L. Chen, “Exfoliation corrosion of friction stir welded dissimilar 2024-to-7075 aluminum alloys,” *Mater. Charact.*, vol. 147, pp. 93–100, 2019.
- [163] R. D. Kumar, M. S. I. U. Hassan, and S. Muthukumaran, “Single and multi-response optimization and Validation of mechanical properties in dissimilar friction stir welded AA2219-T87 and AA7075-T73 Alloys using T-GRA,” *Exp. Tech.*, vol. 43, pp. 245–259, 2019.
- [164] B. Wang, B. B. Lei, J. X. Zhu, Q. Feng, L. Wang, and D. Wu, “EBSD study on microstructure and texture of friction stir welded AA5052-O and AA6061-T6 dissimilar joint,” *Mater. Des.*, vol. 87, pp. 593–599, 2015.
- [165] M. Ilangoan, S. Rajendra Boopathy, and V. Balasubramanian, “Effect of tool pin profile on microstructure and tensile properties of friction stir welded dissimilar AA 6061–AA 5086 aluminium alloy joints,” *Def. Technol.*, vol. 11, no. 2, pp. 174–184, 2015.
- [166] N. F. M. Selamat, A. H. Baghdadi, Z. Sajuri, and A. H. Kokabi, “Friction stir welding of similar and dissimilar aluminium alloys for automotive applications,” *Int. J. Automot. Mech. Eng.*, vol. 13, no. 2, pp. 3401–3412, 2016.
- [167] M. Ahmadnia, S. Shahraki, and M. A. Kamarposhti, “Experimental studies on optimized mechanical properties while dissimilar joining AA6061 and AA5010 in a friction stir welding process,” *Int. J. Adv. Manuf. Technol.*, vol. 87, no. 5–8, pp. 2337–2352, 2016.
- [168] M. J. Peel, A. Steuwer, P. J. Withers, T. Dickerson, Q. Shi, and H. Shercliff, “Dissimilar friction stir welds in AA5083-AA6082. Part I: Process parameter effects on thermal history and weld properties,” *Metall. Mater. Trans. A Phys. Metall. Mater. Sci.*, vol. 37, no. 7, pp. 2183–2193, 2006.
- [169] A. Steuwer, M. J. Peel, and P. J. Withers, “Dissimilar friction stir welds in AA5083-AA6082: The effect of process parameters on residual stress,” *Mater. Sci. Eng. A*, vol. 441, no. 1–2, pp. 187–196, 2006.

- [170] I. Shigematsu, Y. J. Kwon, K. Suzuki, T. Imai, and N. Saito, "Joining of 5083 and 6061 aluminium alloys by friction stir welding," *J. Mater. Sci. Lett.*, vol. 22, pp. 353–356, 2003.
- [171] H. Jamshidi Aval, S. Serajzadeh, A. H. Kokabi, and A. Loureiro, "Effect of tool geometry on mechanical and microstructural behaviours in dissimilar friction stir welding of AA 5086–AA 6061," *Sci. Technol. Weld. Join.*, vol. 16, no. 7, pp. 597–604, 2011.
- [172] H. Jamshidi Aval, S. Serajzadeh, and A. H. Kokabi, "Thermo-mechanical and microstructural issues in dissimilar friction stir welding of AA5086-AA6061," *J. Mater. Sci.*, vol. 46, no. 10, pp. 3258–3268, 2011.
- [173] S.-K. Park, S.-T. Hong, J.-H. Park, K.-Y. Park, Y.-J. Kwon, and H.-J. Son, "Effect of material locations on properties of friction stir welding joints of dissimilar aluminium alloys," *Sci. Technol. Weld. Join.*, vol. 15, no. 4, pp. 331–336, 2010.
- [174] V. RajKumar, M. VenkateshKannan, P. Sadeesh, N. Arivazhagan, and K. Devendranath Ramkumar, "Studies on effect of tool design and welding parameters on the friction stir welding of dissimilar aluminium alloys AA 5052 - AA 6061," *Procedia Eng.*, vol. 75, pp. 93–97, 2014.
- [175] Y. Chen, H. Wang, H. Li, X. Wang, H. Ding, and J. Zhao, "Investigation into the dissimilar friction stir welding of AA5052 and AA6061 aluminum alloys using pin-eccentric stir tool," *Metals (Basel)*, vol. 9, no. 7, p. 718, 2019.
- [176] P. Tayebi, A. Fazli, P. Asadi, and M. Soltanpour, "Formability analysis of dissimilar friction stir welded AA 6061 and AA 5083 blanks by SPIF process," *CIRP J. Manuf. Sci. Technol.*, vol. 25, pp. 50–68, 2019.
- [177] G. Peng, Q. Yan, J. Hu, P. Chen, Z. Chen, and T. Zhang, "Effect of forced air cooling on the microstructures, tensile strength, and hardness distribution of dissimilar friction stir welded AA5A06-AA6061 joints," *Metals (Basel)*, vol. 9, no. 3, p. 304, 2019.
- [178] A. Sasikumar, S. Gopi, and D. G. Mohan, "Effect of magnesium and chromium fillers on the microstructure and tensile strength of friction stir welded dissimilar aluminium alloys," *Mater. Res. Express*, vol. 6, no. 8, p. 086580, 2019.
- [179] S. Verma and V. Kumar, "Investigation of microhardness and microstructure using friction stir welding of dissimilar aluminium alloys," *J. Commun. Eng. Syst.*, vol. 8, no. 3, pp. 37–44, 2018.
- [180] K. N. Krishnan, "On the formation of onion rings in friction stir welds," *Mater. Sci. Eng. A*, vol. 327, no. 2, pp. 246–251, 2002.
- [181] J. G. Kaufman, "Aluminum alloy database," *Knovel*, 2004. .
- [182] S. S. Yutaka, H. Hiroyuki, K. Ikeda, M. Enomoto, S. Jogan, and T. Hashimoto, "Microtexture in the friction-stir weld of an aluminum alloy," *Metall. Mater. Trans. A Phys. Metall. Mater. Sci.*, vol. 32, no. 4, pp. 941–948, 2001.
- [183] D. P. Field, T. W. Nelson, Y. Hovanski, and K. V. Jata, "Heterogeneity of crystallographic texture in friction stir welds of aluminum," *Metall. Mater. Trans. A*, vol. 32, no. 11, pp. 2869–2877, 2001.



- [184] M. M. Z. Ahmed, B. P. Wynne, W. M. Rainforth, A. Addison, J. P. Martin, and P. L. Threadgill, "Effect of tool geometry and heat input on the hardness, grain structure, and crystallographic texture of thick-section friction stir-welded aluminium," *Metall. Mater. Trans. A*, vol. 50, no. 1, pp. 271–284, 2019.
- [185] R. W. Fonda and K. E. Knipling, "Texture development in friction stir welds," *Sci. Technol. Weld. Join.*, vol. 16, no. 4, pp. 288–294, 2011.
- [186] V. Patel, W. Li, A. Vairis, and V. Badheka, "Recent development in friction stir processing as a solid-state grain refinement technique : Microstructural evolution and property enhancement," *Crit. Rev. Solid State Mater. Sci.*, vol. 44, no. 5, pp. 378–426, 2019.
- [187] U. F. H. R. Suhuddin, S. Mironov, Y. S. Sato, and H. Kokawa, "Grain structure and texture evolution during friction stir welding of thin 6016 aluminum alloy sheets," *Mater. Sci. Eng. A*, vol. 527, no. 7–8, pp. 1962–1969, 2010.
- [188] Z. Y. Ma, A. H. Feng, D. L. Chen, and J. Shen, "Recent advances in friction stir welding/processing of aluminum alloys: Microstructural evolution and mechanical properties," *Crit. Rev. Solid State Mater. Sci.*, vol. 43, no. 4, pp. 269–333, 2018.
- [189] W. Woo, H. Choo, D. W. Brown, S. C. Vogel, P. K. Liaw, and Z. Feng, "Texture analysis of a friction stir processed 6061-T6 aluminum alloy using neutron diffraction," *Acta Mater.*, vol. 54, pp. 3871–3882, 2006.
- [190] J. Hirsch and K. Locke, "Mechanism of deformation and development of rolling textures in polycrystalline FCC metals-I. Description of rolling texture development in homogeneous CuZn alloys," *Acta Metall.*, vol. 36, no. 11, pp. 2863–2882, 1988.
- [191] L. S. Toth, K. W. Neale, and J. J. Jonas, "Stress response and persistence characteristics of the ideal orientations of shear textures," *Acta Metall.*, vol. 37, no. 8, pp. 2197–2210, 1989.
- [192] S. Li, I. J. Beyerlein, and M. A. M. Bourke, "Texture formation during equal channel angular extrusion of fcc and bcc materials : comparison with simple shear," *Mater. Sci. Eng. A*, vol. 394, pp. 66–77, 2005.
- [193] L. A. I. Kestens and H. Pirgazi, "Texture formation in metal alloys with cubic crystal structures," *Mater. Sci. Technol.*, vol. 32, no. 13, pp. 1303–1315, 2016.
- [194] R. Palanivel, P. Koshy Mathews, I. Dinaharan, and N. Murugan, "Mechanical and metallurgical properties of dissimilar friction stir welded AA5083-H111 and AA6351-T6 aluminum alloys," *Trans. Nonferrous Met. Soc. China*, vol. 24, no. 1, pp. 58–65, Jan. 2014.
- [195] G. Sundararajan and Y. Tirupataiah, "The hardness-flow stress correlation in metallic materials," *Bull. Mater. Sci.*, vol. 17, no. 6, pp. 747–770, 1994.
- [196] J. G. Kaufman, *Properties of Aluminum Alloys: Tensile, Creep and Fatigue Data at High and Low Temperatures*. Ohio, USA: ASM International, 1999.
- [197] W. Lee, Y. Yeon, and S. Jung, "The joint properties of dissimilar formed Al alloys by friction stir welding according to the fixed location of materials," *Scr. Mater.*, vol. 49, pp.

- 423–428, 2003.
- [198] J. Guo, P. Gougeon, and X. Chen, “Microstructure evolution and mechanical properties of dissimilar friction stir welded joints between AA1100-B 4 C MMC and AA6063 alloy,” *Mater. Sci. Eng. A*, vol. 553, pp. 149–156, 2012.
- [199] F. Thibeault, “Numerical and experimental study of friction stir welding (in French),” Université du Québec à Chicoutimi, 2012.
- [200] G. Qin, Y. Su, and S. Wang, “Microstructures and properties of welded joint of aluminum alloy to galvanized steel by Nd:YAG laser + MIG arc hybrid brazing-fusion welding,” *Trans. Nonferrous Met. Soc. China*, vol. 24, no. 4, pp. 989–995, Apr. 2014.
- [201] N. Martinez, N. Kumar, R. S. Mishra, and K. J. Doherty, “Microstructural variation due to heat gradient of a thick friction stir welded aluminum 7449 alloy,” *J. Alloys Compd.*, vol. 713, pp. 51–63, 2017.
- [202] J. Schneider, R. Beshears, and A. C. Nunes, “Interfacial sticking and slipping in the friction stir welding process,” *Mater. Sci. Eng. A*, vol. 435–436, pp. 297–304, 2006.
- [203] A. C. F. Silva, J. De Backer, and G. Bolmsjö, “Temperature measurements during friction stir welding,” *Int. J. Adv. Manuf. Technol.*, vol. 88, pp. 2899–2908, 2017.
- [204] Y. Hwang, Z. Kang, Y. Chiou, and H. Hsu, “Experimental study on temperature distributions within the workpiece during friction stir welding of aluminum alloys,” *Int. J. Mach. Tools Manuf.*, vol. 48, pp. 778–787, 2008.
- [205] A. J. Ardell, “Precipitation hardening,” *Metall. Trans. A*, vol. 16, no. 12, pp. 2131–2165, 1985.
- [206] W. Tang, X. Guo, J. C. McClure, L. E. Murr, and A. Nunes, “Heat Input and Temperature Distribution in Friction Stir Welding,” *J. Mater. Process. Manuf. Sci.*, vol. 7, no. 2, pp. 163–172, 1998.
- [207] C. Hamilton, S. Dymek, and A. Sommers, “A thermal model of friction stir welding in aluminum alloys,” *Int. J. Mach. Tools Manuf.*, vol. 48, pp. 1120–1130, 2008.
- [208] A. Gerlich, P. Su, and T. H. North, “Peak temperatures and microstructures in aluminium and magnesium alloy friction stir spot welds,” *Sci. Technol. Weld. Join.*, vol. 10, no. 6, pp. 647–652, 2005.
- [209] V. Malin, “Study of metallurgical phenomena in the HAZ of 6061-T6 aluminum welded joints,” *Weld. Res. Suppl.*, pp. 305–318, 1995.
- [210] Ø. Frigaard, Ø. Grong, and O. T. Midling, “A process model for friction stir welding of age hardening aluminum alloys,” *Metall. Mater. Trans. A*, vol. 32, no. May, pp. 1189–1200, 2001.
- [211] M. Peel, A. Steuwer, M. Preuss, and P. J. Withers, “Microstructure, mechanical properties and residual stresses as a function of welding speed in aluminium AA5083 friction stir welds,” *Acta Mater.*, vol. 51, no. 16, pp. 4791–4801, Sep. 2003.
- [212] A. H. Cottrell, “LXXXVI. A note on the Portevin-Le Chatelier effect,” *London*,

- Edinburgh, Dublin Philos. Mag. J. Sci.*, vol. 44, no. 355, pp. 829–832, 1953.
- [213] J. Coër, P. Y. Manach, H. Laurent, M. C. Oliveira, and L. F. Menezes, “Piobert – Lüders plateau and Portevin – Le Chatelier effect in an Al – Mg alloy in simple shear,” *Mech. Res. Commun.*, vol. 48, pp. 1–7, 2013.
- [214] H. Halim, D. S. Wilkinson, and M. Niewczas, “The Portevin – Le Chatelier ( PLC ) effect and shear band formation in an AA5754 alloy,” *Acta Mater.*, vol. 55, pp. 4151–4160, 2007.
- [215] J. A. Gerken, M. Gratzel, and J. P. Bergmann, “Investigation of the material flow during friction stir welding of EN-AW 5754 by multi-axial high resolution process force analysis,” in *12th International Symposium on Friction Stir Welding*, 2018, pp. 1–11.
- [216] P. B. Prangnell and C. P. Heason, “Grain structure formation during friction stir welding observed by the ‘stop action technique,’” *Acta Mater.*, vol. 53, pp. 3179–3192, 2005.
- [217] H. J. McQueen and J. E. Hockett, “Microstructures of aluminum compressed at various rates and temperatures,” *Metall. Trans.*, vol. 1, no. 11, pp. 2997–3004, 1970.
- [218] H. J. McQueen and J. J. Jonas, *Plastic deformation of materials*. New York: Academic Press, 1975.
- [219] K. Colligan, “Material Flow Behavior during Friction Stir Welding of Aluminum,” *Weld. J.*, vol. 78, no. July, pp. 229–237, 1999.
- [220] X. C. Liu, Y. F. Sun, T. Nagira, K. Ushioda, and H. Fujii, “Strain rate dependent micro-texture evolution in friction stir welding of copper,” *Materialia*, vol. 6, p. 100302, 2019.
- [221] X. C. Liu, Y. F. Sun, T. Nagira, K. Ushioda, and H. Fujii, “Evaluation of dynamic development of grain structure during friction stir welding of pure copper using a quasi in situ method,” *J. Mater. Sci. Technol.*, vol. 35, no. 7, pp. 1412–1421, 2019.
- [222] X. Liu, C. Wu, and G. K. Padhy, “Characterization of plastic deformation and material flow in ultrasonic vibration enhanced friction stir welding,” *Scr. Mater.*, vol. 102, pp. 95–98, 2015.
- [223] D. R. Cordray, L. R. Kaplan, P. M. Woyciesjes, and T. F. Kozak, “Solid-liquid phase diagram for ethylene glycol + water,” *Fluid Phase Equilib.*, vol. 117, pp. 146–152, 1996.
- [224] U. F. H. R. Suhuddin, S. Mironov, Y. S. Sato, H. Kokawa, and C. W. Lee, “Grain structure evolution during friction-stir welding of AZ31 magnesium alloy,” *Acta Mater.*, vol. 57, no. 18, pp. 5406–5418, 2009.
- [225] A. P. Reynolds, “Microstructure development in aluminum alloy friction stir welds,” in *Friction stir welding and processing*, R. S. Mishra and M. W. Mahoney, Eds. Materials Park, Ohio: ASM International, 2007, pp. 59–60.
- [226] F. Lambiase, A. Paoletti, and A. Di Ilio, “Forces and temperature variation during friction stir welding of aluminum alloy AA6082-T6,” *Int. J. Adv. Manuf. Technol.*, vol. 99, no. 1–4, pp. 337–346, 2018.
- [227] J. Yan, M. A. Sutton, and A. P. Reynolds, “Process – structure – property relationships for

- nugget and heat affected zone regions of AA2524 – T351 friction stir welds,” *Sci. Technol. Weld. Join.*, vol. 10, no. 6, pp. 725–736, 2005.
- [228] L. H. Shah, A. Fleury, L. St-George, S. Walbridge, and A. P. Gerlich, “Evolution of process parameters in friction stir welding of AA6061 aluminum alloy by varying tool eccentricity,” *Submitt. to Weld. World*, 2019.
- [229] U. F. Kocks, C. N. Tome, and H. R. Wenk, *Texture and anisotropy: preferred orientations in polycrystals and their effect on materials properties*. Cambridge, UK: Cambridge University Press, 1998.
- [230] M. Reza-E-Rabby, W. Tang, and A. P. Reynolds, “Effects of thread interruptions on tool pins in friction stir welding of AA6061,” *Sci. Technol. Weld. Join.*, vol. 23, no. 2, pp. 114–124, 2018.
- [231] M. Mehta, K. Chatterjee, and A. De, “Monitoring torque and traverse force in friction stir welding from input electrical signatures of driving motors,” *Sci. Technol. Weld. Join.*, vol. 18, no. 3, pp. 191–197, 2013.
- [232] R. Harish, R. Chandan, W. Prahalad, and H. A. Shivappa, “Design and Analysis of Machine Tool Spindle for Special Purpose Machines ( SPM ) and Standardizing the Design Using Autodesk Inventor ( I-Logic ),” *Int. J. Ignited Minds*, vol. 2, no. 9, pp. 193–202, 2015.
- [233] P. Upadhyay and A. P. Reynolds, “Effects of thermal boundary conditions in friction stir welded AA7050-T7 sheets,” *Mater. Sci. Eng. A*, vol. 527, pp. 1537–1543, 2010.
- [234] V. Firouzdor and S. Kou, “Al-to-Mg friction stir welding: Effect of material position, travel speed, and rotation speed,” *Metall. Mater. Trans. A Phys. Metall. Mater. Sci.*, vol. 41, no. 11, pp. 2914–2935, 2010.
- [235] A. Gerlich, M. Yamamoto, and T. H. North, “Local melting and tool slippage during friction stir spot welding of Al-alloys,” *J. Mater. Sci.*, vol. 43, pp. 2–11, 2008.
- [236] A. Gerlich, P. Su, M. Yamamoto, and T. H. North, “Effect of welding parameters on the strain rate and microstructure of friction stir spot welded 2024 aluminum alloy,” *J. Mater. Sci.*, vol. 42, no. 14, pp. 5589–5601, 2007.
- [237] A. Gerlich, G. Avramovic-Cingara, and T. H. North, “Stir zone microstructure and strain rate during Al 7075-T6 friction stir spot welding,” *Metall. Mater. Trans. A Phys. Metall. Mater. Sci.*, vol. 37, no. 9, pp. 2773–2786, 2006.
- [238] M. Yamamoto, A. Gerlich, T. H. North, and K. Shinozaki, “Cracking and local melting in Mg-alloy and Al-alloy during friction stir spot welding,” *Weld. World*, vol. 52, no. 9–10, pp. 38–46, 2008.
- [239] S. Kou, *Welding Metallurgy*, 2nd Editio. New Jersey, USA: John Wiley & Sons, 2003.
- [240] P. Venkateswaran and A. P. Reynolds, “Factors affecting the properties of friction stir welds between aluminum and magnesium alloys,” *Mater. Sci. Eng. A*, vol. 545, pp. 26–37, 2012.

- [241] T. Long, W. Tang, and A. P. Reynolds, "Process response parameter relationships in aluminium alloy friction stir welds," *Sci. Technol. Weld. Join.*, vol. 12, no. 4, pp. 311–317, 2007.

## Appendix A

### General properties of base metal AA6061-T6511 Al alloy

Chemical composition (in weight percentage, wt%)

Aluminum	Magnesium	Silicon	Manganese	Chromium	Copper	Zinc	Iron
Balance	0.81	0.53	0.08	0.06	0.18	0.01	0.19

Physical properties	Value
Melting range	582-652 °C
Density	2.713 g/cm <sup>3</sup>
Recrystallization temperature	69-154 °C
Thermal conductivity	167 W/mK
Electrical resistivity	0.04 Ωmm <sup>2</sup> /m
Young's modulus	68.9 GPa
Yield strength	276 MPa
Ultimate tensile strength	310 MPa
Poisson's ratio	0.33
Elongation	17%
Hardness	108 HV
Strengthening precipitates	$\beta''$ -Mg <sub>2</sub> Si (needle-shaped)

Sources:      1) Aluminum alloy database, J.F. Kaufman  
                   2) <http://asm.matweb.com>

## General properties of base metal AA5052-H32 Al alloy

Chemical composition (in weight percentage, wt%)

Aluminum	Magnesium	Silicon	Manganese	Chromium	Copper	Zinc	Iron
Balance	2.8	0.25	0.1	0.35	0.1	0.1	0.4

Physical properties	Value
Melting range	607-649 °C
Density	2.685 g/cm <sup>3</sup>
Recrystallization temperature	79-167 °C
Thermal conductivity	138 W/mK
Electrical resistivity	0.05 Ωmm <sup>2</sup> /m
Young's modulus	70.3 GPa
Yield strength	193 MPa
Ultimate tensile strength	228 MPa
Poisson's ratio	0.33
Elongation	18 %
Hardness	68 HV

Sources: 1) Aluminum alloy database, J.F. Kaufman  
2) <http://asm.matweb.com>

## Appendix B

The list below consists of academic contributions submitted by the author in the form of conference presentations and journal papers during the duration of the study. The individual contributions of each co-authors are also highlighted.

### Conference presentations

1. ‘Effect of tool runout in friction stir welding of aluminum alloy for structural applications’, **Luqman H.A. Shah**, S. Guo, S. Walbridge, A. Gerlich, *TMS 2017 146<sup>th</sup> Annual Meeting & Exhibition*, February 26 – March 2, 2017, San Diego, California, USA.

**Shah** presented the work and conducted the friction stir welding, mechanical and microstructural analysis. Guo assisted in the friction stir welding process, while Walbridge and Gerlich provided funding and valuable discussions on the subject.

2. ‘Effect of tool eccentricity on the microstructural and mechanical property of friction stir welded aluminum alloys’, **L.H. Shah**, S. Guo, S. Walbridge, A. Gerlich, *CanWeld Expo & Conference 2017*, September 13-17, 2017, Montreal, Quebec, Canada.

**Shah** presented the work and conducted the friction stir welding, mechanical and microstructural analysis. Guo assisted in the friction stir welding process, while Walbridge and Gerlich provided funding and valuable discussions on the subject.

3. ‘Effect of laser beam wobbling on AA6022 Al alloy to AZ31 Mg alloy dissimilar welding with Ni interlayer’, **Luqman Hakim Ahmad Shah**, Farzad Khodabakhshi, Adrian Gerlich, *International Conference on Aluminum Alloys 16*, June 17-21, 2018, Montreal, Quebec, Canada.



**Shah** presented the work and conducted the mechanical and microstructural characterizations. Khodabakhshi assisted in the microstructural characterization, while Gerlich provided the funding and provided valuable discussions on the subject.

4. ‘Evaluation of tool eccentricity on material flow and mechanical properties in friction stir welded AA6061 aluminum alloy’, **L.H. Shah**, S. Walbridge, A. Gerlich, *12<sup>th</sup> International Symposium on Friction Stir Welding*, June 26 – 28, 2018, Chicoutimi, Quebec, Canada.

**Shah** presented the work and conducted the friction stir welding, mechanical and microstructural analysis. Walbridge and Gerlich provided funding and valuable discussions on the subject.

5. ‘Effect of tool eccentricity & base metal positioning on dissimilar FSW of 5052-6061 aluminum alloys’, **Luqman Hakim Ahmad Shah**, Seyedhossein Sonbolestan, Scott Walbridge, Adrian Gerlich, *TMS 2019 148<sup>th</sup> Annual Meeting & Exhibition*, February 26 – March 2, 2017, San Antonio, Texas, USA.

**Shah** presented the work and conducted the friction stir welding as well as most of mechanical and microstructural characterizations. Sonbolestan conducted temperature measurements and hardness characterization. Walbridge and Gerlich provided funding and expertise on the subject.

## **Journal papers**

1. ‘Friction-stir processing of a cold sprayed AA7075 coating layer on the AZ31B substrate: Structural homogeneity, microstructures and hardness’ F Khodabakhshi, B Marzbanrad, **LH Shah**, H Jahed, AP Gerlich, *Surface and Coatings Technology* 2017, 331, 116-128.

Khodabakhshi wrote the article, microstructural and mechanical characterizations. Marzbanrad conducted the cold gas dynamic spraying process while **Shah** conducted the friction stir

processing. Jahed provided expertise on cold spray technology as well as funding and Gerlich provided expertise on friction stir processing technology and funding.

2. 'Review of research progress on aluminium-magnesium dissimilar friction stir welding', **L H Shah**, N H Othman, A Gerlich, *Science and Technology of Welding and Joining* 2018, 23(3) 256-270

**Shah** wrote the article, Othman compiled the literature review data and Gerlich provided valuable discussions on the subject.

3. 'Design guideline for intermetallic compound mitigation in Al-Mg dissimilar welding through addition of interlayer', **L H Shah**, A Gerlich, Y. Zhou, *International Journal of Advance Manufacturing Technology* 2018, 94, 2667-2678.

**Shah** wrote the article and conducted the experiments, Gerlich provided funding and expertise in microstructural analysis and Zhou provided funding and expertise in laser welding.

4. 'Effect of tool eccentricity on the properties of friction stir welded AA6061 aluminum alloys', **LH Shah**, S Guo, S Walbridge, A Gerlich, *Manufacturing Letters* 2018, 15, 14-17.

**Shah** wrote the article and conducted the friction stir welding, mechanical and microstructural analysis. Guo assisted in the friction stir welding process, while Walbridge and Gerlich provided funding and valuable discussions on the subject.

5. 'Effect of quality control parameter variations on the fatigue performance of aluminum friction stir welded joints', Shihui Guo, **Luqman Shah**, Rakesh Ranjan, Scott Walbridge, Adrian Gerlich, *International Journal of Fatigue* 2019, 118, 150-161.

Guo wrote most of the article and conducted the fatigue tests, **Shah** wrote a portion of the article, conducted the friction stir welding, hardness and microstructural characterizations. Ranjan conducted the fatigue tests and provided valuable discussions. Walbridge provided funding and conducted the fracture mechanics analysis, while Gerlich provided expertise on friction stir welding.

6. 'Effect of beam wobbling on laser welding of aluminum and magnesium alloy with nickel interlayer', **L.H. Shah**, F. Khodabakhshi, A. Gerlich, *Journal of Manufacturing Processes* 2019, 37, 212-219.

**Shah** wrote the article and conducted the mechanical and microstructural characterizations. Khodabakhshi assisted in the microstructural characterization, while Gerlich provided the funding and provided valuable discussions on the subject.

7. 'Dissimilar laser welding of an AA6022-AZ31 lap-joint by using Ni-interlayer: Novel beam-wobbling technique, processing parameters, and metallurgical characterization', F. Khodabakhshi, **L.H. Shah**, A.P. Gerlich, *Optics and Laser Technology* 2019, 112, 349-362.

Khodabakhshi wrote the article as well as mechanical and microstructural characterizations (XRD), **Shah** conducted the microstructural characterizations (SEM, EDX), while Gerlich provided expertise on the subject.

8. 'Tool eccentricity in friction stir welding: a comprehensive review', **L.H. Shah**, S. Walbridge and A. Gerlich, *Science and Technology of Welding and Joining* 2019, 24 (6), 566-578.

**Shah** wrote the article while Walbridge and Gerlich provided valuable discussions on the subject.

9. 'Surface modification of a cold gas dynamic spray-deposited titanium coating on aluminum alloy by using friction-stir processing', F. Khodabakhshi, B. Marzbanrad, **L.H. Shah**, H. Jahed, A.P. Gerlich, *Journal of Thermal Spray Technology* 2019, 28(6), 1185-1198.

Khodabakhshi wrote the article, microstructural and mechanical characterizations. Marzbanrad conducted the cold gas dynamic spraying process while **Shah** conducted the friction stir processing and microstructural analysis (SEM, EDX). Jahed provided expertise on cold spray technology as well as funding and Gerlich provided expertise on friction stir processing technology and funding.

10. 'Dissimilar friction stir welding of thick plate AA5052-AA6061 aluminum alloys: effects of material positioning and tool eccentricity', **Luqman Hakim Ahmad Shah**, Seyedhossein Sonbolestan, Abdelbaset R. H. Midawi, Scott Walbridge, Adrian Gerlich, *International Journal of Advance Manufacturing Processes* 2019, 105(1-4), 889-904.

**Shah** wrote the article, conducted the friction stir welding as well as most of mechanical and microstructural characterizations. Sonbolestan conducted temperature measurements and hardness characterization. Midawi conducted digital image correlation experiments and analysis. Walbridge and Gerlich provided funding and expertise on the subject.

11. 'The role of tool offset on the microstructure and mechanical properties of Al/Cu friction stir welded joints', Wentao Hou, **Luqman Hakim Ahmad Shah**, Guoqiang Huang, Zhikang Shen, Yifu Shen, Adrian Gerlich, *Journal of Alloys and Compounds* 2020, 825.

Hou wrote the article and conducted most of the friction stir welding temperature measurements with **Shah** and Huang. Z. Shen, Y. Shen and Gerlich provided funding and expertise on the subject.

12. 'Influence of tool eccentricity on the material flow and microstructural properties of AA6061 aluminum alloy friction stir welds', **L.H. Shah**, A.R.H. Midawi, S. Walbridge, A. Gerlich, *Journal of Alloys and Compounds* 2020, 826.

**Shah** wrote the article, conducted the friction stir welding process and most of the mechanical and microstructural characterizations. Midawi conducted digital image correlation experiments and analysis. Walbridge and Gerlich provided funding and expertise on the subject.

13. 'Influence of tool offsetting and base metal positioning on the material flow of AA5052-AA6061 dissimilar friction stir welding', **L.H. Shah**, A.R.H. Midawi, S. Walbridge, A. Gerlich, *Journal of Mechanical Engineering and Sciences* 2020, 14(1), 6393-6402.

**Shah** wrote the article, conducted the friction stir welding process and most of the mechanical and microstructural characterizations. Midawi conducted digital image correlation experiments and analysis. Walbridge and Gerlich provided funding and expertise on the subject.

14. 'Evolution of process parameters in friction stir welding of AA6061 aluminum alloy by varying tool eccentricity', **L.H. Shah**, A. Fleury, L. St-George, S. Walbridge, A.P. Gerlich, *International Journal of Advanced Manufacturing Technology* 2020, submitted.

**Shah** wrote the article, conducted the peak temperature and high speed camera (HSC) studies. Fleury conducted the force and torque measurements along with camera studies. St-George, Walbridge and Gerlich provided funding and expertise on the subject.

15. 'Structural morphology of AA6061 aluminum alloy friction stir welds through tool eccentricity', **L.H. Shah**, N. Huda, S. Esmaeili, S. Walbridge, A. P. Gerlich, *Materials Letters* 2020, submitted.

**Shah** wrote the article, conducted the macrostructural observations and sample preparations. Huda conducted the post-processing TEM analysis. Esmaeili provided critical information regarding TEM interpretation. Walbridge and Gerlich provided funding and expertise on the subject.